



HAL
open science

Detection and characterization of exoplanets using Doppler spectroscopy

Shweta Dalal

► **To cite this version:**

Shweta Dalal. Detection and characterization of exoplanets using Doppler spectroscopy. Astrophysics [astro-ph]. Sorbonne Université, 2020. English. NNT : 2020SORUS201 . tel-03404326

HAL Id: tel-03404326

<https://theses.hal.science/tel-03404326>

Submitted on 26 Oct 2021

HAL is a multi-disciplinary open access archive for the deposit and dissemination of scientific research documents, whether they are published or not. The documents may come from teaching and research institutions in France or abroad, or from public or private research centers.

L'archive ouverte pluridisciplinaire **HAL**, est destinée au dépôt et à la diffusion de documents scientifiques de niveau recherche, publiés ou non, émanant des établissements d'enseignement et de recherche français ou étrangers, des laboratoires publics ou privés.

École doctorale n° 127 :
Astronomie et Astrophysique d'Ile de France

Doctorat à l'Institut d'astrophysique de Paris

THÈSE

pour obtenir le grade de docteur délivré par

Sorbonne Université
Spécialité doctorale "Astrophysique"

présentée et soutenue publiquement par

Shweta DALAL

le 16 septembre 2020

**Detection & Characterization of Exoplanets
using Doppler Spectroscopy**

Directeur de thèse : **Guillaume HÉBRARD**
Co-directeur de thèse : **Alain LECAVELIER DES ÉTANGS**

Jury

M. Bruno Sicardy,	Président
M. Jean-Charles Augereau,	Rapporteur
M. Joshua Winn,	Rapporteur
Mme Claire Moutou,	Examineur
M. Claude Catala,	Examineur
M. Xavier Bonfils,	Examineur

Institu d'astrophysique de Paris
UMR CNRS 7095, PARIS, France

Publications

Nearly polar orbit of the sub-Neptune HD 3167 c. Constraints on the dynamical history of a multi-planet system

Dalal, S., Hébrard, G., Lecavelier des Étangs, A., Petit, A. C., Bourrier, V., Laskar, J., König, P.-C., & Correia, A. C. M. (2019), A&A, 631, A28.

Early science with SPIRou: near-infrared radial velocity and spectro-polarimetry of HD 189733

Moutou, C., Dalal, S., Donati, J.-F., Martioli, E., Folsom, C.P., Artigau, E., et al. (2020), arXiv e-prints, arXiv:2008.05411, A&A, **Accepted**

The SOPHIE search for northern extrasolar planets - Giant Long Period Exoplanets

Demangeon, O., Dalal, S., et al. (2020), **in prep.**

The SOPHIE search for northern extrasolar planets - giant planets, brown dwarfs and stellar companions

Dalal, S., Hébrard, G., et al. (2020), **in prep.**

Magnetism and spin-orbit alignment in the young planetary system AU Mic

Martioli, E., Hébrard, G., Moutou, C., Donati, J.-F., Artigau, E., Cale, B., Cook, N. J., Dalal, S., Delfosse, X., Forveille, T., et al. (2020), A&A, 641, L1.

SOPHIE related publications

Two Transiting Hot Jupiters from the WASP Survey: WASP-150b and WASP-176b

Cooke, B. F., Pollacco, D., Almléaky, Y., Barkaoui, K., Benkhaldoun, Z., Blake, J. A., Bouchy, F., Boumis, P., Brown, D. J. A., Bruni, I., et al. (2020), AJ, 159, 255.

Discovery and characterization of the exoplanets WASP-148b and c. A transiting system with two interacting giant planets

Hébrard, G., Diaz, R. F., Correia, A. C. M., Collier Cameron, A., Laskar, J., Pollacco, D., Almenara, J.-M., Anderson, D. R., Barros, S. C. C., Boisse, I., et al. (2020), arXiv e-prints, arXiv:2004.14645.

The SOPHIE search for northern extrasolar planets. XVI. HD 158259: A compact planetary system in a near-3:2 mean motion resonance chain

Hara, N. C., Bouchy, F., Stalport, M., Boisse, I., Rodrigues, J., Delisle, J.-B., Santerne, A., Henry, G. W., Arnold, L., Astudillo-Defru, N., et al. (2020), A&A, 636, L6.

XO-7 b: A Transiting Hot Jupiter with a Massive Companion on a Wide Orbit

Crouzet, N., Healy, B. F., Hébrard, G., McCullough, P. R., Long, D., Montañés-Rodríguez, P., Ribas, I., Vilardell, E., Herrero, E., Garcia-Melendo, E., Conjat, M., Foote, J., Garlitz, J., Vo, P., Santos, N. C., de Bruijne, J., Osborn, H. P., Dalal, S., & Nielsen, L. D. (2020), AJ, 159, 44.

Detection and characterisation of 54 massive companions with the SOPHIE spectrograph. Seven new brown dwarfs and constraints on the brown dwarf desert

Kiefer, F., Hébrard, G., Sahlmann, J., Sousa, S. G., Forveille, T., Santos, N., Mayor, M., Deleuil, M.,

Wilson, P. A., [Dalal, S.](#), et al. (2019), A&A, 631, A125.

The SOPHIE search for northern extrasolar planets. XV. A warm Neptune around the M dwarf Gl 378

Hobson, M. J., Delfosse, X., Astudillo-Defru, N., Boisse, I., Díaz, R. F., Bouchy, F., Bonfils, X., Forveille, T., Arnold, L., Borgniet, S., et al. (2019), A&A, 625, A18.

The SOPHIE search for northern extrasolar planets. XIV. A temperate ($T_{\text{eq}} 300 \text{ K}$) super-earth around the nearby star Gliese 411

Díaz, R. F., Delfosse, X., Hobson, M. J., Boisse, I., Astudillo-Defru, N., Bonfils, X., Henry, G. W., Arnold, L., Bouchy, F., Bourrier, V., et al. (2019), A&A, 625, A17.

The SOPHIE search for northern extrasolar planets. XIII. Two planets around M-dwarfs Gl617A and Gl96

Hobson, M. J., Díaz, R. F., Delfosse, X., Astudillo-Defru, N., Boisse, I., Bouchy, F., Bonfils, X., Forveille, T., Hara, N., Arnold, L., et al. (2018), A&A, 618, A103.

Talks & Posters

Exo Système I - Évolution, Paris (Jan 2020)

Oral presentation on the topic "Nearly Polar Orbit of sub Neptune HD3167 c".

Extreme Solar Systems IV, Iceland (Aug 2019)

Oral presentation on "Nearly Polar Orbit of sub Neptune HD3167 c".

3rd Advanced School on Exoplanetary Science, Vietri sul Mare, Italy (May 2019)

Presented a poster on "Nearly Polar Orbit of sub Neptune HD3167 c".

2nd Rencontres du Vietnam on Exoplanetary Science, Quy Nhon, Vietnam (Feb 2018)

Presented a poster on "Giant Planet Survey with SOPHIE".

Résumé

Plus de 4000 exoplanètes ont été découvertes dans une très grande diversité de systèmes planétaires. Les planètes découvertes présentent des caractéristiques très différentes de celles du Système solaire, avec, par exemple, de grandes obliquités, des Jupiters-chauds près de leurs étoiles ou des planètes sur des orbites très excentriques; cela implique un changement de perspective car les observations ne sont pas conformes aux théories classiques de la formation des planètes. L'étude de cette grande diversité de systèmes planétaires aide à répondre à de nombreuses questions fondamentales sur la formation et l'évolution des systèmes exoplanétaires, en particulier sur les processus de migration. Dans ce contexte, j'ai travaillé sur la découverte et la caractérisation de nouvelles planètes géantes. De plus, j'ai également étudié les exoplanètes en transit pour mesurer leurs obliquités. Les mesures de vitesses radiales ont été utilisées comme méthode de détection, en particulier avec le spectrographe SOPHIE de l'Observatoire Haute Provence (OHP). On trouvera ici la présentation de 6 nouvelles planètes géantes découvertes dans le cadre du consortium d'exoplanètes SOPHIE. Ces planètes ont une masse minimale allant de 0,7 à 4 masses de Jupiter. Toutes les planètes géantes détectées sont des «Jupiter froids» avec des périodes orbitales supérieures à 200 jours. En outre, 6 nouvelles naines brunes ont également été détectées avec une masse minimale de 20 à 90 masses de Jupiter dans le cadre d'un programme de recherche de naines brunes encore en cours avec SOPHIE. Ces détections permettent d'étudier la frontière entre les planètes massives et les étoiles de faible masse. Enfin, 15 nouveaux compagnons stellaires ont été détectés avec une masse comprise entre 0,096 et 0,382 masses solaires sur des orbites aussi proches que 30 jours et s'étendant jusqu'à plus de 10 ans.

L'obliquité contribue à la compréhension de l'histoire dynamique des systèmes exoplanétaires. Je présente la mesure de l'obliquité projetée sur le ciel pour HD3167 c. Je présente également l'obliquité projetée sur le ciel obtenue pour une exoplanète bien connue HD189733 à l'aide du nouveau spectropolarimètre SPIROU. Pour mesurer l'obliquité de la planète en transit HD3167 c, les données ont été obtenues avec le spectrographe HARPS-N. Plusieurs méthodes, à savoir la technique classique de Rossiter-McLaughlin, l'ombre Doppler et la technique dite de "reloaded Rossiter-McLaughlin", ont été mises en œuvre car il s'agit d'une mesure difficile avec une exoplanète de petite taille ayant un rayon de 3 rayons terrestres. La "sous-Neptune" HD3167c s'est révélée être sur une orbite presque polaire. Nous avons déduit via la dynamique de ce système multi-planétaire que les orbites des planètes c et d doivent être presque coplanaires, concluant ainsi que les deux planètes c et d sont sur des orbites presque polaires. Enfin, il a été émis l'hypothèse qu'il existe un compagnon invisible supplémentaire dans le système afin d'expliquer les orbites polaires des planètes c et d. L'obliquité projetée sur le ciel pour l'exoplanète HD 189733 b a été mesurée à l'aide des données SPIROU. Les deux méthodes, à savoir la technique classique de Rossiter-McLaughlin et l'ombre Doppler, ont été utilisées. Nous obtenons une obliquité projetée sur le ciel similaire à celle obtenue à partir des données optiques. C'est la première fois que l'ombre Doppler est utilisée pour mesurer l'obliquité projetée sur le ciel dans la gamme des longueurs d'onde du proche infrarouge.



Abstract

More than 4000 exoplanets have been discovered with a diverse range of planetary systems. Unlike in our solar system, several discoveries such as high obliquity, the existence of hot Jupiters, and highly eccentric orbits changed our perspective as they do not conform to the classical theories of planet formation. The study of this diverse range of planetary systems helps us in answering many fundamental questions about the formation, evolution, and migration processes of exoplanetary systems. In this context, I have worked on the discovery and characterization of new giant planets. In addition, I have also studied transiting exoplanets to measure their obliquities.

The radial velocity technique is used as the detection method, with the SOPHIE spectrograph at Observatoire de Haute-Provence (OHP) as the detection instrument. I present six new giant planets that have been discovered under the SOPHIE exoplanet consortium. These planets have a minimum mass ranging from 0.7 up to 4 Jupiter masses. All of the detected giant planets are “Cool Jupiters” with orbital periods longer than 200 days. Furthermore, six new brown dwarfs have also been detected with minimum mass 20 - 90 Jupiter masses under an ongoing brown dwarf program with SOPHIE that allows the frontier between massive planets and low-mass stars to be studied. Additionally, 15 new stellar companions have been detected with a mass in the range of 0.096 – 0.382 solar masses in orbits as close as 30 days, as well as longer than ten years.

Obliquity contributes to the understanding of the dynamical history of exoplanetary systems. I present the measurement of sky-projected obliquity for HD 3167 c. I also present the sky-projected obliquity obtained for a well-known exoplanet HD 189733 using a new spectropolarimeter SPIRou. To measure the sky-projected obliquity of a transiting planet HD3167 c, the data was obtained from the HARPS-N spectrograph. Several methods, i.e., Classical Rossiter-McLaughlin, Doppler Shadow and Reloaded Rossiter-McLaughlin, were implemented as it was a challenging measurement for a small-size exoplanet having a radius of 3.01 earth radii. The sub-Neptune HD3167 c was found to be in nearly polar orbit. The dynamical analysis of this multi-planetary system concluded that the orbits of planets c and d are nearly co-planar, which means that both planets c and d are in nearly polar orbits. Finally, it was speculated that there exists an additional unseen companion in the system that might be able to explain the polar orbits of planets c and d. The sky-projected obliquity for the exoplanet HD 189733 b was measured using SPIRou data. The two methods of Classical Rossiter-McLaughlin and Doppler Shadow techniques were used, with the resulting sky-projected obliquity found to be similar to the ones in literature from the optical data. This constitutes the first time that Doppler Shadow is used to measure sky-projected obliquity in the near-infrared wavelength range.

Acknowledgments

My research journey through exoplanets would not have been possible without the support of many kind people around me.

I wish to express my deepest gratitude to my supervisor, Guillaume Hébrard, and my co-supervisor, Alain Lecavelier des Étangs, for guiding me and for their continuous support during my Ph.D. I want to thank my great committee: Bruno Sicardy (President of the jury), Jean-Charles Augereau (reviewer), Joshua Winn (reviewer), Claire Moutou (examiner), Claude Catala (examiner), Xavier Bonfils (examiner) for their positive, insightful and encouraging comments. I am also grateful to Eder Martioli for having various interesting discussions and his continuous optimistic nature. I am extremely thankful for being part of the SOPHIE team, which allowed me to visit the beautiful landscapes in the Alpes.

The morning, afternoon, and evening coffee breaks with my colleagues/friends helped me in writing this thesis. I appreciate a lot Pierre's help with every little Ph.D. struggle, be it administrative or personal. I am grateful to rely on Simon's astronomy knowledge during my Ph.D. I am thankful to Amaël Ellien (or Email Alien) for making our office entertaining. It has been a pleasure to have a little coffee club with Pierre, Lukas, Alexandre, Quentin, François, Virginia and Aline. Thank you, Eduardo Vitral, for your sweet treats and encouraging words. I am especially thankful to you for providing me with the improved version of your python codes, which helped me to create beautiful plots. I am also thankful to my ex-labmates/friends Doogesh and Matteo for always being there and for their countless conversations, including bits of advice. I am grateful to my Ping Pong partner, Julien, and my excellent (no sarcasm here) Ph.D. day organizer partner, Lucas Pinol for being just incredible.

I am most grateful to my best friend Soumita, for providing me with emotional support at difficult times and also sharing my happy/sad/stress/nervous moments during this Ph.D. I want to express my special thanks to my friend and a fantastic researcher, Vaibhav Pant, who inspired me continuously and encouraged me throughout my Ph.D. I am a bit thankful to my two friends Anoop and Sachin, who didn't play any roles in my Ph.D., but they helped and encouraged me to become better.

Throughout the years in Paris, I've met many wonderful people. Quentin and Baptiste: my Crêpe, Rock-4 temps partners, Nishit: my amazing Indian food friend and Goodminton: my LGBTQ+ badminton club. Thanks again to all the aforementioned people who helped me proof-read and improve this thesis in so many ways.

Finally, I am really thankful to my parents and my three little sisters, Anki, Niki, and Shikha, for always believing in me. I am grateful to my two cute little brothers, Tejas and Tanish, for bringing joy in my life with their smiles.

Contents

Contents	xi
1 Introduction	1
1.1 History	2
1.2 Searching for Exoplanets	3
1.2.1 Transit	3
1.2.2 Radial Velocity	3
1.2.3 Direct imaging	4
1.2.4 Microlensing	4
1.3 Solar System and Extra-Solar Systems	4
1.3.1 Solar System	4
1.3.2 Extra Solar Systems	5
1.4 Exoplanets	6
1.4.1 Diversity in Exoplanets	6
1.4.2 Classification of Exoplanets	6
1.5 Thesis	8
1.5.1 Keynote	8
1.5.2 Outline	9
1.6 References	9
2 Detection instruments and techniques	13
2.1 Detection Instruments	14
2.1.1 SOPHIE	14
2.1.2 HARPS-N	14
2.1.3 SPIRou	15
2.2 Data and Data Reduction	15
2.3 Detection Method - Radial Velocity	16
2.3.1 Keplerian Orbit	17
2.3.2 Model	18
2.3.3 Keplerian Fitting	19
2.4 Rossiter–McLaughlin Effect and Obliquity Measurement	21
2.4.1 Rossiter–McLaughlin Effect	21
2.4.2 Obliquity	22
2.4.3 Classical Rossiter–McLaughlin	23
2.4.4 Doppler Shadow	25
2.4.5 Reloaded Rossiter–McLaughlin	27
2.5 Challenges in the Radial Velocity Method	28
2.5.1 Activity Indicators	29
2.6 References	29

3	A stellar catalog for giant planet detection	33
3.1	Catalog definition	34
3.1.1	Criterion 1 - Volumetric Constraint	35
3.1.2	Criterion 2- Selection of Main Sequence stars	35
3.1.3	Criterion 3 - Removing SB9 binaries	35
3.1.4	Criterion 4 - Removing CORAVEL binaries and fast rotators	36
3.1.5	Criterion 5 - Removing targets from KECK survey	36
3.1.6	Criterion 6 - Removing targets from ELODIE survey	37
3.1.7	Criterion 7 - Removing known planets	37
3.2	Comparison with old Catalog	37
3.3	Conclusion	38
3.4	References	38
4	New Detections	39
4.1	Motivation	40
4.1.1	Giant Planets	40
4.1.2	Brown Dwarfs	42
4.2	Observations, Data Reduction and Keplerian fit	44
4.3	New Detections	45
4.3.1	Giant planets without drifts	45
4.3.2	Giant planets with drifts	49
4.3.3	Brown Dwarfs	50
4.3.4	Stellar Companions	50
4.4	False Positive Indicator Analysis	53
4.5	Summary and Conclusion	54
4.6	References	56
5	Obliquity Measurements	59
5.1	Why measure star-planets alignment/misalignment?	60
5.2	Obliquity measurement of a sub-Neptune HD 3167 c	62
5.2.1	Stellar and planetary parameters	63
5.2.2	Spin-Orbit (mis)alignment measurement	64
5.2.3	Results and Conclusion	77
5.2.4	Additional Information - True Obliquity	77
5.3	Revisiting obliquity of HD 189733 with SPIRou	78
5.3.1	Stellar and planetary parameters	78
5.3.2	Keplerian Orbit of HD 189733 in near infrared	78
5.3.3	Observation and Analysis	80
5.3.4	Obliquity measurement using classical RM Fit	81
5.3.5	Obliquity measurement using Doppler Shadow	83
5.3.6	Results and Conclusion	84
5.4	Summary	85
5.5	References	85
6	Conclusion & Prospects	89
6.1	References	92
A	Annexes	I

Chapter 1

Introduction

*“ Imagination will often carry us
to worlds that never were, but
without it, we go nowhere. ”*

Carl Sagan

Contents

1.1 History	2
1.2 Searching for Exoplanets	3
1.2.1 Transit	3
1.2.2 Radial Velocity	3
1.2.3 Direct imaging	4
1.2.4 Microlensing	4
1.3 Solar System and Extra-Solar Systems	4
1.3.1 Solar System	4
1.3.2 Extra Solar Systems	5
1.4 Exoplanets	6
1.4.1 Diversity in Exoplanets	6
1.4.2 Classification of Exoplanets	6
1.5 Thesis	8
1.5.1 Keynote	8
1.5.2 Outline	9
1.6 References	9

1.1 History

For many centuries, planets orbiting other stars, known as exoplanets, only existed in our imagination and science fiction. From the dark swamps of Yoda’s planet Dagobah to the desert planet with two Suns of Luke Skywalker’s Tatooine in Star Wars, our imagination has fiddled with many such exotic exoplanets under the guise of fiction and fantasy.

The fascination with worlds beyond Earth dates back to more than 2000 years with Epicurus asserting that “There is an infinite number of worlds, some like this world, others unlike it”. In the sixteenth century, the Italian philosopher, Giordano Bruno, argued that “There are countless suns and countless Earths all rotating around their suns...”. However, it was not until the mid-nineteenth century that astronomers began looking for exoplanets. The first possible observational evidence of an extrasolar planetary system’s existence is the spectrum of van Maanen’s star, recorded on October 24, 1917, over a glass plate (Zuckerman, 2015). Almost a century later, in a scientific conference, Wolszczan and Frail reported two exoplanets orbiting around a pulsar, PSR B1257+12 (Wolszczan & Frail, 1992). This discovery surprised many astronomers because they expected to find planets orbiting around only main-sequence stars (Lissauer, 1993).

HD 114762 b was the first planetary candidate discovered around a solar-type star with a minimum mass of 11 Jupiter Mass (Latham et al., 1989). This object’s nature was unknown until 2019 when Kiefer (2019) presented the evidence that this substellar object belongs to the brown dwarf regime using Gaia astrometry data. The first known exoplanet, 51 Pegasi b orbiting a “solar-type star”, was discovered in 1995 using the ELODIE spectrograph at Observatoire de Haute-Provence (OHP, France) (Mayor & Queloz, 1995). This spectacular discovery led Mayor and Queloz to the shared Nobel Prize in Physics in 2019. 51 Peg b is a gas giant, about Jupiter’s mass, which orbits its star at an orbital distance much smaller than that of Mercury orbiting the Sun. Gas giant planets were not expected to be found so close to the star as they were expected to form beyond the snow line¹(Pollack et al., 1996). This discovery completely changed our perspective of planetary systems and altered the existing fundamental models of planet formation and evolution. Later, many large, closely orbiting “hot Jupiters”² were discovered because they are easier to detect. In December 1999, the first multi-planet system was detected around the star ν Andromedae (Butler et al., 1999). The first transiting exoplanet, HD209458 b was discovered independently by Charbonneau et al. (2000) and Henry et al. (2000).

The next milestone achieved in the field of exoplanet research was to analyze the composition of the exoplanet atmosphere in October 2001 (Charbonneau et al., 2002). The big winner in the gold rush of detecting planet was NASA’s planet-finding mission Kepler (with an extended mission named K2). This space telescope showed remarkable results by discovering thousands of exoplanets. The first space mission devoted to exoplanet transits, CoRoT, launched in 2006, found the first telluric exoplanet. Since then, exoplanets have been ubiquitously observed throughout the Galaxy. Until today, more than 4000 exoplanets, more than 3000 multi-planet systems, Earth-like planets, and planets in potentially habitable zone³ have been discovered.

¹The snow line is the distance from the protostar at which the temperature is low (about 150-170 K) enough to form ice grains.

²Hot Jupiters are gas giant exoplanets that are similar to Jupiter but that have short orbital periods < 10 days, which cause their atmospheres to have high temperatures (Wang et al., 2015).

³The potentially habitable zone or circumstellar habitable zone (or sometimes “Goldilocks zone”) is the region around a star where a rocky planet with sufficient atmospheric pressure can maintain liquid water on its surface.

1.2 Searching for Exoplanets

Most of the night sky stars resemble tiny point light sources, even with the most powerful ground or space-based telescopes. Exoplanets are even smaller and too faint compared to the stars, which make their detection highly elusive and challenging. Therefore, scientists have developed a series of indirect methods to detect them.

Figure 1.1 illustrates the contribution of different methods to the detection of exoplanets. The radial velocity method was the first successful technique responsible for discovering exoplanets, and it continues to achieve remarkable results. Currently, the most successful planet-hunting technique is the transit method that has helped detect thousands of new exoplanets, including earth-sized planets. Thanks to space-based telescopes like TESS, Kepler, Spitzer, and CoRoT along with many ground-based instruments such as HARPS, HIRES, SOPHIE, and SPIRou, astronomers are constantly overcoming pre-existing limitations to detect earth-size planets and study them in detail. The following four methods of detection have been the most successful in discovering new exoplanets.

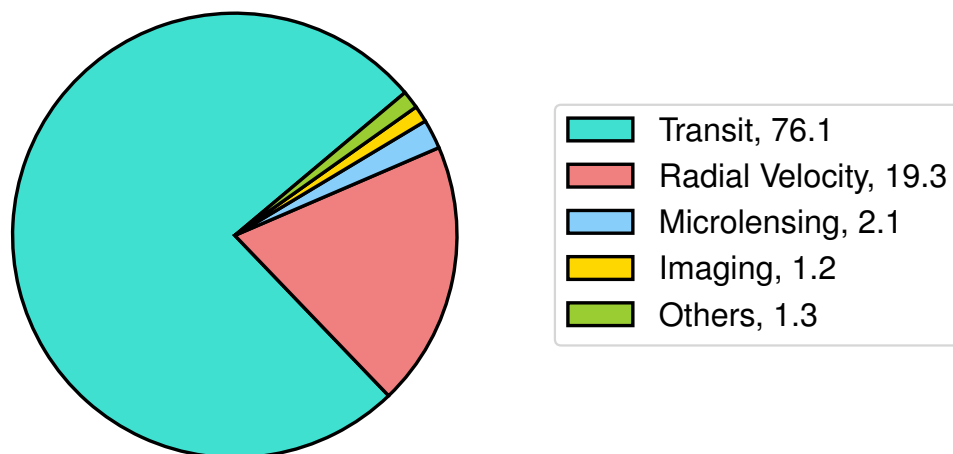


Figure 1.1 – Contribution of different methods of exoplanet detection. Source: NASA’s Exoplanet Archive (Table downloaded on April 27, 2020)

1.2.1 Transit

The transit method is an indirect method of detecting a planet by searching for little dips in starlight. When a planet passes in front of its star, it produces periodic “dips” in the stellar light. By taking photometric observations, these planetary transits can be detected, which indirectly implies the presence of exoplanets. This method is particularly advantageous as it reveals the planetary radius, provided the stellar radius is known. The transit observation also yields the orbital period and orbital inclination. The more detailed explanation of the transit method is provided in Section 2.4.1 of Chapter 2. Furthermore, using transmission spectroscopy, the light that grazes can be analyzed to study the planet’s atmosphere.

1.2.2 Radial Velocity

The radial velocity (hereafter RV) method is also an indirect method of detecting a planet by observing its host star’s wobble. For an Earth-like planet orbiting a solar-type star, the wobble is

at turtle-like speeds, and for a hot Jupiter, the wobble is similar to a high-speed train. A planet around a star perturbs its host star's orbit leading to a Doppler shift in the star spectrum, which can be detected using spectroscopy. Using this method, one can get the orbital period, eccentricity, and "minimum mass" of the planet. However, the true mass cannot be obtained only using the RV method except in multiple interacting systems. With the help of the transit method, the orbital inclination can be constrained for transiting systems, and the true planetary mass can be obtained. The detailed explanation of the RV method is given in Chapter 2.

1.2.3 Direct imaging

Direct Imaging is the only direct method known today for detecting exoplanets. The photograph of the planet(s) or the light from the planet(s) far from its parent star is obtained by blocking the glare of the host star. This light can either be light reflected from the host star or the planet's thermal emission. The direct imaging method is blooming as planets are also observed in X-ray and radio wavelengths to study star-planet interactions. This method has been successful in discovering young and self-luminous planets far from the host star. The direct imaging method allows us to measure the observed separation and period. By analyzing the reflected spectra from the planet's atmosphere, one can also obtain essential information about its composition and physical properties. Also, this method allows astronomers to place constraints on the planet's mass.

1.2.4 Microlensing

Microlensing is an indirect method of exoplanet detection whereby gravity is used as a magnifying glass. When a foreground star passes in front of a more distant background star, the foreground star's gravity acts like a lens, making the background star temporarily brighter. If that foreground star happens to host an exoplanet, that planet also acts as a gravitational lens and induces a tiny magnification in the background star's brightness, which can be detected. However, it is difficult to follow the planet detected for further characterization.

1.3 Solar System and Extra-Solar Systems

Until the discovery of exoplanetary systems, only the Solar System, our host planetary system, had provided us with a framework for understanding the fundamental physics involved in the formation and evolution of the planetary systems. However, exoplanets do not conform with the classical theories of planet formation, thereby completely changing our perspective about planetary systems. It is not yet clear if our Solar System is representative of planetary systems in the Universe, or it is one of the Extreme Solar Systems whose existence we are aware of, but it is the only system that we have studied in detail.

1.3.1 Solar System

The Solar System consists of a wide variety of objects such as the Sun, five dwarf planets, eight planets, hundreds of natural satellites, thousands of comets, and hundreds of thousands of minor bodies like asteroids and Kuiper belt objects.

The planets in the Solar System can be classified based on their composition as a) Terrestrial planets such as Mercury, Venus, Earth, and Mars, and b) Giant planets such as Jupiter, Saturn (Gas Giants), Uranus, and Neptune (Ice Giants). Terrestrial planets are mostly rocky and have relatively high densities, slow rotation, and solid surfaces. Giant planets are composed primarily

of hydrogen and helium and have lower densities, faster rotation, and denser atmospheres. We can also categorize these planets based on their mass for a simpler classification (Stern & Levison, 2002). Most of the Solar System planets are host to one or more natural satellites with their size ranging from a few km (Jupiter's Kale and Saturn's Anthe) to almost the size of a planet (the Moon, Jupiter's Io, and Saturn's Titan). All the outer planets of our Solar System are known to have rings around them. The planets in our Solar System are in nearly circular orbits with a mean eccentricity (e) of 0.04 around the Sun. Only Mercury has a slightly higher eccentricity of 0.206. Their orbits are almost aligned with the Sun's rotation axis (with a maximum inclination of 7° for the Mercury). Venus and Uranus have retrograde rotation, i.e., rotating in the direction opposite their orbital motion, while all other planets are in prograde rotation.

There are more than 3000 known comets in our Solar System. They consist mostly of ice and are coated with dark organic material that can hide important clues about the formation of our Solar System. Comets may have been the source of water, which is a crucial element for life on Earth.

These are some of the characteristics of the Solar System objects, which helped in understanding and building the foundations of the classical theory of planetary formation and evolution. The detailed review of how Solar System physics helped in exoplanet research can be found in Horner et al. (2020).

1.3.2 Extra Solar Systems

Since the dawn of exoplanet research, more than 3000 extrasolar systems have been discovered, some alike our Solar System, some very distinct. One of the planetary systems which resemble our Solar System the most is Kepler-90 with eight planets (Shallue & Vanderburg, 2018). There are a lot of multi-planetary systems like Kepler-90, but they are tightly packed, such as Kepler-80 (MacDonald et al., 2016) TRAPPIST-1 (Gillon et al., 2017) and HD 10180 (Lovis et al., 2011; Tuomi, 2012). Apart from detecting thousands of exoplanets, tens of exocomets in extrasolar Systems have been discovered. The first exocomet around Beta Pictoris was detected in 1987, much before the discovery of the exoplanet (Ferlet et al., 1987; Zieba et al., 2019). Some of the exocomets that have been observed around young stars are HR 2174 (Lecavelier Des Etangs et al., 1997), HD 172555 (Kiefer et al., 2014), and HD 225200 (Welsh & Montgomery, 2018).

There are other objects in extrasolar Systems known as brown dwarfs, which are intermediate between exoplanets and M-dwarfs with respect to mass. Brown dwarfs (BD) are sub-stellar objects ($13 < M < 80 M_J$) that are unable to sustain hydrogen burning in their inner core, but they can burn deuterium in its core, unlike planets. Recently, there has been some speculation with statistical evidence regarding the presence of rings around a transiting planet HIP 41378 f (Akinsanmi et al., 2020). But, high-precision transit observations are required to confirm/dismiss the presence of these planetary rings. Exomoons, i.e., moons around exoplanets, are not yet discovered, but there are some candidates such as Kepler 1625b I (Teachey & Kipping, 2018). To date, there is no detection of any other object from extrasolar systems.

The study of these peculiar and fascinating exoplanetary systems in detail will answer many of the fundamental questions surrounding the formation and evolution of the exoplanetary systems. This diversity in exoplanetary systems can also help in improving our understanding of our Solar System.

1.4 Exoplanets

Exoplanets are different from the Solar System planets in many ways, and some discoveries in extrasolar systems have left us baffled. One of the most surprising aspects of exoplanets is its broad diversity. Many “hot Jupiters” that are in close-in orbit with periods less than ten days have been detected, such as HD189733 b (Bouchy et al., 2005) and WASP-19b (Wong et al., 2020) unlike Jupiter of our Solar System, which orbits Sun in 12 years. As of April 27, 2020, more than 95.7% of the exoplanets detected are orbiting at a distance closer than that of Jupiter (Source: NASA’s Exoplanet Archive). This is one of the biases of observation techniques. Unlike Solar System planets, exoplanets have highly eccentric orbits such as HD 80606 b (Naef et al., 2001) with an eccentricity of 0.9. Some exoplanets have highly oblique orbits relative to the star rotation (e.g., such as HAT-P-30 b (Johnson et al., 2011) and WASP-121 b (Bourrier et al., 2020)), contrary to what has been observed in our Solar System. Some exoplanets are also found to be in retrograde orbits around its star, such as WASP-17 b (Anderson et al., 2010) and HAT-P-7 b (Narita et al., 2009). There are exoplanets that have periods less than one day, known as Ultra-Short Period (USP) planets, e.g., Kepler - 78 b (Sanchis-Ojeda et al., 2013) and HD 80653 b (Frustagli et al., 2020).

Exoplanets are found around all types of stars, from younger stars to older ones, from stars relatively cooler than Sun to hotter giant stars. In addition, there has been the detection of sodium, atomic hydrogen as well as water absorption features (e.g., HD 209458 b, Charbonneau et al., 2002; Deming et al., 2013; Vidal-Madjar et al., 2003) in the exoplanets’ atmospheres.

1.4.1 Diversity in Exoplanets

A table with all planetary parameters for confirmed exoplanets was downloaded on April 27, 2020, from NASA’s Exoplanet Archive to better visualize exoplanets’ diversity. This table is used in the thesis for all the plots which require data of confirmed exoplanets.

Figures 1.2 and 1.3 show the diversity of the exoplanets for different discovery methods. Figure 1.2 shows the distribution of detected exoplanets with their measured mass (m) or minimum mass ($m \sin I_p$) as a function of their orbital period. Figure 1.3 depicts the diversity of exoplanets with radius measurement as a function of their orbital period for different detection techniques. It is evident from these two figures that different exoplanet detection methods are sensitive to different subsets of the population of exoplanets. Every method has its own observational biases and limitations. For example, the transit method is sensitive towards detecting planets with shorter orbital periods. The radial velocity technique is more effective in finding planets that are massive and orbiting close to their host star perpendicular to the plane of the sky. The microlensing method is sensitive to the detection of exoplanets, which are around the snow line. Finally, the direct imaging method mostly explores the outer planets with long periods. Biases can influence our interpretation of the evidence (Sagan, 1996). Therefore, it is important to treat the different detection techniques’ inherent biases with the utmost care. Apart from that, a major factor that forms these distributions is related to the fact that different surveys have very different thresholds, which leads to the over-representation of certain types of exoplanets.

1.4.2 Classification of Exoplanets

To better understand the detected exoplanets, astronomers perform a classification based on their mass and radius. A more straightforward classification is used here, based on observed characteristics, i.e., mass (from radial velocity method) and radius (from transit method) to distinguish the different exoplanets population.

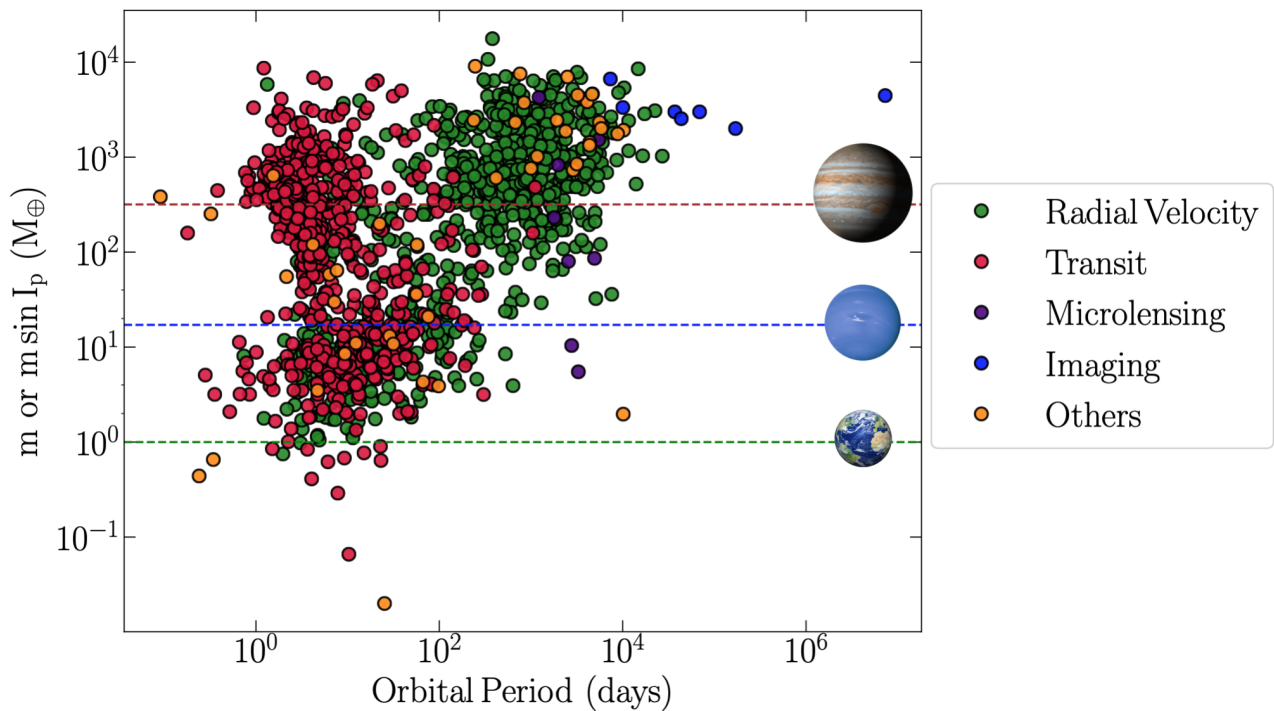


Figure 1.2 – Distribution of known exoplanets: Planetary mass (or minimum mass) as a function of orbital period for different discovery methods. Data is taken from NASA’s Exoplanet Archive.

- Planet Size⁴:

Based on [Borucki et al. \(2011\)](#) and [Fulton et al. \(2017\)](#), exoplanets are classified as follows:

- Earth-size ($<1.25 R_{\oplus}$)
- Super-Earths ($1.25 - 1.75 R_{\oplus}$)
- Sub-Neptunes ($1.75 - 3.5 R_{\oplus}$)
- Neptune-size ($3.5 - 6 R_{\oplus}$)
- Jupiter-size ($6 - 15 R_{\oplus}$)

- Planet Mass⁵:

Based on [Stevens & Gaudi \(2013\)](#), exoplanets are classified as follows:

- Earth planets ($0.1 - 2 M_{\oplus}$)
- Super-Earths ($2 - 10 M_{\oplus}$)
- Neptunes ($10 - 100 M_{\oplus}$)
- Jupiters ($100 - 10^3 M_{\oplus}$)
- Super-Jupiters ($10^3 M_{\oplus} - 13 M_J$)
- Brown Dwarfs ($13 M_J - 0.07 M_{\odot}$)
- Stellar Companions ($0.07 - 1 M_{\odot}$)

⁴ R_{\oplus} - Earth radius

⁵ M_{\oplus} - Earth mass, M_J - Jupiter mass, M_{\odot} - Sun mass

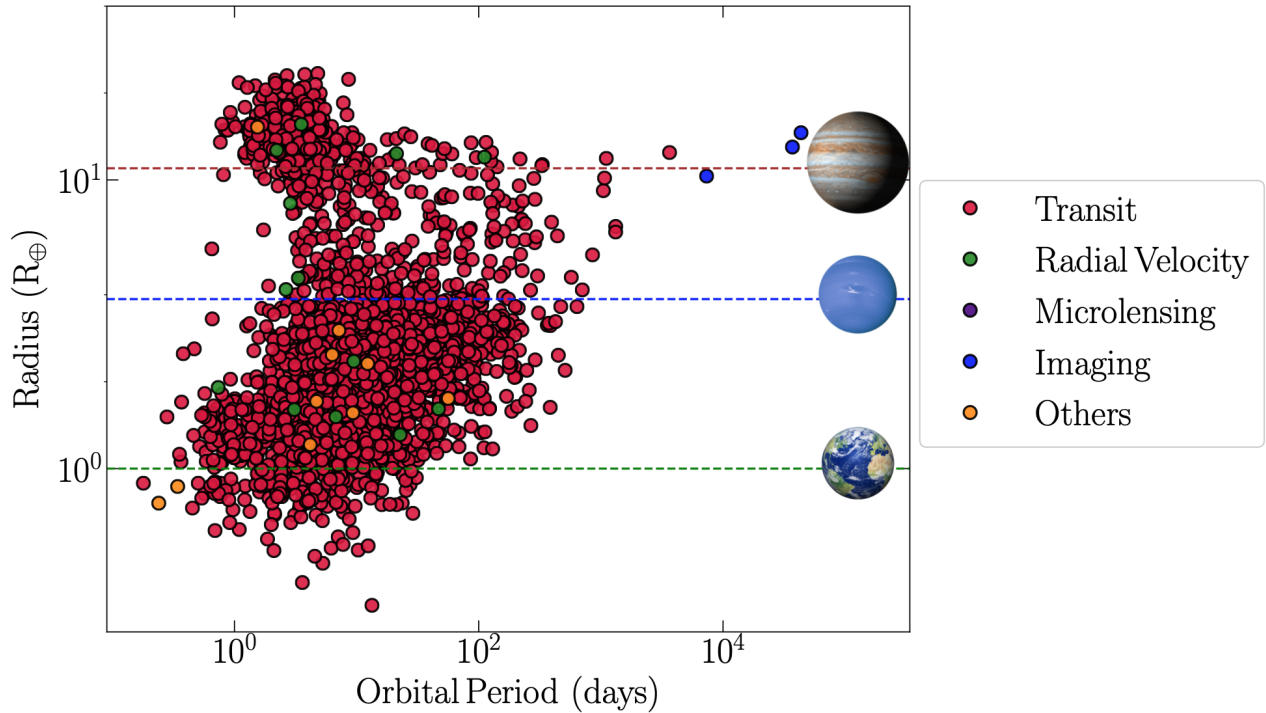


Figure 1.3 – Distribution of known exoplanets: Planetary radius as a function of the orbital period for different discovery methods. Data Credits: NASA’s Exoplanet Archive

Some of the well-known exoplanet types in the exoplanet community are included in the following paragraph.

Gas Giant Planets are similar to Solar System Gas Giants, which are primarily composed of ‘gas’ (hydrogen and helium) or ‘ices’ (volatiles such as water, methane, and ammonia). They have thick atmospheres of hydrogen and helium. **Sub Neptunes** are also called Mini-Neptunes, and they also have thick hydrogen-helium atmospheres, probably with deep layers of ice, rock, or liquid oceans. **Super Earths** are primarily rocky worlds that are larger than our Earth, yet smaller than Neptune or Uranus. **Terrestrial planets** are the exoplanets that are composed of mainly silicate rocks and metals. **Goldilock planets** are orbiting its host star within the star’s habitable zone.

1.5 Thesis

1.5.1 Keynote

Despite several decades of research, the fundamental questions about the formation and evolution of the exoplanetary systems remain unanswered. More detections with precise and accurate measurements of the different exoplanets’ parameters such as mass, radius, orbital distance, inclination, eccentricity, and obliquity are required to study them in detail. The statistical surveys of these planetary and stellar parameters reveal the hidden information about their origin. For instance, investigating the radius distribution of exoplanets may help to segregate different populations of exoplanets. [Fulton et al. \(2017\)](#) found that small-size exoplanets have two distinct populations, i.e. Super-Earths and Sub-Neptunes. Moreover, these authors reported a dearth of exoplanets at $1.8 R_{\oplus}$, known as the Fulton gap. They also postulated that the differences in the envelope masses of small planets can result in such a gap. One of the proposed mechanisms to

explain this observed radius distribution in small-size exoplanets is photoevaporation, wherein the small close-in planets may be stripped off their gaseous envelopes by x-ray and extreme ultraviolet (XUV) radiation from their host stars (e.g., [Lecavelier Des Etangs, 2007](#); [Lecavelier des Etangs et al., 2004](#); [Lopez et al., 2012](#); [Owen & Wu, 2013](#)). [Van Eylen et al. \(2018\)](#) found a similar gap that results in a dichotomy of small exoplanets into two populations. Thus, the observed radius distribution of exoplanets not only helps in distinguishing the exoplanets population but also helps in providing crucial information that will improve our understanding of low-mass planet formation. Furthermore, the mass-radius relationship, along with observation of the exoplanets' atmospheres, may help understand the composition of exoplanets' cores and envelopes. Likewise, the orbital distance distribution may shed some light on the planet evolution mechanisms. By analyzing the eccentricities of giant planets, [Dawson & Murray-Clay \(2013\)](#) found that the metal-rich stars host giant planets that have high eccentricities as compared to metal-poor stars. These high eccentricities can be explained by disk migration and planet-planet interactions. Another important probe for understanding the dynamical history of exoplanetary systems lies in the obliquity of the system. For example, the distribution of hot Jupiters' obliquities revealed that hot Jupiters around host stars with $T_{\text{eff}} > 6000\text{-}6300$ K are more oblique ([Albrecht et al., 2012](#); [Winn et al., 2010](#)).

It is important to detect and characterize new and diverse planetary systems to improve confidence in the observed trends in statistical distributions of the planetary system properties. These observed distributions of different orbital parameters are considered as fossil traces of the processes of planet formation or evolution, which ultimately help in constraining the planet formation mechanisms.

1.5.2 Outline

Having explained the importance of new detections, this thesis is mainly focused on discoveries and characterization of exoplanets.

In Chapter 2, I present the detection instruments and techniques that I used for the research done in this thesis. I describe the radial velocity measurements and analysis to search for exoplanets. I also discuss the method of distinguishing the true signal in the radial velocity from the stellar activity. I also explain three techniques i.e., Classical Rossiter-McLaughlin, Doppler Shadow, and Reloaded Rossiter-McLaughlin, which are used to measure the spin-orbit alignment of exoplanets. In Chapter 3, I discuss the new stellar catalog for giant planets detection for a volume-limited survey with SOPHIE. In chapter 4, I present the discovery of six new giant exoplanets, six new brown dwarfs, and 15 massive companions using the radial velocity method. SOPHIE spectrograph has been used for these new detections. In Chapter 5, I present the obliquity measurement of a sub-Neptune HD 3167 c using the three techniques mentioned above. I also present the obliquity measurement of the well-studied exoplanet HD 189733 b using a new spectropolarimeter, SPIRou. Finally, In Chapter 6, I summarise the main findings of this thesis and provide a future outlook.

1.6 References

Akinsanmi B., Santos N. C., Faria J. P., Oshagh M., Barros S. C. C., Santerne A., Charnoz S., 2020, [A&A, 635, L8 5](#)

Albrecht S., et al., 2012, [ApJ, 757, 18 9](#)

Anderson D. R., et al., 2010, [ApJ, 709, 159 6](#)

- Borucki W. J., et al., 2011, *ApJ*, 736, 19 7
- Bouchy F., et al., 2005, *A&A*, 444, L15 6
- Bourrier V., et al., 2020, *A&A*, 637, A36 6
- Butler R. P., Marcy G. W., Fischer D. A., Brown T. M., Contos A. R., Korzennik S. G., Nisenson P., Noyes R. W., 1999, *ApJ*, 526, 916 2
- Charbonneau D., Brown T. M., Latham D. W., Mayor M., 2000, *ApJ*, 529, L45 2
- Charbonneau D., Brown T. M., Noyes R. W., Gilliland R. L., 2002, *ApJ*, 568, 377 2, 6
- Dawson R. I., Murray-Clay R. A., 2013, *ApJ*, 767, L24 9
- Deming D., et al., 2013, *ApJ*, 774, 95 6
- Ferlet R., Hobbs L. M., Madjar A. V., 1987, *A&A*, 185, 267 5
- Frustagli G., et al., 2020, *A&A*, 633, A133 6
- Fulton B. J., et al., 2017, *AJ*, 154, 109 7, 8
- Gillon M., et al., 2017, *Nature*, 542, 456 5
- Henry G. W., Marcy G. W., Butler R. P., Vogt S. S., 2000, *ApJ*, 529, L41 2
- Horner J., et al., 2020, arXiv e-prints, p. arXiv:2004.13209 5
- Johnson J. A., et al., 2011, *ApJ*, 735, 24 6
- Kiefer F., 2019, *A&A*, 632, L9 2
- Kiefer F., Lecavelier des Etangs A., Augereau J. C., Vidal-Madjar A., Lagrange A. M., Beust H., 2014, *A&A*, 561, L10 5
- Latham D. W., Mazeh T., Stefanik R. P., Mayor M., Burki G., 1989, *Nature*, 339, 38 2
- Lecavelier Des Etangs A., 2007, *A&A*, 461, 1185 9
- Lecavelier Des Etangs A., et al., 1997, *A&A*, 325, 228 5
- Lecavelier des Etangs A., Vidal-Madjar A., McConnell J. C., Hébrard G., 2004, *A&A*, 418, L1 9
- Lissauer J. J., 1993, *ARA&A*, 31, 129 2
- Lopez E. D., Fortney J. J., Miller N., 2012, *ApJ*, 761, 59 9
- Lovis C., et al., 2011, *A&A*, 528, A112 5
- MacDonald M. G., et al., 2016, *AJ*, 152, 105 5
- Mayor M., Queloz D., 1995, *Nature*, 378, 355 2
- Naef D., et al., 2001, *A&A*, 375, L27 6
- Narita N., Sato B., Hirano T., Tamura M., 2009, *PASJ*, 61, L35 6

- Owen J. E., Wu Y., 2013, *ApJ*, 775, 105 9
- Pollack J. B., Hubickyj O., Bodenheimer P., Lissauer J. J., Podolak M., Greenzweig Y., 1996, , 124, 62 2
- Sagan C., 1996, The demon-haunted world. Science as a candle in the dark 6
- Sanchis-Ojeda R., Rappaport S., Winn J. N., Levine A., Kotson M. C., Latham D. W., Buchhave L. A., 2013, *ApJ*, 774, 54 6
- Shallue C. J., Vanderburg A., 2018, *AJ*, 155, 94 5
- Stern S. A., Levison H. F., 2002, Highlights of Astronomy, 12, 205 5
- Stevens D. J., Gaudi B. S., 2013, *PASP*, 125, 933 7
- Teachey A., Kipping D. M., 2018, *Science Advances*, 4, eaav1784 5
- Tuomi M., 2012, *A&A*, 543, A52 5
- Van Eylen V., Agentoft C., Lundkvist M. S., Kjeldsen H., Owen J. E., Fulton B. J., Petigura E., Snellen I., 2018, *MNRAS*, 479, 4786 9
- Vidal-Madjar A., Lecavelier des Etangs A., Désert J. M., Ballester G. E., Ferlet R., Hébrard G., Mayor M., 2003, *Nature*, 422, 143 6
- Wang J., Fischer D. A., Horch E. P., Huang X., 2015, *ApJ*, 799, 229 2
- Welsh B. Y., Montgomery S. L., 2018, *MNRAS*, 474, 1515 5
- Winn J. N., Fabrycky D., Albrecht S., Johnson J. A., 2010, *ApJ*, 718, L145 9
- Wolszczan A., Frail D. A., 1992, *Nature*, 355, 145 2
- Wong I., et al., 2020, *AJ*, 159, 104 6
- Zieba S., Zwintz K., Kenworthy M. A., Kennedy G. M., 2019, *A&A*, 625, L13 5
- Zuckerman B., 2015, in Dufour P., Bergeron P., Fontaine G., eds, Astronomical Society of the Pacific Conference Series Vol. 493, 19th European Workshop on White Dwarfs. p. 291 ([arXiv:1410.2575](https://arxiv.org/abs/1410.2575)) 2

Chapter 2

Detection instruments and techniques

“ If we assume we’ve arrived, we stop searching, we stop developing ”

Jocelyn Bell Burnell

Contents

2.1	Detection Instruments	14
2.1.1	SOPHIE	14
2.1.2	HARPS-N	14
2.1.3	SPIRou	15
2.2	Data and Data Reduction	15
2.3	Detection Method - Radial Velocity	16
2.3.1	Keplerian Orbit	17
2.3.2	Model	18
2.3.3	Keplerian Fitting	19
2.4	Rossiter–McLaughlin Effect and Obliquity Measurement	21
2.4.1	Rossiter–McLaughlin Effect	21
2.4.2	Obliquity	22
2.4.3	Classical Rossiter–McLaughlin	23
2.4.4	Doppler Shadow	25
2.4.5	Reloaded Rossiter–McLaughlin	27
2.5	Challenges in the Radial Velocity Method	28
2.5.1	Activity Indicators	29
2.6	References	29

A few of the known exoplanets (19.3%) have been discovered from the Doppler shift of the stellar spectrum or the radial velocity method (as of April 27, 2020). These high-precision radial velocity measurements can be determined using spectrographs. Modern spectrographs can detect the radial velocity variations below 1 ms^{-1} . Some of the well-known spectrographs used for exoplanet detection and characterization are APF, CARMENES, ESPRESSO, HARPS, HARPS-N, HIRES, or SOPHIE.

2.1 Detection Instruments

2.1.1 SOPHIE

SOPHIE (Spectrographe pour l'Observation des PHénomènes des Intérieurs stellaires et des Exoplanètes) is a high resolution échelle spectrograph at the 1.93 m telescope of Observatoire de Haute-Provence (OHP), France, that has been in operation since 2006 (Bouchy & Sophie Team, 2006; Perruchot et al., 2008). It is the successor of the ELODIE spectrograph which was in operation from 1994 to 2006 (Baranne et al., 1996). Perruchot et al. (2008) provides a detailed description of the instrument's optical design and technical key points for obtaining high accuracy radial velocity measurements. In 2011, SOPHIE was upgraded to SOPHIE+, by replacing the circular fibre with an octagonal-section fibre in the fibre link to improve the scrambling (Bouchy et al., 2013; Perruchot et al., 2011).

Specifications of the SOPHIE

SOPHIE is a fiber-fed cross-dispersed echelle spectrograph dedicated to high-precision radial velocity measurements. It is enclosed in an environmentally stabilized chamber to avoid drift in the spectrum due to temperature and pressure variations. The spectrograph has two spectral resolutions (R) corresponding to its two modes – the high resolution (HR) mode with $R = 75000$, and the high-efficiency (HE) mode with $R = 40000$. The light from the telescope is fed into the spectrograph through optical fibers. One of the two fibers is illuminated by the target while the other is illuminated either by the sky spectrum for estimating background moon pollution or the simultaneous calibration lamp exposure (see next paragraph) for tracking spectrograph drift. The spectrum is then projected onto an e2V 44-82 CCD (Charge Coupled Device) detector (4096x2048, 15-micron pixels), which yields 41 spectral orders, out of which 39 orders are recorded covering a wavelength range from 3872 \AA to 6943 \AA .

SOPHIE has a calibration unit with five slots for calibration lamps: two Thorium-Argon lamps, Tungsten, LDLS, and a Fabry-Perot etalon that are stored in a temperature-controlled room. The LDLS and the tungsten lamps are used for order localization and flat-field calibrations. The Thorium-Argon (Th-Ar) lamps are used for wavelength calibration. A Fabry-Perot etalon (FP) is used when observations with very accurate radial velocities are needed. The dense grid of lines and homogeneous amplitude of the FP spectrum have definite merit over the irregular distribution of the Th-Ar emission lines.

2.1.2 HARPS-N

HARPS-N (High Accuracy Radial velocity Planet Searcher - North) is an echelle spectrograph located at the 3.6 m Telescopio Nazionale Galileo (TNG), La Palma. It is designed to obtain high-precision radial velocity measurements. The designs of SOPHIE and HARPS-N are quite similar. HARPS-N is fiber-fed and has two fibers – one for calibration or sky exposures and another for stellar light. HARPS-N is enclosed in an environmentally stabilized vacuum chamber to avoid drifts

due to variations in temperature and pressure. The spectral wavelength range covered is 383 nm–690 nm. It has a higher spectral resolution as compared to SOPHIE with $R = 115000$. The spectrum is projected on an e2V CCD 231 detector, which allows 69 spectral orders. For wavelength calibration, HARPS-N has two calibration lamps similar to SOPHIE: Th-AR and Fabry-Perot (Cosentino et al., 2012).

HARPS-N has a better short-term radial velocity precision than SOPHIE with $\sim 0.3 \text{ ms}^{-1}$, thanks to the larger telescope and an environmentally stabilized vacuum chamber. Therefore, HARPS-N is a much more suitable instrument to obtain radial velocity data for detecting small exoplanet and for obliquity measurement of planets with small radii.

2.1.3 SPIRou

SPIRou (SPectropolarimètre InfraROUge) is a near-infrared spectropolarimeter and a high-precision velocimeter installed at the 3.6 m Canada-France-Hawaii Telescope (CFHT), Hawaii. It is enclosed in a vacuum cryogenic vessel cooled down to a temperature of 73 K, and stabilized at a sub-mK level (Reshetov et al., 2012). The spectrograph provides spectra in various bands, i.e., Y, J, H, and K (in the wavelength range 0.95–2.35 μm). It has a spectral resolution of $\sim 70,000$, and it is fed with three fluoride fibers – two science fibers collecting light out of the polarimeter and a calibration fiber. The spectrum is recorded with a 15-micron science grade H4RG detector. SPIRou has two modes: spectropolarimetric and spectroscopic. The radial velocities of the star can be obtained from both modes.

SPIRou is designed to be one of the most precise infrared velocimeters worldwide on the sky since 2019. It will unveil many new exoplanets around different stellar populations, mainly late M-dwarfs. The polarimeter on SPIRou is an additional tool for stellar characterization that allows the study of magnetic fields and stellar activity signals in the RV data. Along with the additional information offered by the polarimeter, SPIRou enables detailed characterization of the planetary system.

2.2 Data and Data Reduction

An automatic Data Reduction Software (DRS) is used to extract spectra from the CCD images. The process of spectra extraction includes localization of the orders on the images, optimal order extraction, cosmic-ray rejection, wavelength calibration, and one-dimensional flat-field correction. SOPHIE, HARPS-N, and SPIRou have their own DRS (Bouchy et al., 2009b; Cosentino et al., 2014, , Cook et al.; 2020, in prep.).

The resulting spectra are then cross-correlated with numerical masks (F0, G2, K0, K5, M4, and M5) corresponding to the spectral type of the star (see Figure 2.1). The obtained cross-correlation functions (CCF) is then fitted with Gaussians in order to derive the radial velocities (Baranne et al. (1996); Pepe et al. (2002)). The mean of the fitted Gaussian gives the radial velocity of the star. The thus obtained radial velocities (RVs) are then corrected for the charge transfer inefficiency (CTI) effect following Bouchy et al. (2009a). These RVs also include the barycentric correction corresponding to the observatory's motion relative to the Solar System barycenter. Other stellar parameters such as metallicity, the projected rotational velocity, and activity index can also be obtained directly from the pipeline.

These radial velocity measurements are then fitted with a Keplerian model derived from the physics behind the Doppler motion of the star, as described in Section 2.3. These models reveal the information about the exoplanet around that star. However, it should be taken into account

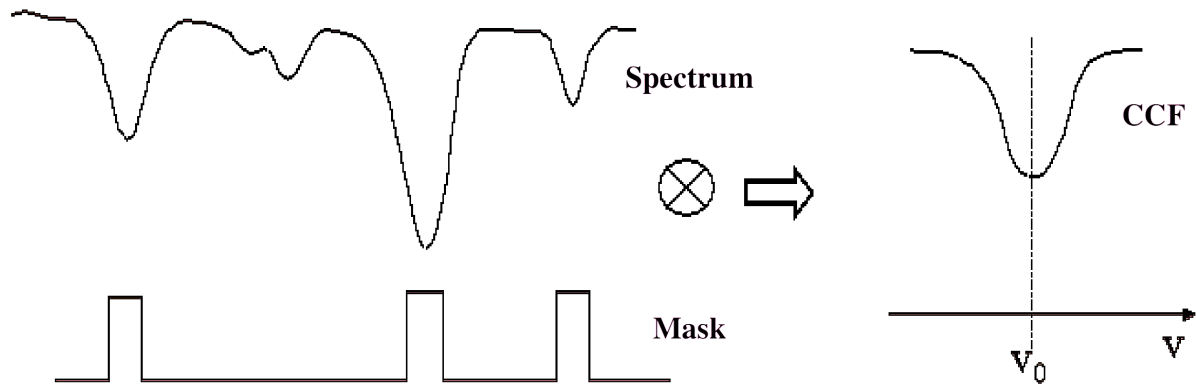


Figure 2.1 – Principle of cross-correlation with a numerical mask to obtain a CCF (Adapted from [Bouchy \(2006\)](#))

that this radial velocity signal of a few ms^{-1} can be mimicked by stellar activity ([Queloz et al., 2001](#)) and face-on binaries (e.g. [Díaz et al., 2012](#); [Wright et al., 2013](#)). To tackle such false positive scenarios, some indicators can be used to establish that the RV signal is, in fact, due to the Doppler of the star and not because of other stellar effects (see Section 2.5 for a more detailed explanation).

2.3 Detection Method - Radial Velocity

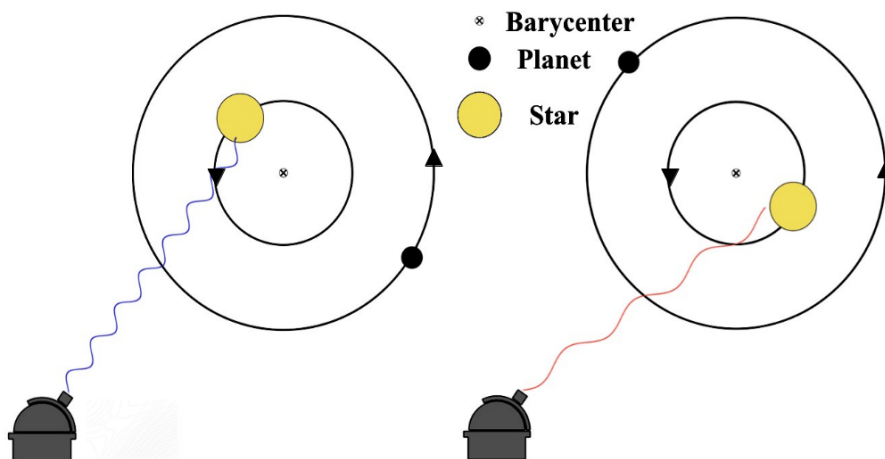


Figure 2.2 – Cartoon showing the radial velocity method: The stellar light is periodically blue-shifted and red-shifted when the star and planet orbit their barycenter.

The radial-velocity method, also known as Doppler spectroscopy, is an indirect method for finding exoplanets. It relies on the fact that in the presence of a planet (or planets), a star orbits the planet(s)-star common center of mass. When the star is traveling towards us, it will appear blue-shifted, and when it is traveling away, it will appear red-shifted, as illustrated in Figure 2.2. This shift in wavelength, which is caused by the periodic motion of a planet around its host star, can be measured with a spectrograph. The Doppler motion of the star reveals the hidden information about the orbital period and eccentricity of the planet and also helps us determine the lower limit on the planet's mass.

Besides the measurement of the apparent RV, one can also detect the Rossiter–McLaughlin (RM) Effect, which will be discussed in detail in Section 2.4.

2.3.1 Keplerian Orbit

The velocity of an isolated star is constant with respect to the barycenter of the Solar System. However, a star with a planet orbits around the common barycenter of the system. Figure 2.3 shows the top view of the planetary elliptical orbit. The orbit of the planet with respect to the star is given by Murray & Dermott (1999):

$$r_p = \frac{a(1 - e^2)}{1 + e \cos f} \quad (2.1)$$

where r_p is the star-planet distance, a is the semi-major axis, e is the eccentricity of the orbit and f is the true anomaly. The true anomaly can be expressed in terms of the eccentric anomaly E as,

$$\cos f = \frac{\cos E - e}{1 - e \cos E} \quad (2.2)$$

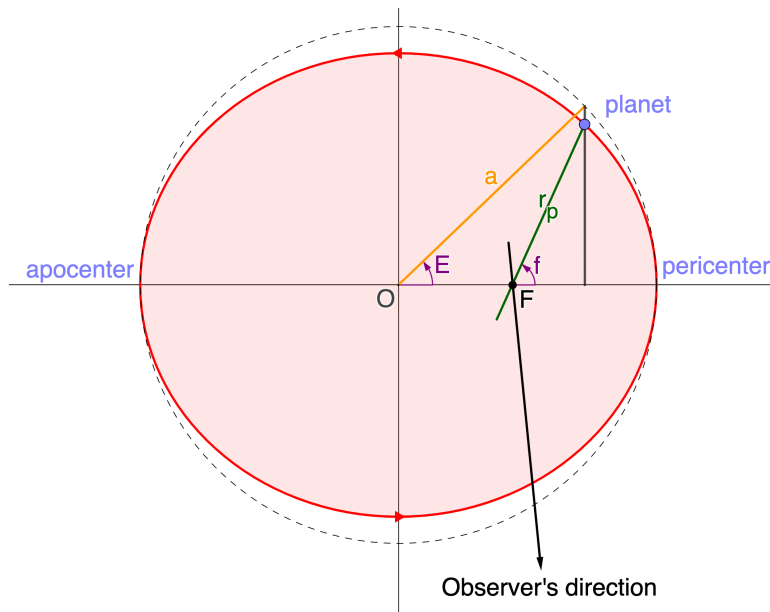


Figure 2.3 – Top view of the elliptical orbit of a planet. E and f describe the eccentric and the true anomaly respectively.

The eccentric anomaly is also related to the mean anomaly as

$$E - e \sin E = n(t - \tau) \quad (2.3)$$

where $n = 2\pi/P$ is the mean motion (P is the orbital period), and τ is the time of passage through the pericenter.

Figure 2.4 shows the three dimensional schematic of the same elliptical orbit. The three angles (I_p, Ω, ω) represent the projection of the true orbit into the observed orbit. I_p is the inclination between the orbital plane with respect to the sky. Ω specifies the longitude of the ascending node, and ω is the argument of the pericenter.

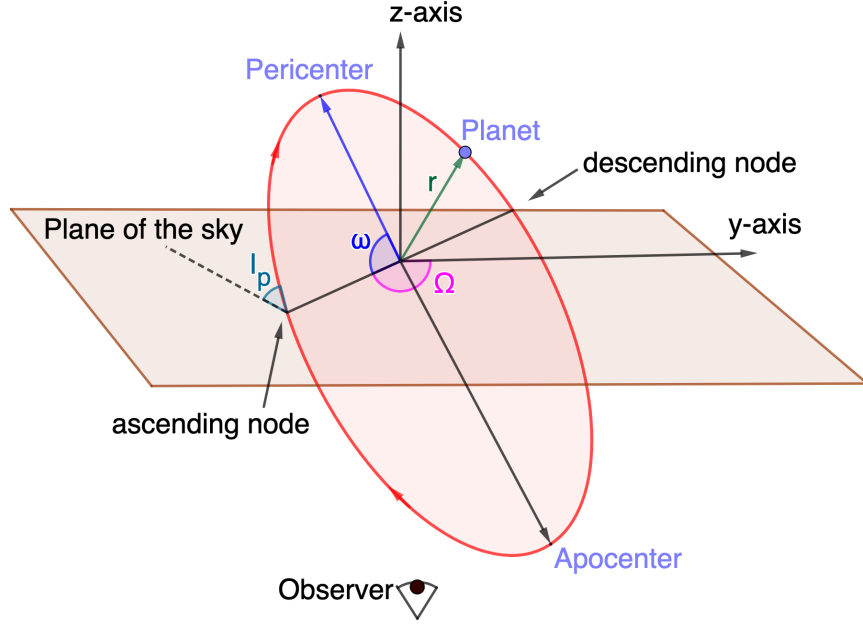


Figure 2.4 – Schematic configuration of a planetary orbit in three dimensions. (see Section 2.3.1 for the meaning of the symbols.)

2.3.2 Model

The radial velocity (V_r) of a star of mass (M) with a planet along the line of sight to the observer at a given time t is given by:

$$V_r(t) = K [\cos(f + \omega) + e \cos \omega] + v_{\text{ref}} \quad (2.4)$$

where

$$K = \frac{m \sin I_p}{(M + m)} \frac{2\pi a}{P \sqrt{1 - e^2}} \quad (2.5)$$

In the equations above K is the semi-amplitude, v_{ref} corresponds to the reference radial velocity of the barycenter and m is the mass of the planet. Using Kepler's third law to substitute a we can express the equation 2.5 as follows:

$$K = \frac{28.43 \text{ms}^{-1}}{\sqrt{1 - e^2}} \frac{m \sin I_p}{M_{\text{Jup}}} \left(\frac{m + M}{M_{\odot}} \right)^{-2/3} \left(\frac{P}{1 \text{yr}} \right)^{-1/3} \quad (2.6)$$

Using 2.6 the semi-amplitude can be determined for planets with different masses and semi-major axes. For Jupiter, the Sun wobbles with a semi-amplitude of 12.5 m/s and for Earth it wobbles with semi-amplitude of 9 cm/s. Table 2.1 shows the radial velocity semi-amplitude for different kinds of exoplanets that have been detected so far.

In binary stars, the radial velocity variations can be up to several kilometers per second. These systems are called spectroscopic binaries. In the case of a multi-planetary system, the radial velocity of the star will be given by simply adding the radial velocity due to each planet and neglecting any planet-planet interactions.

Planet Type	Name	K (m/s)	P (days)	a (A.U)	Reference
Gas Giant	HD9446 c	63.9	192.9	0.646	(Hébrard et al., 2010)
Hot Jupiter	51 Peg b	55.9	4.23	0.05	(Mayor & Queloz, 1995)
Sub Neptune	HD3167 c	2.24	29.84	0.1795	(Christiansen et al., 2017)
Super-Earth	HD85512 b	0.77	58.43	0.26	(Pepe et al., 2011)
Earth	Earth	0.09	365.25	1	⁻¹
Jupiter	Jupiter	12.5	4332.59	5.203	⁻²

Table 2.1 – Radial velocity semi-amplitude comparison for different kinds of planets and exoplanets.

¹ <https://nssdc.gsfc.nasa.gov/planetary/factsheet/earthfact.html>

² <https://nssdc.gsfc.nasa.gov/planetary/factsheet/jupiterfact.html>

2.3.3 Keplerian Fitting

The orbital parameters related to a star’s Keplerian orbit which can be determined from the radial velocity measurements are: P, K, e, ω , τ , and v_{sys} (see Table 2.2). v_{sys} is the combination of V_r and any instrumental drift in the spectrograph. These observables can be used to derive the ‘minimum mass’, $m \sin I_p$ of the planet:

$$\frac{m \sin I_p}{M_J} = 4.92 \times 10^{-3} (P)^{1/3} (1 - e^2)^{1/2} K \left(\frac{m + M}{M_\odot} \right)^{2/3} \quad (2.7)$$

Parameter	Symbol	Units
Orbital Period	P	days
Semi-amplitude	K	ms^{-1}
eccentricity	e	-
Argument of periastron	ω	deg
Periastron time	τ	BJD
Systemic velocity	v_{sys}	kms^{-1}

Table 2.2 – List of parameters that can be derived from radial velocity data using a Keplerian model

The first step in determining the Keplerian is to search for periodic signals in a periodogram analysis. The orbital period and the false alarm probability (FAP) can be estimated using the Lomb-Scargle periodogram. FAP determines the statistical significance of the signal. It is also important to identify other peaks in the periodogram that have very likely stellar, instrumental, or observational origin and not the planetary origin. For example, Dawson & Fabrycky (2010) found that an earlier reported 2.8 day period of 55 Cnc e by Fischer et al. (2008) was actually an alias, and the true period of 55 Cnc e was 0.74 days. The distinction of an alias from a physical frequency, therefore, is crucial for characterizing extrasolar planets.

Figure 2.5 shows the Lomb-Scargle periodogram of WASP-25 before and after fitting the Keplerian orbit. In the top panel of the periodogram, the spurious alias frequencies are likely caused by the discrete-time sampling of the observations, which disappear after removing the planetary signal. The preliminary estimate of the period from a periodogram (e.g., at 3.7 days for WASP-25) can be used to fit the data with equation 2.4 based on the parameter space using a χ^2 minimization. Markov Chain Monte Carlo (MCMC) techniques are also widely used for fitting radial velocities. Various tools available to fit radial velocity measurements includes radVel (Fulton et al., 2018), DACE¹ and yorbit (Ségransan et al., 2011).

¹<https://dace.unige.ch/radialVelocities>

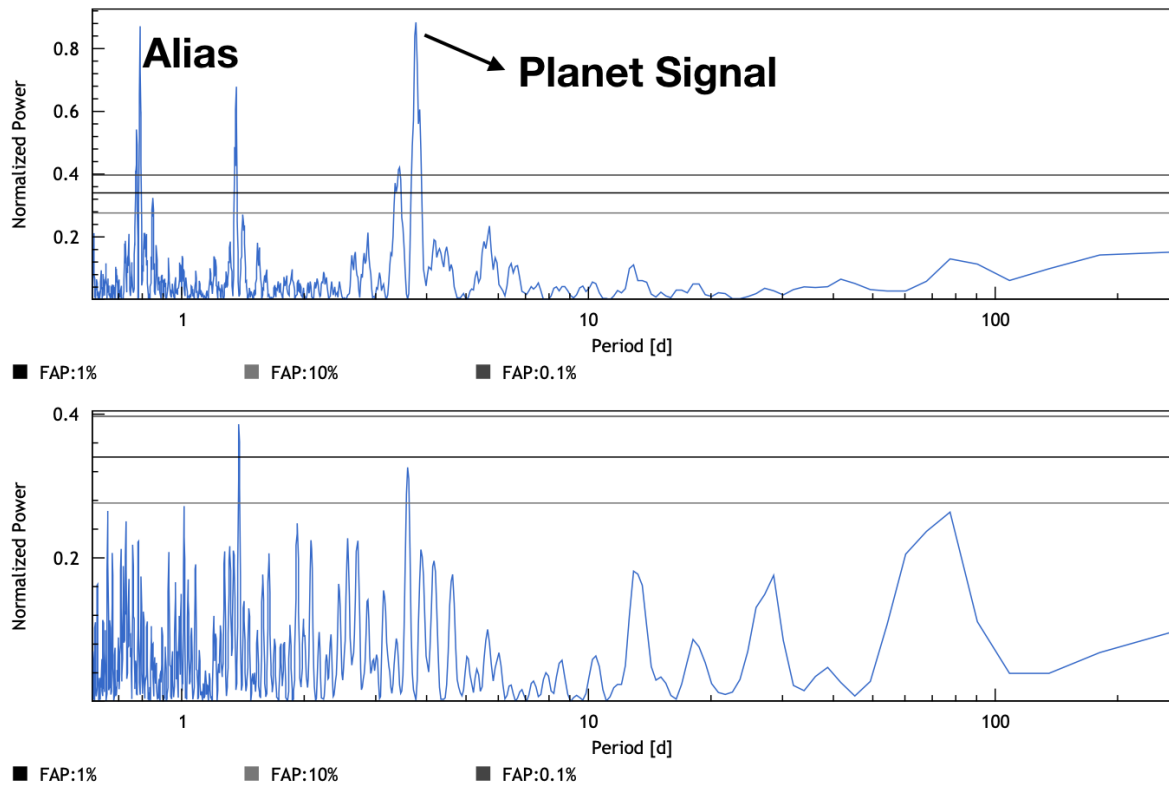


Figure 2.5 – Lomb-Scargle periodogram (using DACE) of WASP-25 with the data obtained from the CORALIE spectrograph. The top panel shows the periodogram of radial velocities of WASP-25, and the bottom panel shows the periodogram of residual radial velocities after fitting the one-planet Keplerian. The three solid lines indicate 10%, 1%, and 0.1% FAP.

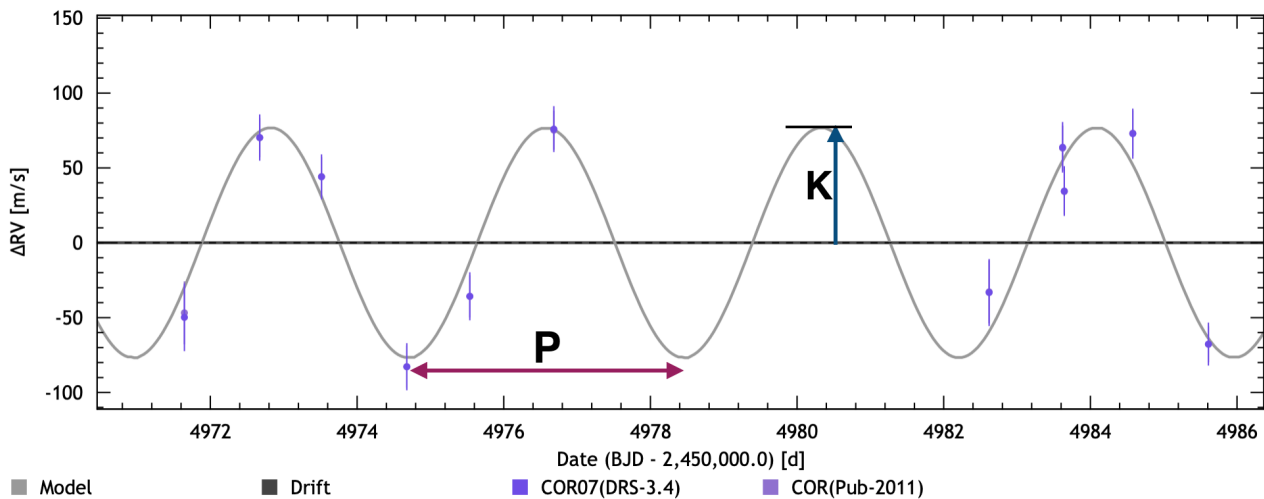


Figure 2.6 – Radial velocity curve of WASP-25 from DACE. The solid grey line shows the Keplerian orbit for the planet, and the blue circle are the radial velocity measurements taken between May 18, 2009, and June 5, 2009, using CORALIE spectrograph.

Figure 2.6 shows radial velocity curves along with some RV measurements for WASP-25 that hosts a hot Jupiter of mass $0.6 M_J$ and an orbital period of 3.76 days (Enoch et al., 2011). The orbit of WASP-25 b is circular. However, there have been many eccentric orbits detected for exoplanets. The eccentric orbits are tricky to deal. They might look to have long periods when observed near the apocenter, where the radial velocity shift is small. It has been argued that two planets in resonant circular orbits can mimic the radial velocity signal of a highly eccentric planet (Kürster et al., 2015). Proper observation strategies, therefore, need to be applied for characterizing a planet in an eccentric orbit.

2.4 Rossiter–McLaughlin Effect and Obliquity Measurement

2.4.1 Rossiter–McLaughlin Effect

The Rossiter–McLaughlin Effect is a spectroscopic phenomenon that is observed when an exoplanet or a star transits across the disk of the observed star. In addition to the photometric transit signal, there is a small spectroscopic signal along with the basic orbital Doppler shift. It was originally predicted as early as by Holt (1893). Later in 1924, Rossiter and McLaughlin simultaneously observed and described this effect, thus designating it as the 'Rossiter-McLaughlin effect.' Since the RM effect is a phenomenon related to the transit of the planet, I explain the basics of the transit method, which will be useful in modeling the RM effect.

Transit Basics

Periodic 'dips' in the stellar flux can be observed whenever a planet transits in front of the stellar disk, as shown in Figure 2.7.

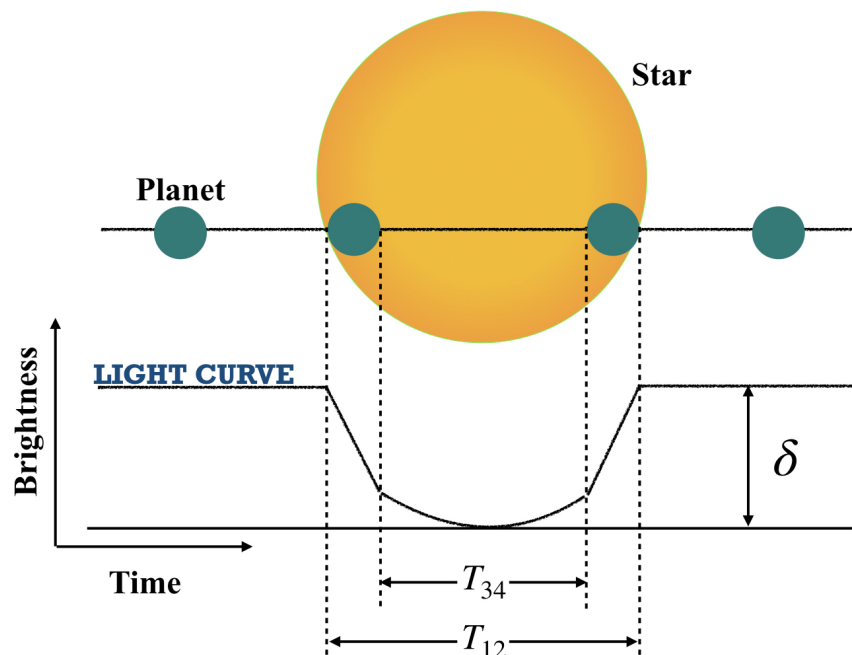


Figure 2.7 – Transit light curve: The bottom plot shows the schematic light curve in solid black line and the corresponding geometry of star and planet is shown on the top.

Seager & Mallén-Ornelas (2003) presented an analytical solution to derive planetary parameters from the transit of a planet. The orbital period (P) of the planet can be obtained by measuring

the time-span between two transits. Given the radius of the star (R), the radius of the planet (r) can be derived as follows:

$$r = R\sqrt{\delta} \quad (2.8)$$

where δ is the transit depth. The impact parameter b is also derived from the light curve as follows

$$b = \sqrt{\frac{(1 - \sqrt{\delta})^2 - [\sin^2(T_{23}\pi/P) / \sin^2(T_{14}\pi/P)](1 + \sqrt{\delta})^2}{1 - [\sin^2(T_{23}\pi/P) / \sin^2(T_{14}\pi/P)]}} \quad (2.9)$$

where T_{12} is the total duration of the transit and T_{34} is the duration of the transit when the planet disk is completely inside the stellar disk (see Figure 2.7). The semi-major axis a can be determined using Kepler's third law by considering m (mass of the planet) \ll M (mass of the star) as

$$a = \left(\frac{P^2 GM}{4\pi^2} \right)^{1/3} \quad (2.10)$$

where G is the gravitational constant. Using the above two equations, the planet's orbital inclination I_p can be derived as,

$$I_p = \cos^{-1} \left(\frac{bR}{a} \right) \quad (2.11)$$

These equations are derived for a planet in a circular orbit around its host star. Different transit models such as Mandel & Agol (2002), Giménez (2006) and many softwares such as TAP (Gazak et al., 2012) and batman (Kreidberg, 2015) are available for modeling and fitting the photometric transit. The shape of the limb darkening can influence the derived planetary parameters. The transit models take into account the stellar limb darkening while fitting the light curve. The laws proposed in the literature for limb darkening which are used in this thesis are:

The linear law:

$$\frac{I(\mu)}{I(\mu = 1)} = 1 - u(1 - \mu) \quad (2.12)$$

and the quadratic law:

$$\frac{I(\mu)}{I(\mu = 1)} = 1 - u_1(1 - \mu) - u_2(1 - \mu)^2 \quad (2.13)$$

where $\mu = \cos \theta$ (θ is the angle between the line of sight of the observer and the emerging flux) and $I(\mu = 1)$ is the central intensity. u denotes the linear limb darkening coefficient and u_1 and u_2 correspond to the quadratic limb darkening coefficients. Based on how well the observations constrain the shape of limb darkening, a non-linear law or a limb darkening law with more coefficients can be used to fit the transit curve.

2.4.2 Obliquity

Obliquity is the angle between the stellar rotation axis and the orbital axis of the exoplanet. It is different from axial tilt, which is the angle between an object's rotational axis and its orbital axis. One can measure the obliquity projected onto the sky through the Rossiter-McLaughlin (RM) effect. When a star rotates on its axis, one of its hemispheres appears to be coming towards the observer, making it slightly blue-shifted, and its other hemisphere appears to be moving away from the observer, making it red-shifted. When an exoplanet (or a star) transits the disk of the primary star, it covers both the hemispheres sequentially. For instance, if it blocks the blue-shifted hemisphere, the observer will receive a slightly red-shifted spectrum, giving rise to an apparent deviation in the radial velocity from the expected pattern (radial velocity due to the Doppler motion of the star). This deviation, often called 'anomaly,' arises due to the RM effect. Gaudi & Winn (2007) gives a detailed description of the RM effect.

True Obliquity

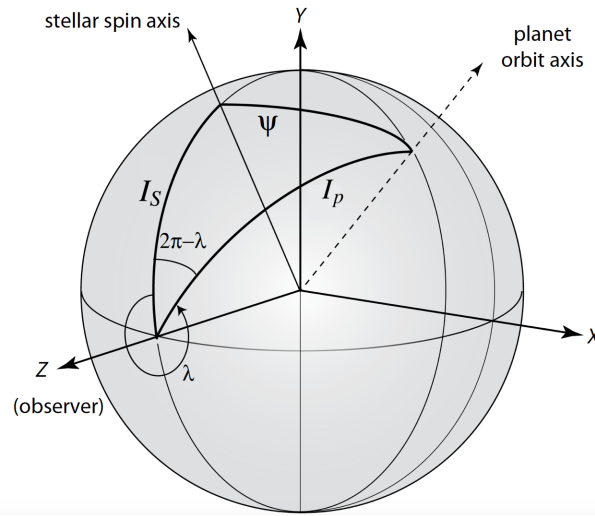


Figure 2.8 – Schematic Illustration to show different angles in a star-planet system. The true obliquity (ψ) is the angle between the stellar rotation axis and the planetary orbit axis. Adapted from [Perryman \(2018\)](#).

Most methods only access the measurement of obliquity projection on the plane of the sky which provides a lower limit to the true obliquity. Figure 2.8 shows an illustration of the system with true obliquity to describe the configuration of the system. The true spin–orbit misalignment ψ in three-dimensional space is defined as follows:

$$\cos \psi = \cos I_S \cos I_p + \sin I_S \sin I_p \cos \lambda, \quad (2.14)$$

It is difficult to determine the measurement of the true 3D obliquity as it is problematic to find the value of I_S . Various approaches have been used to determine it. One such method is to measure the line-of-sight rotational velocity of the star ($\Omega_S \sin I_S$) and to estimate the rotation period (P_{rot}) of the star separately in order to find the value of I_S as follows ([Winn et al., 2007](#), equation 8):

$$\sin I_S \equiv \Omega_S \sin I_S \left(\frac{P_{\text{rot}}}{2\pi R} \right) \quad (2.15)$$

where $\Omega_S \sin I_S$ can be determined from spectroscopic observations. P_{rot} and R (radius of the star) can be estimated from transit observations. I_S can also be determined using asteroseismology (e.g. [Ballot et al., 2006](#); [Gizon & Solanki, 2003](#)).

To measure the sky-projected obliquity (λ), various techniques are used in this thesis such as the classical Rossiter–McLaughlin technique (Section 2.4.3), which uses the radial velocity of the star, Doppler shadow (Section 2.4.4), and Reloaded Rossiter–McLaughlin technique (2.4.5) which use the information in the spectrum of the star, which is analyzed through the resulting CCF.

2.4.3 Classical Rossiter–McLaughlin

The classical Rossiter-McLaughlin technique considers that the asymmetry in the stellar line profile induces an anomaly in the measured radial velocity of the star, which can be analyzed to find λ . Figure 2.9 shows two examples of how the RM effect changes the shape of the RM anomaly ([Triaud, 2018](#)).

Model

The method developed by [Ohta et al. \(2005\)](#) is used to model the Rossiter–McLaughlin anomaly. They derive an approximate analytic formula for the anomaly by taking into account the stellar limb darkening.

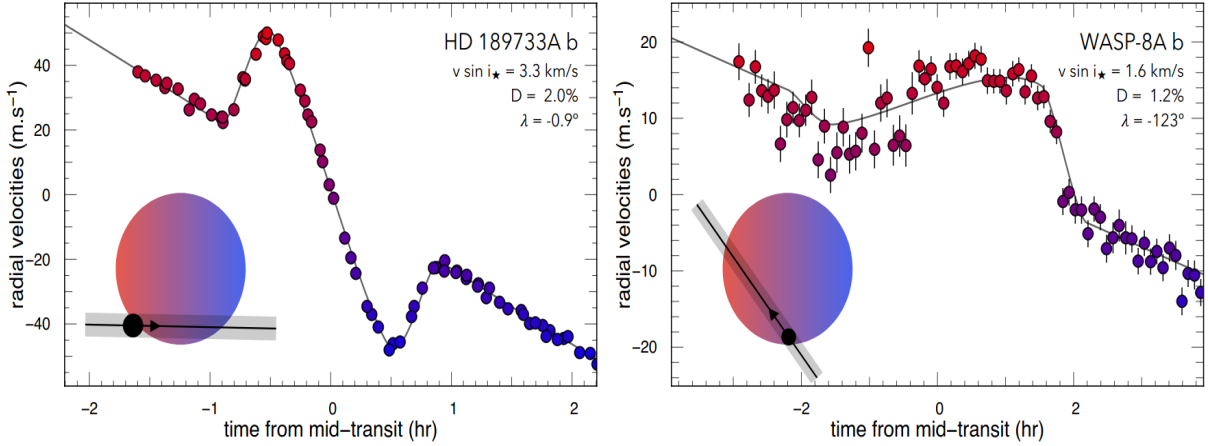


Figure 2.9 – *Left panel:* RM effect obtained for an aligned hot Jupiter HD 189733 A b. *Right panel:* RM effect for WASP-8 A b. In the bottom of each panel visual representation of the orbits are also provided. ([Triaud, 2018](#))

Consider a planet of mass m and radius r which is transiting in front of a star with mass M and radius R . The planet has a period P , eccentricity e , and argument of pericenter ω . The radial velocity variation of the star (ΔV) can be written as:

$$\Delta V(t) = \Delta V_K(t) + \Delta V_{RM}(t) \quad (2.16)$$

where $V_K(t)$ is the radial velocity variation due to the Doppler motion as expressed by Eq. 2.4 and $\Delta V_{RM}(t)$ is the radial velocity variation due to the RM effect. Eq. 20 of [Ohta et al. \(2005\)](#) gives the 'apparent' radial velocity anomaly due to the RM effect as:

$$\Delta V_{RM}(t) = -\Omega_S \sin I_S \frac{\iint x I(x, z) dx dz}{\iint I(x, z) dx dz} \quad (2.17)$$

where Ω_S is the angular velocity of the star and I_S is inclination of the stellar spin axis with respect to the sky plane. $I(x, z)$ is the surface intensity of the stellar disk. This radial velocity anomaly shape is linearly dependent on $\Omega_S \sin I_S$. The next step is to derive how the intensity of the star changes during ingress, transit and egress of the planet. The linear limb darkening law is adopted while computing the stellar surface intensity $I(x, z)$. To simplify, [Gaudi & Winn \(2007\)](#) write the radial velocity anomaly due to RM effect as:

$$\Delta V_{RM}(t) = K_{RM} g(t; x, u, \gamma, \dots) \quad (2.18)$$

where $\gamma \equiv r/R$, u is the linear limb darkening coefficient and K_{RM} is the amplitude of the RM effect which is given by:

$$K_{RM} = 52.8 \text{ ms}^{-1} \left(\frac{\Omega_S \sin I_S}{5 \text{ km s}^{-1}} \right) \left(\frac{r}{R_J} \right)^2 \left(\frac{R}{R_\odot} \right)^{-2} \quad (2.19)$$

In the above equation $\gamma \ll 1$ is assumed, R_J is the radius of Jupiter and R_\odot is the radius of the Sun. The function g depends on the position of the planet on the disk making it dependent on additional parameters such as impact parameter b and sky-projected obliquity λ . Figure 2.9 shows the shape of RM anomaly in the radial velocity data for a well-aligned and a misaligned system.

However, Ohta's model does not take into account any stellar effects, such as differential stellar rotation and center-to-limb convective variation. These effects can significantly influence the RM anomaly shape (Albrecht et al., 2012; Cegla et al., 2016b; Reiners et al., 2016). There have been improvements in the models of the classical RM technique that led to improved analytical estimates of the shape of the radial velocity anomaly (Boué et al., 2013; Fabrycky & Winn, 2009; Hirano et al., 2010, 2011). It is, therefore, important to consider stellar effects to obtain a better model of the RM anomaly.

The first reported planetary obliquity measurement using this classical RM technique was carried out by Queloz et al. (2000) for HD 209458 ($\lambda = 4^\circ \pm 20^\circ$). Since then, the classical RM technique has been used to measure obliquity for many systems such as HD 189733 (Winn et al., 2006), HD 80606 (Hébrard et al., 2010; Pont et al., 2009), and WASP-61 (Brown et al., 2017).

2.4.4 Doppler Shadow

When a planet transits its rotating host star, it blocks different regions of the stellar disk. When the planet blocks the blue-shifted hemisphere of the star, there is a positive bump on the blue-shifted wing of the absorption lines for the star (case A), and when the red-shifted hemisphere of the star is blocked, the positive bump is on the red-shifted wing (case B). Figure 2.10 shows two cases of the stellar line profile for KELT-21 b blocking the light of its host star (Johnson et al., 2018)². This positive bump is the planet's trace or the planet's 'Doppler shadow' on the stellar disk. The spectral position of the bump depends on the rotation of the star, the obliquity, and the impact parameter of the planet orbits, and its amplitude depends on the fraction of light blocked by the planet.

Model

Collier Cameron et al. (2010) (hereafter C10) developed a model to derive the obliquity based on Albrecht et al. (2007) by exploiting the full information in the stellar line profile. The approach followed by the C10 model is used for measuring λ in this thesis.

C10 model the observed stellar Cross-Correlation Function (CCF) as the convolution of a limb darkened rotation profile and a Gaussian corresponding to the average photospheric line profile.

$$h(x) = \int_{-1}^1 f(z) l(x-z) dz \quad (2.20)$$

where $f(z)$ is the limb darkened rotation profile and $l(x-z)$ is the local line profile at any point of a limb darkened rotating star. Since the CCF is observed in the barycentric frame, the above model is shifted to match the Keplerian orbit solution. The $f(x)$ and $l(x)$ are expressed as (C10)

$$f(x) = \frac{6 \left[(1-u)\sqrt{1-x^2} - \pi u(x^2-1)/4 \right]}{\pi(3-u)} \quad (2.21)$$

$$l(x) = \frac{1}{\sqrt{2\pi}s} \exp(-x^2/2s^2) \quad (2.22)$$

where x (dimensionless velocity) and s (non-rotating local CCF width) are expressed in units of the projected stellar equatorial rotation speed $\Omega_S \sin I_S$, i.e, $x = \Omega_S / (\Omega_S \sin I_S)$ and $s = \sigma / (\Omega_S \sin I_S)$. u is the linear limb darkening co-efficient.

To model the positive bump which travels across the stellar disk during the transit, C10 considered that the spectrum of the light coming from an elementary surface of the star is a Gaussian

²<http://www.astronomy.ohio-state.edu/~johnson.7240/#tomographygallery>

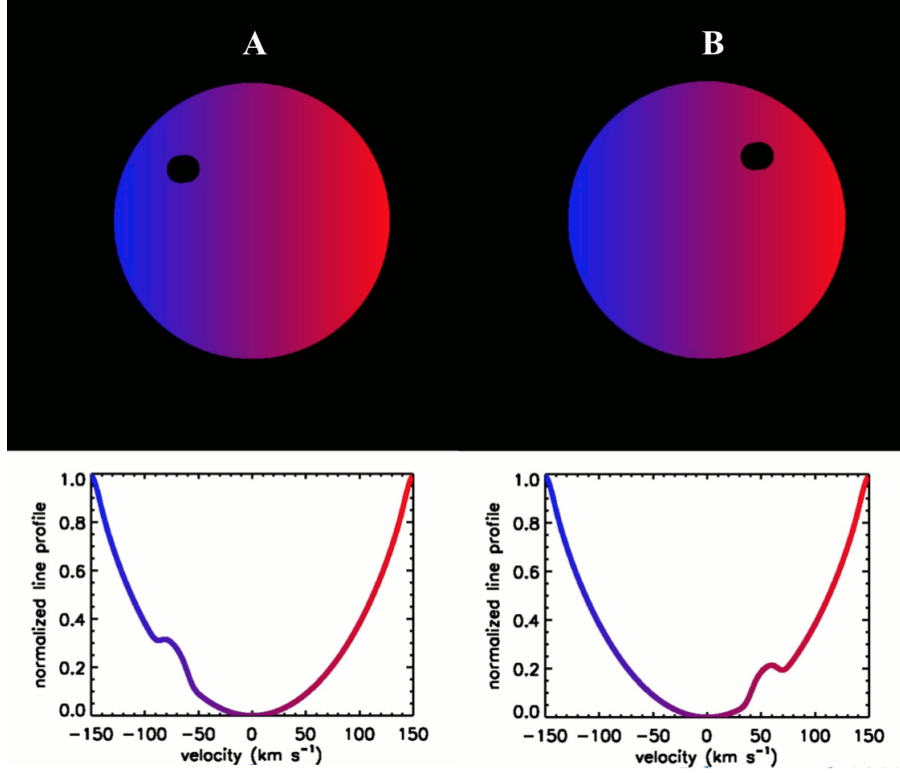


Figure 2.10 – Doppler Shadow: The two cases A and B show how the profile of the stellar absorption lines changes due to the planet transit. The bottom panel shows the CCF of the star along with the positive bump on the blue-shifted wing (case A) and red-shifted wing (case B) along with the corresponding position of the planet on the stellar disk shown on the top. (Johnson et al., 2018)

with an intrinsic width s . Therefore, the combined model of stellar CCF along with the missing light which is blocked by the planet is (C10)

$$p_{ij} = h(x_{ij}) + \beta l(x_{ij} - u_p) \quad (2.23)$$

where β is the fraction of light blocked by the planet at a moment during transit. u_p is the projected distance of the planet from the stellar rotation axis, which depends on λ (see the left-hand panel of Figure 2.11). x_{ij} is the shift of the model CCF to match orbit solution for a pixel i , and at the time of j th observation and p_{ij} is the model of stellar CCF that is subtracted from the observed CCFs to obtain the measurement of sky-projected obliquity.

DS is frequently used for faster rotating stars where the radial-velocity uncertainties increase. Since the Doppler shadow does not become 0 when the planet transits the center of the stellar axis, it helps to improve the significance of detection for systems with λ close to 90° (e.g., WASP-79 b, HD3167 c, Brown et al., 2017; Dalal et al., 2019). However, DS assumes a constant symmetric line profile across the stellar disk and ignores the effects of differential rotation and velocity shifts due to stellar effects. In Cegla et al. (2016b), the authors explore the impact of a convective blue-shift that varies across the stellar disk and non-Gaussian stellar photospheric profiles. They found that neglecting to account for the center-to-limb convective variation can significantly affect the RM waveform. For example, for a star with known $\Omega_S \sin I_S$, ignoring the convective center-to-limb variation can lead to an uncertainty in the λ of 10° – 20° (for $b=0$). Hence, neglecting the impact of stellar surface convection may bias the obliquity measurements, resulting in a biased interpretation of the theories on planetary formation and evolution.

The Doppler shadow technique has been adopted in measuring obliquity for many planetary

systems such as CoRoT-11 (Gandolfi et al., 2012), KOI-12b (Bourrier et al., 2015), HAT-P-41 (Johnson et al., 2017), XO-6 (Crouzet et al., 2017) and, WASP-180A (Temple et al., 2019).

2.4.5 Reloaded Rossiter–McLaughlin

The Reloaded Rossiter-McLaughlin (RRM) technique is similar to DS, where the light blocked behind the planet is isolated. However, RRM does not assume any particular shape for the intrinsic line profiles and allows us to directly analyze the local CCF occulted by the planet during transit. Apart from that, both differential rotation and center-to-limb net convective variations can also be taken into account while using the RRM technique.

Model

Cegla et al. (2016a) first presented the RRM technique and applied it to HD 189733. Like DS, the Doppler-reflex motion-induced due to the presence of the planetary companion(s) is removed. Unlike DS, a master is built CCF instead of having a model for the stellar line profile. The master CCF is created by adding all the CCFs taken outside of the transit. This master CCF is then used to align all the CCFs in the stellar rest-frame. The continuum fluxes for in-transit and out-transit CCFs are also scaled considering a quadratic limb darkening model. This allows the direct subtraction of all the CCFs from the master CCF. The top panel of Figure 2.11 shows the residual time series map of CCFs for WASP-8 b (Bourrier et al., 2017). The center of all the CCFs occurs at ~ 0 kms^{-1} as the orbital and systemic radial velocities are removed. The residual CCF during the transit shows the starlight behind the planet. A Gaussian profile is fitted to the residual CCFs to find the local RVs. The middle panel of Figure 2.11 shows the local RVs against the orbital phase. These local RVs are then fitted with a model to compute λ . These local RVs are modeled by taking into account the differential stellar rotation. The differential rotation law derived from the Sun (Reinhold et al., 2013, , Eq. 1) is assumed. In this case, the equatorial regions of the star rotate faster than its poles. Therefore, the stellar rotation velocity $v_{\text{rot}\star}$ is defined as

$$v_{\text{rot}\star} = u_p \Omega_S \sin I_S (1 - \alpha z') \quad (2.24)$$

where u_p is the projected distance of the planet from the stellar rotation axis (See Figure 2.11), and α is the differential rotation rate. For rigid body rotation, α is considered 0, like in the DS technique. z' is the distance of the planet from the stellar equator, which depends on the planet's position on the stellar disk. As mentioned above, the shift in the velocity due to center-to-limb convective variations are also considered. The net convective velocity shifts (v_{conv}) are defined as

$$v_{\text{conv}} = \sum_{i=0}^{i=n} c_i < \mu >^i \quad (2.25)$$

where n is the degree of the polynomial. To calculate v_{conv} , only in-transit residual CCFs are used. Therefore, the total velocity will be given by

$$v_{\text{RRM}} = v_{\text{conv}} + \frac{\sum I v_{\text{rot}\star}}{\sum I} \quad (2.26)$$

The local RVs are fitted using Eq. 2.26 to obtain λ , as shown in the right-hand panel of Figure 2.11.

This new technique has been implemented for the re-analysis of the WASP-8 system for which Bourrier et al. (2017) found $\lambda = -143.0^{+1.6}_{-1.5}$ degrees which is significantly different from the $\lambda = -123.0^{+3.4}_{-4.4}$ degrees obtained with the Classical RM technique in Queloz et al. (2010). Other systems, which used this technique to measure spin-orbit alignments, include GJ 436 (Bourrier et al., 2018) and HD 3167 (Dalal et al., 2019).

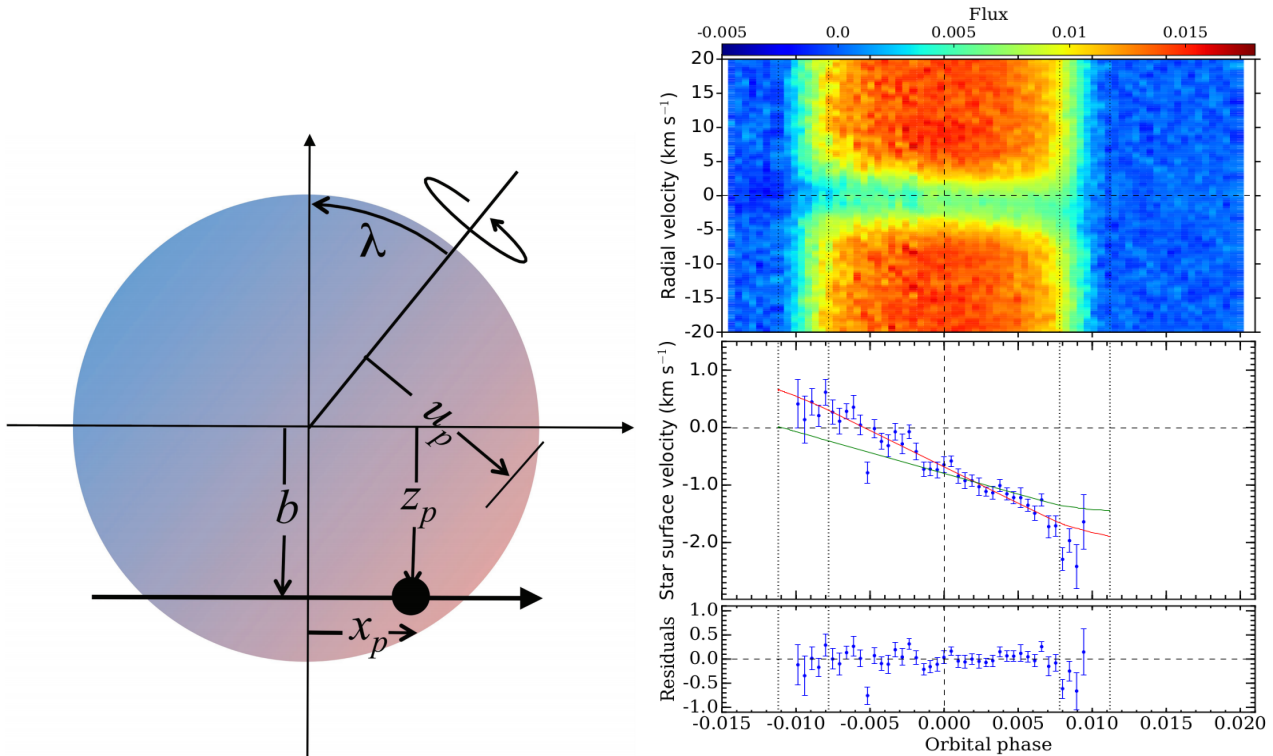


Figure 2.11 – *Left panel:* The instantaneous orbital coordinates of the planet on the stellar disk, x_p and z_p , are projected onto the plane of the sky (Collier Cameron et al., 2010). *Right panel:* The upper panel shows the map of residual time series maps of CCFs for WASP-8. The middle panel shows the local RVs fitted with a best-fit model obtained using the Reloaded RM method (Bourrier et al., 2017) with a red line and using the classical RM technique (Queloz et al., 2010) with a green line. The lower panel shows the residuals after subtracting the best-fit model.

2.5 Challenges in the Radial Velocity Method

The radial velocity method is a powerful method for detecting exoplanets, but it has its limitations. It gives no information about the size of the planet. A large low-density planet and a small high-density planet having the same mass will produce the same radial velocity signal. Another limitation is due to the system's geometry, i.e., the orbital inclination of the planet is unknown. The $m \sin I_p$ can, therefore, either correspond to a low-mass planet with high inclination or a high-mass planet or a brown dwarf with low inclination. It is, therefore, important to constrain the orbital inclination to confirm the nature of the planet.

There are other limitations of the RV method that arise due to the atmosphere of the star or due to the presence of a binary companion. The radial velocity of the star is determined by measuring the centroid of the spectral-line profile. The shape of the stellar line profile can be altered due to activity in the stellar atmosphere, which can give rise to variations in radial velocity that can either mask or mimic the planetary signal. It is, therefore, important to secure the planetary nature of the detected signal. It was first reported by Queloz et al. (2001) where they found that the RV variation for HD 166435 was due to starspots on the surface and not due to the gravitational interaction between the star and an orbiting planet. There have been many examples of such effects in the literature, such as HD 219542 (Desidera et al., 2003) and BD +201790 (Figueira et al., 2010).

To circumvent these challenges, various indicators are frequently used to detect signals that are induced by stellar activity or stellar systems. Some of the indicators are discussed below.

2.5.1 Activity Indicators

Bisector Inverse Slope

Star spots can distort the spectral lines, which can cause RV variations. A line bisector can be used to measure the shapes of the spectral line. The bisector is defined as the midpoint of the horizontal line segments bounded by the sides of the line profile (Toner & Gray, 1988). To compute the Bisector Inverse Slope (BIS), the difference between the velocity span of the top and bottom part of the bisector is calculated. BIS_{top} is the average of the bisector between 60% and 90% of the total contrast of the line profile and BIS_{bottom} is the average of the bisector between 10% and 40% of the total contrast of the line profile. Queloz et al. (2001) used this technique with different limits for BIS_{top} with 55% and 85% instead of 60% and 90%.

Boisse et al. (2011) suggested a similar but improved diagnosis for the bisector. This method is less sensitive to noise in the stellar line. To find the V_{span} , the difference between the mean of the two Gaussians (ϕ) fitted in the top and bottom of the CCF is calculated. The two Gaussians ($\phi_{top}, \phi_{bottom}$) are defined as follows:

$$\phi_{top} = \phi(-\infty, x_0 - 1\sigma) \cup \phi(x_0 + 1\sigma, \infty) \quad (2.27)$$

$$\phi_{bottom} = \phi(-\infty, x_0 - 3\sigma) \cup \phi(x_0 - 1\sigma, x_0 + 1\sigma) \cup \phi(x_0 + 3\sigma, \infty) \quad (2.28)$$

where x_0 is the measured radial velocity by fitting a Gaussian and σ is its standard deviation. The V_{span} is therefore defined as:

$$V_{span} = x_{top} - x_{bottom} \quad (2.29)$$

where x_{top} and x_{bottom} are the means of the Gaussians ϕ_{top} , and ϕ_{bottom} respectively.

R'_{HK}

The Ca II H and K lines are widely used as indicators of stellar magnetic activity which can be parametrized by R'_{HK} . The R'_{HK} index is derived from the S-value to measure chromospheric activity. The S-value is the ratio between the emitted flux in the center of the lines and the continuum flux (Wilson, 1968). Active regions of stars have Ca II H, and K emission lines, and thus R'_{HK} will show variations with the rotation period of the star, which will allow in determining the nature of the RV signal.

2.6 References

- Albrecht S., Reffert S., Snellen I., Quirrenbach A., Mitchell D. S., 2007, *A&A*, 474, 565 25
- Albrecht S., Winn J. N., Butler R. P., Crane J. D., Shectman S. A., Thompson I. B., Hirano T., Wittenmyer R. A., 2012, *ApJ*, 744, 189 25
- Ballot J., García R. A., Lambert P., 2006, *MNRAS*, 369, 1281 23
- Baranne A., et al., 1996, *A&AS*, 119, 373 14, 15
- Boisse I., Bouchy F., Hébrard G., Bonfils X., Santos N., Vauclair S., 2011, *A&A*, 528, A4 29
- Bouchy F., 2006, *Ecole de Goutelas*, 28, 27 16

- Bouchy F, Sophie Team 2006, in Arnold L., Bouchy F, Moutou C., eds, Tenth Anniversary of 51 Peg-b: Status of and prospects for hot Jupiter studies. pp 319–325 [14](#)
- Bouchy F, Isambert J., Lovis C., Boisse I., Figueira P., Hébrard G., Pepe F., 2009a, in Kern P., ed., EAS Publications Series Vol. 37, EAS Publications Series. pp 247–253, [doi:10.1051/eas/0937031](#) [15](#)
- Bouchy F, et al., 2009b, [A&A](#), [505](#), [853](#) [15](#)
- Bouchy F, Díaz R. F., Hébrard G., Arnold L., Boisse I., Delfosse X., Perruchot S., Santerne A., 2013, [A&A](#), [549](#), [A49](#) [14](#)
- Boué G., Montalto M., Boisse I., Oshagh M., Santos N. C., 2013, [A&A](#), [550](#), [A53](#) [25](#)
- Bourrier V., et al., 2015, [A&A](#), [579](#), [A55](#) [27](#)
- Bourrier V., Cegla H. M., Lovis C., Wyttenbach A., 2017, [A&A](#), [599](#), [A33](#) [27](#), [28](#)
- Bourrier V., et al., 2018, [Nature](#), [553](#), [477](#) [27](#)
- Brown D. J. A., et al., 2017, [MNRAS](#), [464](#), [810](#) [25](#), [26](#)
- Cegla H. M., Lovis C., Bourrier V., Beeck B., Watson C. A., Pepe F., 2016a, [A&A](#), [588](#), [A127](#) [27](#)
- Cegla H. M., Oshagh M., Watson C. A., Figueira P., Santos N. C., Shelyag S., 2016b, [ApJ](#), [819](#), [67](#) [25](#), [26](#)
- Christiansen J. L., et al., 2017, [AJ](#), [154](#), [122](#) [19](#)
- Collier Cameron A., Bruce V. A., Miller G. R. M., Triaud A. H. M. J., Queloz D., 2010, [MNRAS](#), [403](#), [151](#) [25](#), [28](#)
- Cosentino R., et al., 2012, in Proc. SPIE. p. 84461V, [doi:10.1117/12.925738](#) [15](#)
- Cosentino R., et al., 2014, in Proc. SPIE. p. 91478C, [doi:10.1117/12.2055813](#) [15](#)
- Crouzet N., et al., 2017, [AJ](#), [153](#), [94](#) [27](#)
- Dalal S., Hébrard G., Lecavelier des Étangs A., Petit A. C., Bourrier V., Laskar J., König P. C., Correia A. C. M., 2019, [A&A](#), [631](#), [A28](#) [26](#), [27](#)
- Dawson R. I., Fabrycky D. C., 2010, [ApJ](#), [722](#), [937](#) [19](#)
- Desidera S., et al., 2003, [A&A](#), [405](#), [207](#) [28](#)
- Díaz R. F., et al., 2012, [A&A](#), [538](#), [A113](#) [16](#)
- Enoch B., et al., 2011, [MNRAS](#), [410](#), [1631](#) [21](#)
- Fabrycky D. C., Winn J. N., 2009, [ApJ](#), [696](#), [1230](#) [25](#)
- Figueira P., et al., 2010, [A&A](#), [513](#), [L8](#) [28](#)
- Fischer D. A., et al., 2008, [ApJ](#), [675](#), [790](#) [19](#)
- Fulton B. J., Petigura E. A., Blunt S., Sinukoff E., 2018, [PASP](#), [130](#), [044504](#) [19](#)
- Gandolfi D., et al., 2012, [A&A](#), [543](#), [L5](#) [27](#)

- Gaudi B. S., Winn J. N., 2007, *ApJ*, **655**, 550 22, 24
- Gazak J. Z., Johnson J. A., Tonry J., Dragomir D., Eastman J., Mann A. W., Agol E., 2012, *Advances in Astronomy*, 2012, 697967 22
- Giménez A., 2006, *A&A*, **450**, 1231 22
- Gizon L., Solanki S. K., 2003, *ApJ*, **589**, 1009 23
- Hébrard G., et al., 2010, *A&A*, **513**, A69 19, 25
- Hirano T., Suto Y., Taruya A., Narita N., Sato B., Johnson J. A., Winn J. N., 2010, *ApJ*, **709**, 458 25
- Hirano T., Suto Y., Winn J. N., Taruya A., Narita N., Albrecht S., Sato B., 2011, *ApJ*, **742**, 69 25
- Holt J. R., 1893, *Astronomy and Astro-Physics (formerly The Sidereal Messenger)*, **12**, 646 21
- Johnson M. C., Cochran W. D., Addison B. C., Tinney C. G., Wright D. J., 2017, *AJ*, **154**, 137 27
- Johnson M. C., et al., 2018, *AJ*, **155**, 100 25, 26
- Kreidberg L., 2015, *PASP*, **127**, 1161 22
- Kürster M., Trifonov T., Reffert S., Kostogryz N. M., Rodler F., 2015, *A&A*, **577**, A103 21
- Mandel K., Agol E., 2002, *ApJ*, **580**, L171 22
- Mayor M., Queloz D., 1995, *Nature*, **378**, 355 19
- Murray C. D., Dermott S. F., 1999, *Solar system dynamics* 17
- Ohta Y., Taruya A., Suto Y., 2005, *ApJ*, **622**, 1118 24
- Pepe F., Mayor M., Galland F., Naef D., Queloz D., Santos N. C., Udry S., Burnet M., 2002, *A&A*, **388**, 632 15
- Pepe F., et al., 2011, *A&A*, **534**, A58 19
- Perruchot S., et al., 2008, in *Proc. SPIE*. p. 70140J, doi:10.1117/12.787379 14
- Perruchot S., et al., 2011, in *Proc. SPIE*. p. 815115 (arXiv:1110.2256), doi:10.1117/12.892466 14
- Perryman M., 2018, *The Exoplanet Handbook* 23
- Pont F., et al., 2009, *A&A*, **502**, 695 25
- Queloz D., Eggenberger A., Mayor M., Perrier C., Beuzit J. L., Naef D., Sivan J. P., Udry S., 2000, *A&A*, **359**, L13 25
- Queloz D., et al., 2001, *A&A*, **379**, 279 16, 28, 29
- Queloz D., et al., 2010, *A&A*, **517**, L1 27, 28
- Reiners A., Mrotzek N., Lemke U., Hinrichs J., Reinsch K., 2016, *A&A*, **587**, A65 25
- Reinhold T., Reiners A., Basri G., 2013, *A&A*, **560**, A4 27

- Reshetov V., Herriot G., Thibault S., Désaulniers P., Saddlemyer L., Loop D., 2012, in Proc. SPIE. p. 84464E, [doi:10.1117/12.927442](https://doi.org/10.1117/12.927442) 15
- Seager S., Mallén-Ornelas G., 2003, *ApJ*, 585, 1038 21
- Ségransan D., et al., 2011, *A&A*, 535, A54 19
- Temple L. Y., et al., 2019, *MNRAS*, 490, 2467 27
- Toner C. G., Gray D. F., 1988, *ApJ*, 334, 1008 29
- Triaud A. H. M. J., 2018, The Rossiter-McLaughlin Effect in Exoplanet Research. p. 2, [doi:10.1007/978-3-319-55333-7_2](https://doi.org/10.1007/978-3-319-55333-7_2) 23, 24
- Wilson O. C., 1968, *ApJ*, 153, 221 29
- Winn J. N., et al., 2006, *ApJ*, 653, L69 25
- Winn J. N., et al., 2007, *AJ*, 133, 1828 23
- Wright J. T., et al., 2013, *ApJ*, 770, 119 16

Chapter 3

A stellar catalog for giant planet detection

“One never notices what has been done, one can only see what remains to be done”

Marie Curie

Contents

3.1 Catalog definition	34
3.1.1 Criterion 1 - Volumetric Constraint	35
3.1.2 Criterion 2- Selection of Main Sequence stars	35
3.1.3 Criterion 3 - Removing SB9 binaries	35
3.1.4 Criterion 4 - Removing CORAVEL binaries and fast rotators	36
3.1.5 Criterion 5 - Removing targets from KECK survey	36
3.1.6 Criterion 6 - Removing targets from ELODIE survey	37
3.1.7 Criterion 7 - Removing known planets	37
3.2 Comparsion with old Catalog	37
3.3 Conclusion	38
3.4 References	38

The SOPHIE exoplanet consortium is devoted to detect and characterize exoplanets, at the Observatoire de Haute Provence since 2006 (Bouchy et al., 2009). It is a continuation of the ELODIE survey for planet-search (Queloz et al., 1998). SOPHIE has many exoplanet detection programs. The goal of one such exoplanet program is to perform a volume-limited survey of giant extra-solar planets, to improve the constraints on the exoplanet parameters and their hosting stars by detecting giant planets. Some of the new detections of giant planets under this program are presented in Chapter 4. At the beginning of the SOPHIE observations, an entrance catalog was created based on the Hipparcos catalog. However, some of its selection criteria were not fully documented, so it is mandatory to well define the entrance catalog for reliable statistics on giant planets. In this chapter, I describe the definition of the new stellar catalog to search and characterize giant planets in the Solar neighborhood. This will help in detecting new giant planets and in building good statistics on giant planets properties.

3.1 Catalog definition

The new catalog definition is adopted similar to the the old catalog definition.

Old Catalog

The old catalog for giant planet was created as follow:

- Targets in Hipparcos catalog up to $d = 70$ pc, with $0.35 < B-V < 2.0$ (F5 to M1) at ± 2 magnitudes from Main Sequence were selected;
- CORAVEL variables, binaries, fast rotators were removed;
- Stars from Keck high-precision program were removed;
- Stars from the first ELODIE program (pp400) were removed;
- Stars with known planets were removed.

In the old catalog, some of the selection criteria were not fully documented, which was the motivation behind creating a new catalog with well-defined criteria as described below.

New Catalog

The new catalog for giant planet is created as follow:

- Targets in Hipparcos catalog up to $d = 60$ pc, with $0.35 < B-V < 1.0$ are selected;
- A new criterion is used for selecting stars around Main Sequence;
- SB9¹ binary stars are removed;
- CORAVEL binaries and fast rotators are removed ;
- Stars from Keck high-precision program are removed;
- Stars from the first ELODIE program (pp400) are removed;
- Stars with known planets are removed.

Below, I describe the steps followed to create a new catalog in more detail.

¹SB9: 9th catalog of Spectroscopic Binary Orbits

3.1.1 Criterion 1 - Volumetric Constraint

Hipparcos (HIP) catalog ([van Leeuwen, 2007](#)) from SIMBAD ([Wenger et al., 2000](#)) is used to create the giant planet catalog for stars in Northern Hemisphere, i.e DEC (declination>0). Table 3.1 gives the list of important parameters obtained from the HIP catalog which will be used to create the giant planet catalog.

Column	Description
_RAJ2000	Right ascension
_DEJ2000	Declination
HIP	Hipparcos identifier
Plx	Parallax
Hpmag	Hipparcos magnitude
B-V	Colour index

Table 3.1 – Parameters obtained from Hipparcos catalog

The list of targets from Simbad was downloaded on 4 November 2019 with $\text{Plx} \geq 16.6667$ mas and $0.35 \leq \text{B-V} < 1.0$. The constraint on parallax is implemented as the giant planet survey is volume-limited. Only targets which are within 60 parsecs of Earth are selected. Similarly, the limits on B-V are set to have bright stars in the sample. The list obtained from Simbad contained 3102 stars.

3.1.2 Criterion 2- Selection of Main Sequence stars

To find main sequence stars, the first step is to calculate the absolute magnitude of the star from its apparent magnitude (Hpmag). The absolute magnitude (\mathcal{M}) can be calculated using:

$$\mathcal{M} = \text{Hpmag} - 5(\log_{10} d_{\text{pc}} - 1) \quad (3.1)$$

where d_{pc} is the distance of the target in parsec, given by $d_{\text{pc}} = 1000/\text{Plx}$.

To select the main-sequence stars, a python Kernel Density Estimator ² is used on the color-magnitude diagram as shown in the Figure 3.1. All the stars shown by white dots in Figure 3.1 that are within 2- σ contour are considered in the Catalog. 2685 targets are within this 2-sigma contour.

New Definition

Before redefining the sample, it is important to note that some of the targets in the SB9 Catalog, CORAVEL and KECK catalog were not observed with Hipparcos. Thus only targets which have HIP identifier are used while comparing these different catalogs with giant planet catalog.

3.1.3 Criterion 3 - Removing SB9 binaries

To remove the spectroscopic binary stars, SB9 and CORAVEL catalog is used. SB9 catalog is downloaded from Simbad ([Pourbaix et al., 2004](#)). After removing the spectroscopic binary using the SB9 catalog, the list has 2441 stars left.

²https://docs.scipy.org/doc/scipy/reference/generated/scipy.stats.gaussian_kde.html

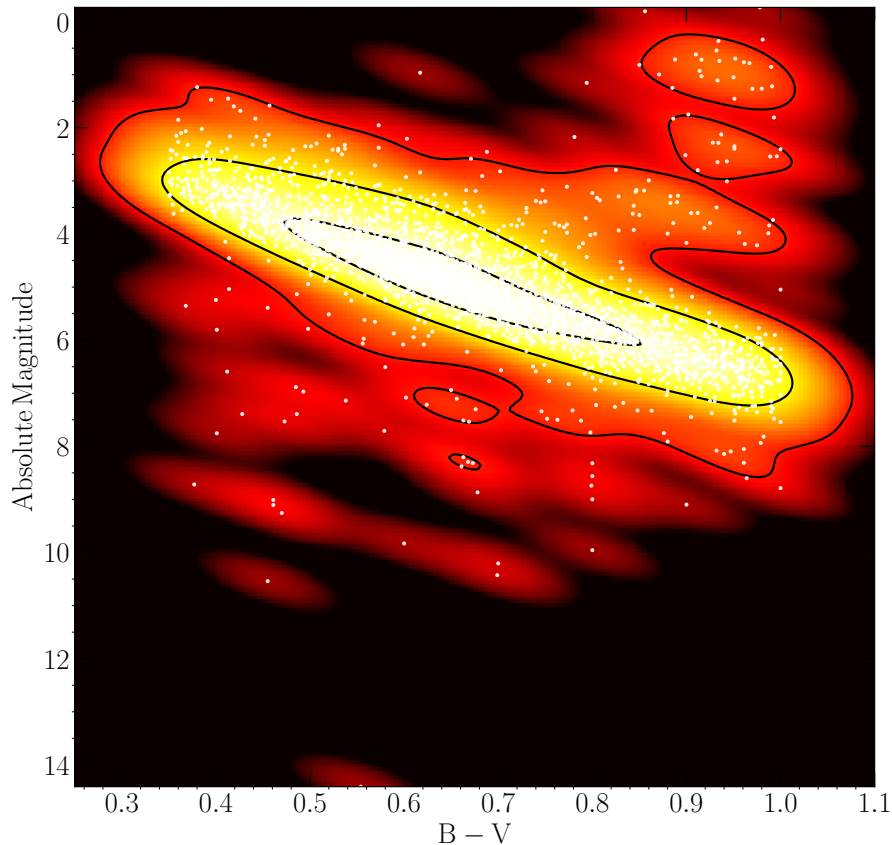


Figure 3.1 – Absolute magnitude versus B-V: The white dots are the targets in the list obtained from SIMBAD and the black lines represents the 1,2 and 3 σ contours after applying Kernel Density Estimator.

3.1.4 Criterion 4 - Removing CORAVEL binaries and fast rotators

CORAVEL catalog had three types of spectroscopic binary stars: SB1 (One lined spectroscopic binary), SB2 (Two-lined spectroscopic binary) and SB3 (Three lined spectroscopic binary stars)

A criterion similar to presented in [Duquennoy et al. \(1991\)](#) is used to define SB1. SB1 are considered to be the stars which have $P(\chi^2) \leq 10^{-4}$ and $E/T \geq 2.0$. Here, $P(\chi^2)$ is the probability that the radial velocity of the star is constant and E/T is the ratio of expected and observed uncertainty on radial velocity (for $N \geq 2$, where N is the number of radial velocity measurements). With the above limits, it is highly likely that the companion is an SB1 which is causing a large variation in the radial velocity.

CORAVEL catalog is also used to remove fast-rotating stars with $V_s \sin I_p \geq 10$ km/s to avoid any radial velocity induced by magnetic activity. It also prevents inaccurate RVs due to the broad CCF. The upper limit is on $V_s \sin I_p$ is adopted from [Saar et al. \(1998\)](#).

After removing SB1, SB2, SB3, and fast rotators of the CORAVEL catalog from the giant planet catalog, 2174 stars left.

3.1.5 Criterion 5 - Removing targets from KECK survey

Some targets had been already observed under different radial velocity surveys are also removed. A total of 1787 stars are left in the giant planet catalog after removing targets of KECK ([Butler et al., 2017](#)) survey.

3.1.6 Criterion 6 - Removing targets from ELODIE survey

Another radial velocity survey that is considered to remove targets that are previously observed is the ELODIE survey. 1626 stars are left in the giant planet catalog after removing targets that were observed using ELODIE.

3.1.7 Criterion 7 - Removing known planets

Targets with known planets are removed using data from Extrasolar Planets Encyclopaedia³. 17 targets were removed using this criterion.

Finally, the new catalog of giant planets has 1609 targets.

3.2 Comparison with old Catalog

The above procedure of catalog definition is also implemented in the old catalog to compare the old and new catalog. However, the old catalog has targets that doesn't satisfy the volume limited criterion i.e. $\text{Plx} \geq 16.6667$ and $0.35 \leq B-V \leq 1.0$. Therefore, before comparing the two catalogs, all the targets which are outside the mentioned range for Plx and B-V are removed. There are 1526 targets in the old catalog.

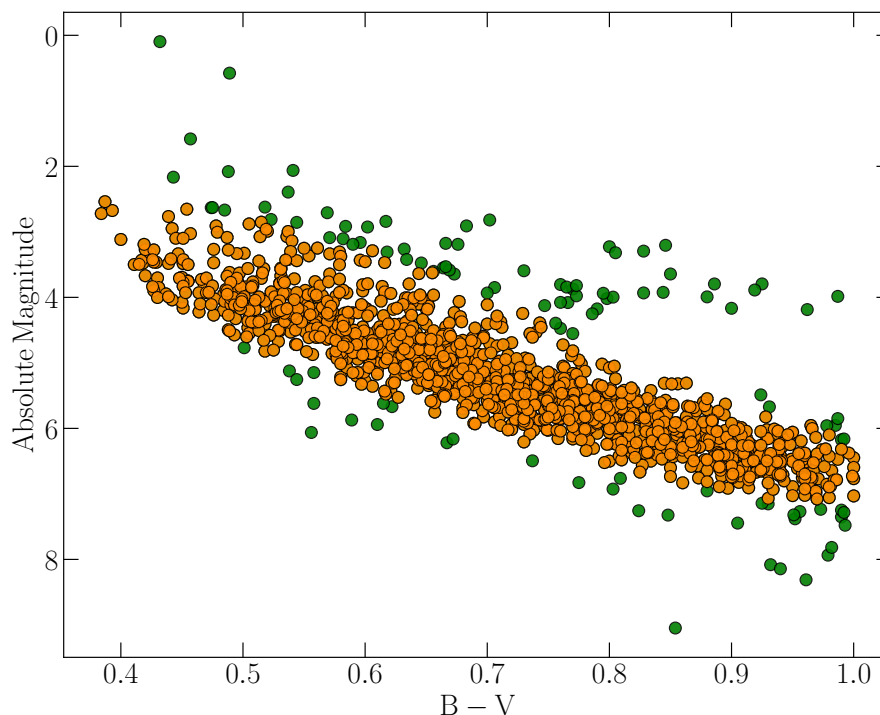


Figure 3.2 – Main sequence selection in old catalog: The orange circles are the selected targets which are within a $2\text{-}\sigma$ density-contour (see Section 3.1.2)

Figure 3.2 shows the selection of the main sequence in the old catalog. To select it, the same $2\text{-}\sigma$ density-contour mentioned in Section 3.1.2 is used. After the procedure of the main sequence in the old catalog, there are 1416 targets left in the old catalog. The next step is to implement the new definition in the old catalog. Finally, the old catalog of giant planets has 1152 targets. A summary of the different criteria on the new and old catalog can be found in Table 3.2.

³<http://exoplanet.eu>, downloaded on Nov 6 2019

Criterion	# of stars in NC	# of stars in OC
Criterion 1	3102	1526
Criterion 2	2685	1416
Criterion 3	2441	1367
Criterion 4	2174	1323
Criterion 5	1787	1167
Criterion 6	1626	1166
Criterion 7	1609	1152

Table 3.2 – Steps followed along with number of stars left after each criterion for the new catalog definition. NC and OC is the new catalog and old catalog, respectively.

3.3 Conclusion

The stellar catalog for giant planets is created with the new definition, has 1609 targets. Out of these 1609 targets, 1152 targets are currently in the old catalog which is used as a giant planet catalog. To complete the volume-limited survey of giant planets, the remaining 457 targets should be observed with SOPHIE. Note that, variable stars are not removed from the new catalog. Therefore, the total targets that are required to observe could be less than 457.

3.4 References

Bouchy F., et al., 2009, *A&A*, **505**, 853 [34](#)

Butler R. P., et al., 2017, *AJ*, **153**, 208 [36](#)

Duquennoy A., Mayor M., Halbwachs J. L., 1991, *A&AS*, **88**, 281 [36](#)

Pourbaix D., et al., 2004, *A&A*, **424**, 727 [35](#)

Queloz D., Mayor M., Sivan J. P., Kohler D., Perrier C., Mariotti J. M., Beuzit J. L., 1998, in Rebolo R., Martin E. L., Zapatero Osorio M. R., eds, *Astronomical Society of the Pacific Conference Series* Vol. 134, *Brown Dwarfs and Extrasolar Planets*. p. 324 [34](#)

Saar S. H., Butler R. P., Marcy G. W., 1998, *ApJ*, **498**, L153 [36](#)

Wenger M., et al., 2000, *A&AS*, **143**, 9 [35](#)

van Leeuwen F., 2007, *A&A*, **474**, 653 [35](#)

Chapter 4

New Detections

“ Science progresses best when observations force us to alter our preconceptions. ”

Vera Rubin

Contents

4.1 Motivation	40
4.1.1 Giant Planets	40
4.1.2 Brown Dwarfs	42
4.2 Observations, Data Reduction and Keplerian fit	44
4.3 New Detections	45
4.3.1 Giant planets without drifts	45
4.3.2 Giant planets with drifts	49
4.3.3 Brown Dwarfs	50
4.3.4 Stellar Companions	50
4.4 False Positive Indicator Analysis	53
4.5 Summary and Conclusion	54
4.6 References	56

SOPHIE is devoted to detect and characterize exoplanets at the Observatoire de-Haute Provence (OHP) since 2006 (Bouchy et al., 2009). The two SOPHIE exoplanet consortium programs on which I mostly worked to detect new companions (planets, brown dwarfs, and stellar companions) are as explained below.

- **Volume-limited Survey of Giant planets:** This ongoing program aims to increase the number of detections of giant planets orbiting nearby bright stars. Under this program, some particular cases are identified for follow-up studies: multi-planetary systems for dynamics and transiting systems for structure characterization. This survey will help improve the statistics on the occurrence and properties of giant planets as a function of stellar properties. The new detections will help explore the new properties in the distribution of exoplanet parameters, which allows us to understand diverse planetary systems.
- **Brown Dwarf Survey:** The goal of the brown dwarf program with SOPHIE is to perform a meaningful unbiased statistic survey of companions detected within and about the brown-dwarf mass regime, and having up to 10 yrs period. It is important to identify and characterize new brown dwarfs to compare the statistics of different parameters of giant planets and brown dwarfs. Furthermore, stellar companions with $m \sin I_p > 90M_J$ are also characterized under brown dwarf program. It allows us to explore the connections between massive brown dwarfs and low-mass stellar companions.

In this chapter, I present the detection of six new cool Jupiters, six new brown dwarfs, and fifteen low-mass stellar companions, which will be published in the forthcoming paper (Dalal et al., 2020, in prep.). Furthermore, I have also visited OHP and performed observation with SOPHIE for seven weeks, spread over 2.5 years.

4.1 Motivation

The statistics on the occurrence and properties of brown dwarfs and giant planets bear a wealth of information about their formation mechanisms. The following sections describe how discoveries of giant planets and brown dwarfs will contribute to exoplanetary science.

4.1.1 Giant Planets

As defined before, Giant planets are the massive planets with substantial envelopes of H/He, similar to solar system giant planets. Despite the discovery of thousands of giant exoplanets, their formation mechanism is still not properly understood. The two formation models that are proposed for giant planets formation are core accretion and disk instability. The dominant mechanism is core accretion (Guilera et al., 2010; Mordasini et al., 2009; Pollack et al., 1996), where a giant planet is formed when a massive (10-20 M_{\oplus}) enough planetary embryo accretes gas from the nebula. In the latter scenario, i.e., disk instability (Boss, 2011; Cai et al., 2010), a proto-planetary disk fragments into planet-sized, self-gravitating clumps.

Although there are more than 4000 exoplanets detected so far, new exoplanet discoveries can still baffle astronomers. Recently, the discovery of a massive exoplanet ($m=0.46 M_J$) orbiting an M5 dwarf GJ 3512 ($M=0.12 M_{\odot}$) challenged giant planet formation models (Morales et al., 2019). The important clues for giant planet formations are hidden in the observed orbital distributions of giant planets. For example, Santos et al. (2017) studied the mass distribution of giant planets and suggested that giant planets with masses above and below $\sim 4 M_J$ may represent two different populations that are formed by different physical processes. For giant planets with mass $< 4 M_J$ or

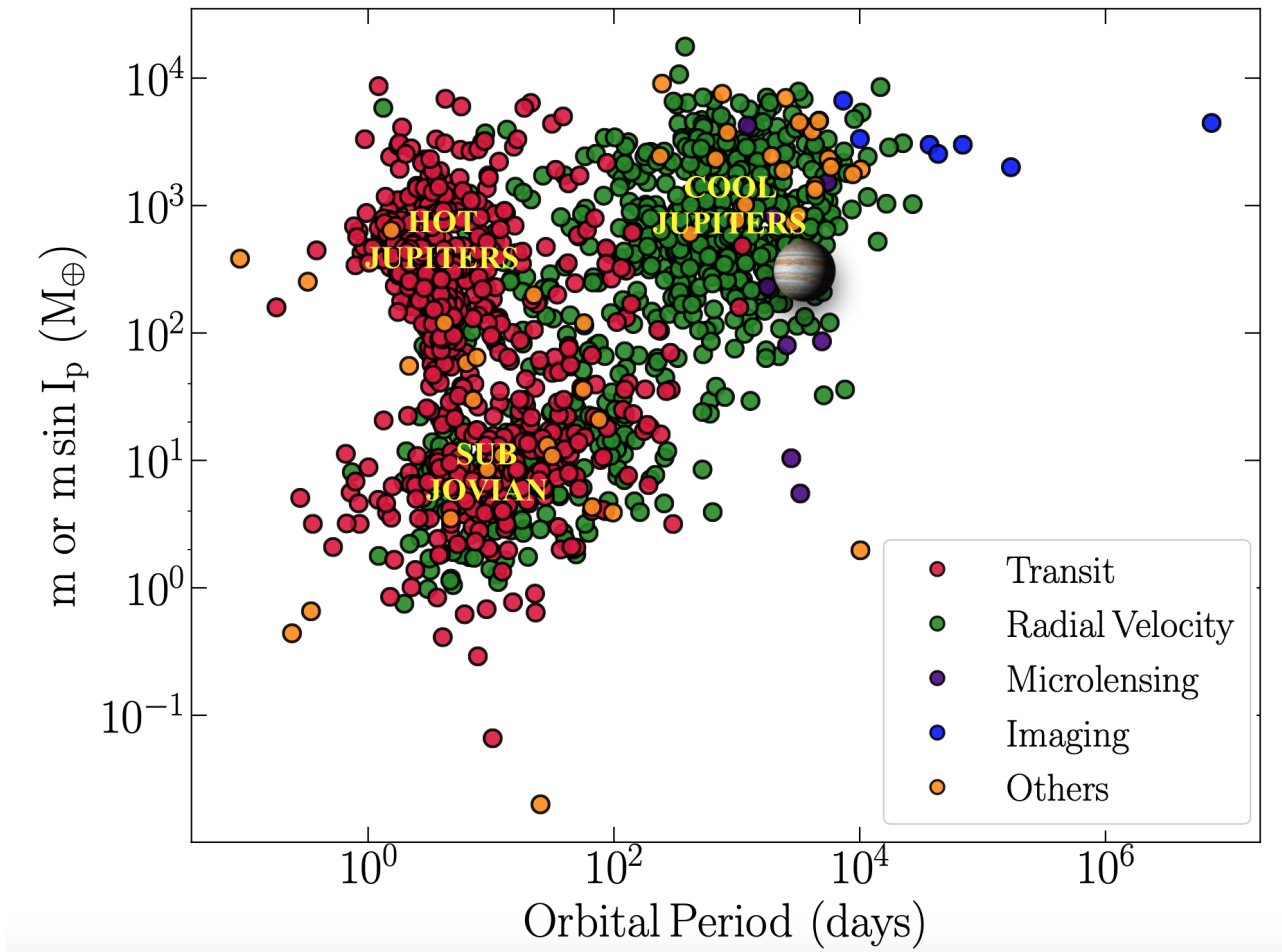


Figure 4.1 – Period-Mass distribution of the confirmed exoplanets: Two different population of giant planets i.e. hot jupiters and cool jupiters are labeled.

mass $> 4 M_J$, the formation process would be most likely core accretion or disk instability, respectively. Recently, [Fernandes et al. \(2019\)](#) found that the giant planet occurrence rate falls off at the snow line by analyzing their occurrence rates as a function of the orbital period. Additional clues about planet formation can be obtained by studying the planetary system properties along with the occurrence rate.

The most popular giant planets are hot Jupiters (HJs). HJs are the giant planets orbiting its host star in less than ten days. The name itself suggests that they have a high equilibrium temperature, reaching values close to 1500 K for separation of 0.05 AU from a solar-type star. These are the first exoplanets to be discovered around main-sequence stars, and only 1% of the solar-type stars hosts HJs ([Howard et al., 2010](#); [Wright et al., 2012](#)). The classical theory of planet formation predicts the giant planets to form and evolve in orbits beyond the snow line. The discovery of HJs was a huge surprise for astronomers as they do not conform with the classical planet formation theories. To explain the origin of HJs, there are currently three proposed mechanisms: in-situ formation, disk migration, and high eccentricity migration (see review by [Dawson & Johnson 2018](#)). But there are still debates about the origin of HJs. Besides HJs, the second class of giant exoplanets is cool Jupiters (CJs) i.e., giant planets having a mass greater than $0.3 M_J$ with an orbital period longer than 100 days¹. Recently, [Wittenmyer et al. \(2020\)](#) found that CJs are more abundant than HJs. They found that CJs occurrence rate is $6.73^{+2.09}_{-1.13}$ per cent whereas HJs occurrence rate is just $0.84^{+0.70}_{-0.20}$.

¹Definition adopted from [Wittenmyer et al. \(2020\)](#)

Given that giant planet of our Solar System widely influence the dynamical history of our Solar System (see [Morbidelli et al., 2007](#); [Raymond & Izidoro, 2017](#)), it is important to detect and study these long-period giant planets. Cool Jupiters that are analogous to Jupiter and Saturn are the best candidates for such studies.

In this context, detecting and characterizing new giant planets will provide stringent constraints on their formation and evolution models. Figure 4.1 shows HJs and CJs on the period-mass distribution of the confirmed exoplanets. It is clear from the figure that it is possible to detect CJs using long term radial velocity surveys. The ongoing radial velocity (volume-limited) survey of giant planets with SOPHIE data (14 years) combined with ELODIE data (10 years), is suitable for detecting CJs.

4.1.2 Brown Dwarfs

Brown dwarfs are sub-stellar objects that occupy a regime between the high mass gas giant planets and the low mass stars. The figure 4.2 shows the life cycle of brown dwarfs on the Hertzsprung–Russell (HR) diagram². Brown dwarfs (wannabe stars) do not emit in the visible range of electromagnetic spectrum. Unlike main sequence stars, they are not massive enough to sustain nuclear fusion of ordinary hydrogen to helium in their cores. However, they are massive enough to ignite Deuterium (^2H) nuclear reactions in their cores.

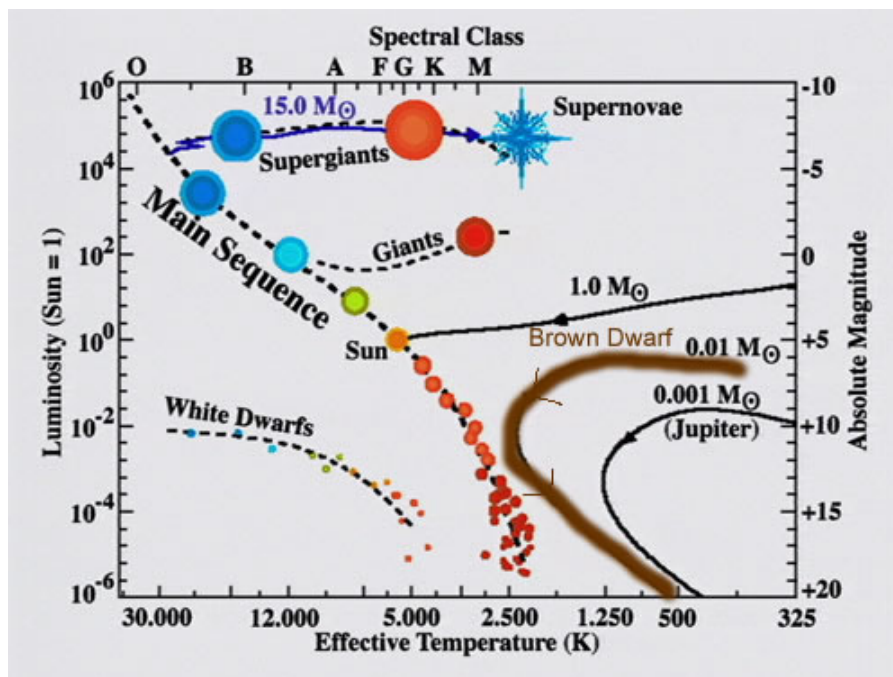


Figure 4.2 – The life cycle of brown dwarfs highlighted with the thick brown line on the HR diagram.

The lower mass limit that separates brown dwarfs from planets comes from the threshold required to fuse deuterium in the core of the brown dwarfs, i.e., $13 M_{\text{J}}$. The upper mass limit of brown dwarfs corresponds to the threshold to fuse hydrogen in the core, i.e., $80 M_{\text{J}}$ ([Hayashi & Nakano, 1963](#)). Both the lower and upper mass limits are susceptible to the metallicity. [Spiegel et al. \(2011\)](#) reported that the lower mass limit on brown dwarf could vary from $11 - 16 M_{\text{J}}$ depending on the metallicity. Similarly, the upper mass limit vary according to metallicity from 83 to $75 M_{\text{J}}$ within $M/H \sim [-1; 0]$ ([Chabrier & Baraffe, 1997](#)).

²http://astro.hopkinsschools.org/course_documents/stars/faintest_and_coolest/brown%20dwarfs/brown_dwarf.htm

The dearth in the detection of brown-dwarfs at an orbital separation of < 5 A.U, (Grether & Lineweaver, 2004; Marcy & Butler, 2000) also known as the brown dwarf desert (see figure 4.3). The presence of this brown dwarf desert tends to suggest different formation scenarios for giant planets and brown dwarfs: core accretion for planets and molecular cloud instability for brown dwarfs.

The statistics of observed brown dwarf companions are still poor. It is, therefore, crucial to identify new brown dwarfs. It has been established that the observed distribution of orbital elements and frequency helps in understanding and distinguishing between different formation and evolution models. For example, the eccentricity distribution of brown dwarf companions with mass $\leq 40 M_J$ is consistent with the eccentricity distribution of massive planets (Ma & Ge, 2014). Apart from that, different planet-formation models allows the formation of bodies up to $40 M_J$ (Albert et al., 2005; Ida & Lin, 2004; Mordasini et al., 2009). This suggests that brown dwarfs $\leq 40 M_J$ might have a similar formation mechanism as massive planets. Ma & Ge (2014) also reported that the massive brown dwarfs' eccentricity distribution was consistent with the binaries. They concluded that high mass brown dwarfs are likely to form in the same way as low mass stars.

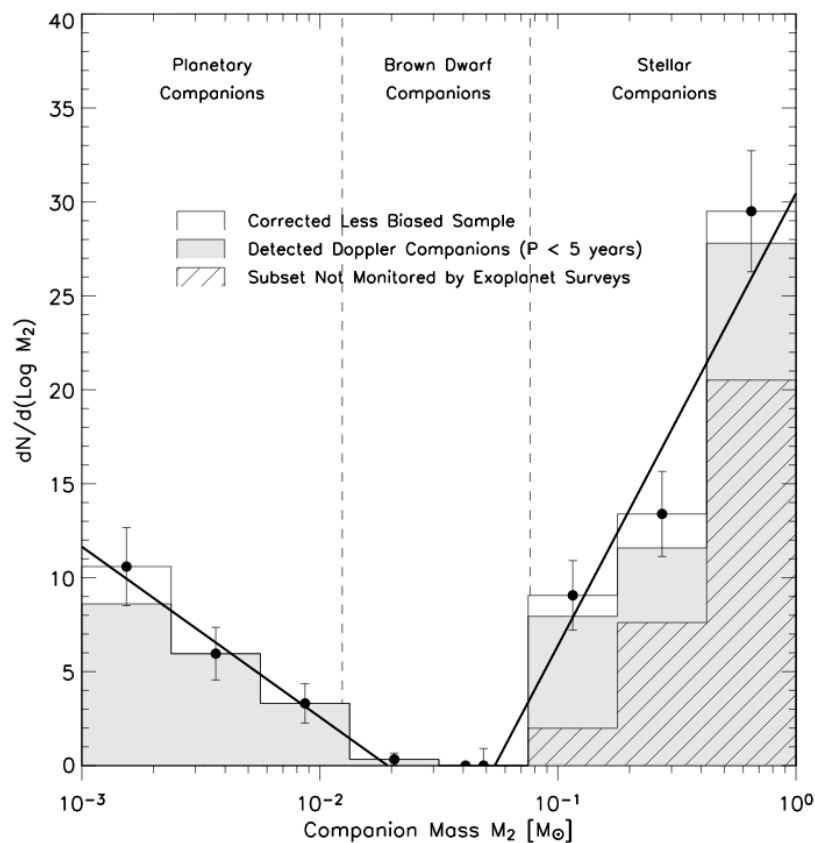


Figure 4.3 – The mass distribution of Brown dwarfs and planets on both sides of the brown dwarf desert in a 60 pc volume-limited sample around the Sun. (Grether & Lineweaver, 2006)

In this context, the detection of new brown dwarf companions is important. Owing to the large reflex motion brown dwarf companions induce in the stars, it is relatively easy to detect them with the radial velocity method. There have been several radial velocity surveys to detect brown dwarfs that also confirmed the brown dwarf desert (e.g. Borgniet et al., 2017; Grether & Lineweaver, 2006; Ma & Ge, 2014; Sahlmann et al., 2011a). However, the RV method only provides a lower limit for the mass. So, it is likely that the fraction of the brown dwarf candidates detected by RV surveys is low-mass stars with low orbital inclination. To determine their true mass accurately, astrometry

can be used (Kiefer et al., 2019; Sahlmann et al., 2011b). One of the ongoing radial velocity surveys for brown dwarfs in the Northern hemisphere is with SOPHIE at OHP (Bouchy et al., 2016; Díaz et al., 2012; Kiefer et al., 2019; Santerne et al., 2016; Wilson et al., 2016).

4.2 Observations, Data Reduction and Keplerian fit

The spectra of all the stars presented in this chapter were obtained with SOPHIE at the 1.93 m telescope of the OHP, France (Bouchy et al., 2009; Perruchot et al., 2008). Observations were taken in the fast-reading mode of the detector and high-resolution ($R = 75000$) mode of the spectrograph. The sky or moonlight pollution is evaluated by placing one of the optical fibers on the sky and the other on starlight. Most of the spectra for the giant planet detection program have a typical signal-to-noise ratio (SNR) per pixel of 50.8 at a wavelength of 550 nm. However, for the brown dwarf and stellar companion detection, the typical signal-to-noise ratio (SNR) per pixel at 550 nm is 43.6 and 41.6. Wavelength calibrations were performed at the beginning and end of each observing night, and approximately every two hours during the night. Two distinct datasets are considered for the data taken using SOPHIE, namely SOPHIE and SOPHIE+, depending on whether the spectra were taken before or after the SOPHIE upgrade of June 2011 (Bouchy et al., 2013).

The SOPHIE pipeline is used for extracting the spectra and cross-correlating them with numerical mask (Bouchy et al., 2009). The cross-correlation functions (CCFs) are produced by considering masks corresponding to their stellar type and incorporating all of the spectral orders. The CCFs were then fitted with Gaussians to derive the radial velocities (RVs) (Baranne et al., 1996; Pepe et al., 2002). The spectra with SNR less than 25 and with significant sky background pollution are removed from further analysis. The obtained RVs are also corrected for the CTI effect using an empirical relation. A quadratic uncertainty of 5 ms^{-1} is added to the uncertainty in RV measurements taken with SOPHIE before the June 2011 upgrade to account for the poor scrambling properties for the exposures.

Keplerian Fit

To fit a Keplerian orbit in the observed radial velocities of each star, the software yorbit (Bouchy et al., 2016; Ségransan et al., 2011) is used. Yorbit uses a genetic algorithm to refine initial parameters for a Levenberg-Marquardt optimization, which leads to the priors for a Markov chain Monte Carlo (MCMC) estimation of error bars following Díaz et al. (2014). The MCMC was applied on 1000 iterations. While fitting the Keplerian, the following parameters are varied: P , K , e , ω , T_0 , and the radial velocity offsets, γ_S and γ_{S+} for SOPHIE and SOPHIE+ datasets, respectively (see Table 2.2 for meaning of these symbols). T_0 is the time at periastron for eccentric orbit and time of possible transit for the circular or nearly circular orbits as the time of periastron passage is ill-defined for $e \sim 0$. Additionally, linear and quadratic drifts are also allowed for some targets, which showed drifts in the residual radial velocity.

The Keplerian solution for all the stars is obtained by considering one planet model except for HD 124330 and BD +550362. A linear and quadratic drift is considered for HD 124330 and BD +550362, respectively, while fitting Keplerian. The derived orbital parameters of each target are discussed below. The uncertainties on $m \sin I_p$ and a are mainly due to the uncertainties on the host star masses.

4.3 New Detections

4.3.1 Giant planets without drifts

A summary of the Keplerian orbit parameters along with $m \sin I_p$, a , and dispersion of residuals for the newly detected planets without drifts can be found in Table 4.1. Figure 4.4 shows the observed radial velocity measurements along with the best-fit Keplerian model and residuals. The phase folded curve for each target is also plotted in the right panel.

BD +450564

BD +450564 is a K1 type star which has a mass of $0.81 \pm 0.07 M_\odot$ and $\log R'_{\text{HK}}$ of -4.98. It was observed with SOPHIE after the upgrade, and the final dataset has 16 SOPHIE+ RV measurements. The Lomb-Scargle periodogram shows a peak of around 300 days. The Keplerian fit of the 16 radial velocities provides a period of 307.7 ± 1.2 days and gives a semi-amplitude of $47.4 \pm 2.3 \text{ ms}^{-1}$ which corresponds to a minimum mass, $m \sin I_p = 1.36 \pm 0.11 M_J$. BD +450564 b orbits its host star in a nearly circular orbit with $e = 0.09 \pm 0.05$. The residual radial velocities have a dispersion of 3.21 ms^{-1} , which is in agreement with the typical uncertainty on the RVs.

HD 155193

HD 155193 is a F8IV type star which has a mass $1.22 \pm 0.08 M_\odot$ and $\log R'_{\text{HK}} = -5.14$. It was observed with SOPHIE after the upgrade, and 78 radial velocity measurements were acquired. The Lomb-Scargle periodogram shows a peak of around 350 days. The one-planet Keplerian fit of the radial velocities gives a semi-amplitude of $19.3 \pm 1.2 \text{ ms}^{-1}$ which corresponds to a minimum mass, $m \sin I_p = 0.75 \pm 0.06 M_J$. HD 155193 b has an orbital period of 352.8 ± 2.5 days and has a significant eccentricity of $e = 0.21 \pm 0.08$. The residuals show a dispersion of 6.9 ms^{-1} , which is slightly higher than the accuracy of the measurements.

HD 204277

The star HD 204277 is an F8V type star with a mass of $1.14 \pm 0.08 M_\odot$. It shows high activity levels with $\log R'_{\text{HK}} = -4.50$. The star was observed only after the SOPHIE upgrade, and 96 RVs were secured. The Lomb-Scargle periodogram shows a clear peak around 250 days. The Keplerian fit of the radial velocities gives a semi-amplitude of $20.1 \pm 4.8 \text{ ms}^{-1}$ and an orbital period of 252.7 ± 4.8 days. This fit corresponds to a planet with minimum mass, $m \sin I_p = 0.61 \pm 0.08 M_J$. Significant eccentricity is detected with $e = 0.41 \pm 0.15$ for the planet. The residual radial velocities have a high dispersion of 11.08 ms^{-1} , which may result from its high activity levels. Further analysis is done to confirm the origin of this signal, and it is found that the radial velocity variation is not due to a planet (4.4).

HD 331093

HD 331093 is a K0 type star which has a mass of $1.03 \pm 0.08 M_\odot$ and $\log R'_{\text{HK}} = -5.10$. It was observed before and after the SOPHIE upgrade, and 21 radial velocity measurements were acquired. The Keplerian fit of the radial velocities gives an orbital period of 619.8 ± 15.4 days and a high eccentricity of $e = 0.59 \pm 0.03$. The fit has a semi-amplitude of $43.8 \pm 2.3 \text{ ms}^{-1}$ which corresponds to a minimum mass, $m \sin I_p = 1.51 \pm 0.11 M_J$. The residuals show a dispersion of 3.34 and 3.58 ms^{-1} for SOPHIE+ and SOPHIE, respectively, which is in agreement with the typical uncertainty on the RVs.

BD +631405

The star BD +631405 is a K0 type star with a mass of $0.82 \pm 0.08 M_{\odot}$ and has low activity levels ($\log R'_{\text{HK}} = -4.98$). It was also observed before and after the SOPHIE upgrade and 21 RVs were secured. The one-planet Keplerian fit of the radial velocities provides an orbital period of 1196.8 ± 50.3 days and a high eccentricity, $e = 0.88 \pm 0.02$. The semi-amplitude, $185.2 \pm 13.5 \text{ ms}^{-1}$ of the Keplerian fit corresponds to a planet with minimum mass, $m \sin I_p = 3.96 \pm 0.31 M_{\text{J}}$. The residuals show a dispersion of 4.3 and 7.0 ms^{-1} for SOPHIE+ and SOPHIE respectively, which is in agreement with accuracy of the RV measurements.

Figure 4.4: Keplerian orbit of the radial velocity variations for BD +450564, BD +631405, HD 155193, HD 204277 and, HD 331093 are plotted here. The left panel shows the RV vs time with O-C residuals below and RV vs phase is on the right panel. SOPHIE+ measurements are plotted in red circles. If the target is observed before and after the upgrade, SOPHIE and SOPHIE+ measurements are plotted in red circles and blue squares simultaneously.

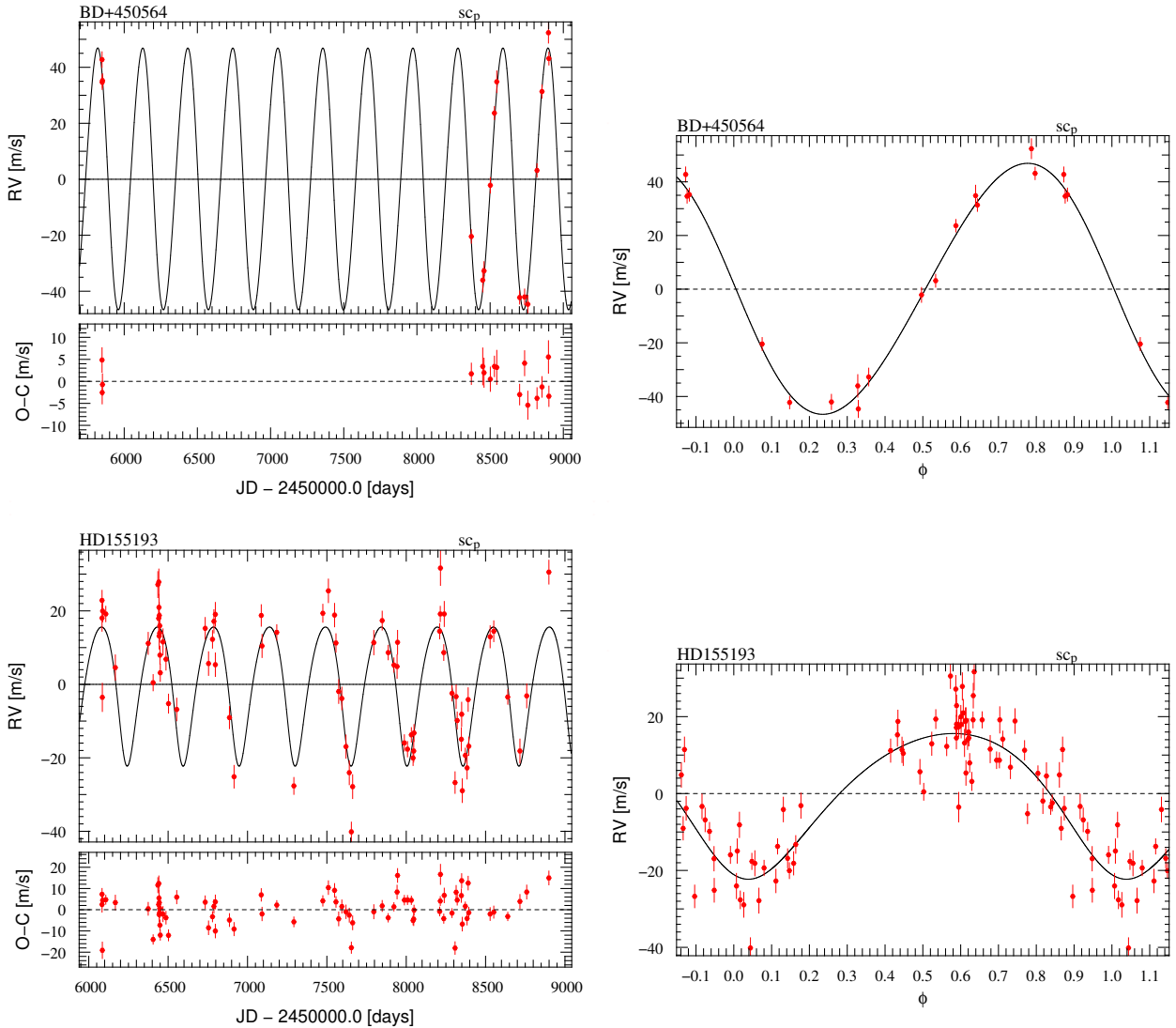


Figure 4.4: Continued.

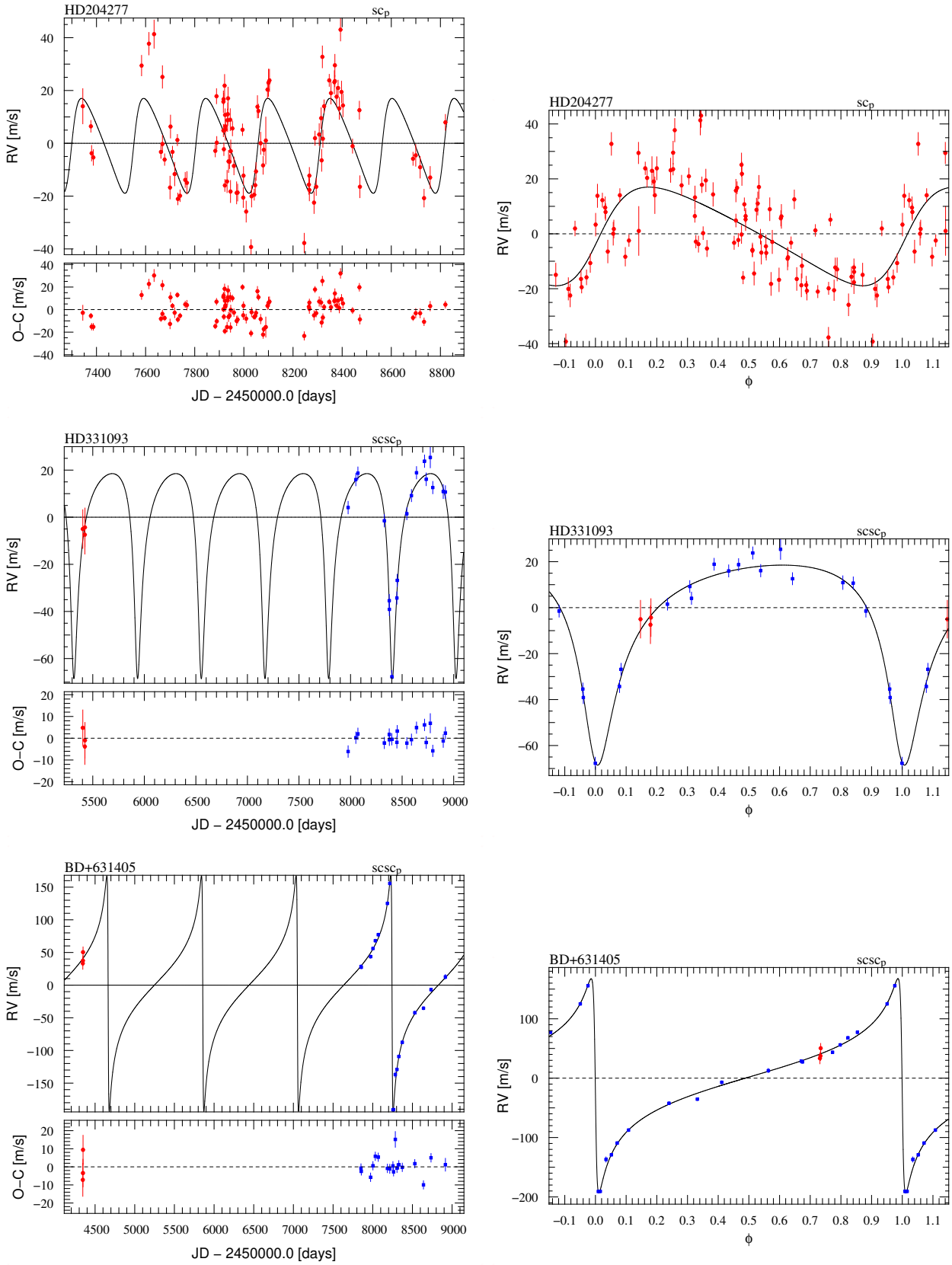


Table 4.1 – Table of Keplerian solution for BD +450564, BD +631405, HD 155193, HD 204277 and, HD 331093. The uncertainty on stellar mass was quadratically added to calculate the uncertainty on $m \sin I_p$ and a . SOPHIE measurements taken after the instrument upgrade in June 2011 are referred as S+.

Parameters	Unit	BD +450564	BD +631405	HD 155193	HD 204277	HD 331093
P	days	307.734±1.203	1196.85±50.306	352.785±2.472	252.776±4.788	619.77±15.424
K	ms ⁻¹	47.385±2.349	185.181±13.523	19.343±1.244	20.151±4.797	43.786±2.268
e	-	0.098±0.053	0.881±0.018	0.206±0.076	0.409±0.148	0.591±0.026
ω	(°)	72.267±47.332	94.338±3.453	72.207±134.201	-88.024±39.038	165.025±26.963
T0	days	58329.0567005±4.627	59437.8837289±4.631	57636.3641026±7.318	57787.0087954±26.354	59020.4951895±15.61
N _S	-	0	3	0	0	3
N _{S+}	-	16	18	78	96	18
γ_{S+}	km s ⁻¹	-6.817±0.002	-15.33±0.013	3.883±0.001	9.331±0.008	-51.32±0.003
γ_S	km s ⁻¹	-	-15.437±0.045	-	-	-51.285±0.02
$\sigma_{O-C, S+}$	ms ⁻¹	3.21	4.32	6.9	11.08	3.34
$\sigma_{O-C, S}$	ms ⁻¹	-	7.0	-	-	3.58
$m \sin I_p$	M _J	1.358±0.111	3.955±0.311	0.749±0.06	0.606±0.079	1.51±0.112
a	A.U.	0.832±0.045	2.064±0.139	1.044±0.045	0.817±0.036	1.437±0.072

4.3.2 Giant planets with drifts

A summary of the Keplerian orbit parameters for BD +550362 and HD 124330 is given in Table 4.2. A quadratic and linear drift model, along with the one-planet model, is considered for BD +550362 and HD 124330. Figure 4.5 shows the observed radial velocity measurements along with the best-fit Keplerian model and residuals. The phase folded curve for each target is also plotted on the right panel.

BD +550362

BD +550362 is a K3 type star which has a mass of $0.91 \pm 0.10 M_{\odot}$ and $\log R'_{\text{HK}} = -5.11$. It was observed after the SOPHIE upgrade, and 26 radial velocity measurements were obtained. The Lomb-Scargle periodogram shows a clear peak of around 260 days. The Keplerian fit of the radial velocities gives a semi-amplitude of $24.8 \pm 1.4 \text{ ms}^{-1}$ which corresponds to a minimum mass, $m \sin I_p = 0.70 \pm 0.07 M_{\text{J}}$. BD +550362 b has an orbital period of 260.2 ± 0.8 days and has significant eccentricity of $e = 0.28 \pm 0.05$. The residuals show a dispersion of 3.8 ms^{-1} , which is in agreement with the accuracy of the RV measurements. Apart from the one-planet model, the radial velocity also shows a quadratic drift of $2.27 \text{ ms}^{-1}\text{yr}^{-2}$. Assuming a circular orbit for the additional companion, the shift would correspond to an orbital period of at least 4050 days and a mass of at least $3.5 M_{\text{J}}$. Other solutions from the data, with longer periods and higher masses, are also possible for the different values of eccentricity.

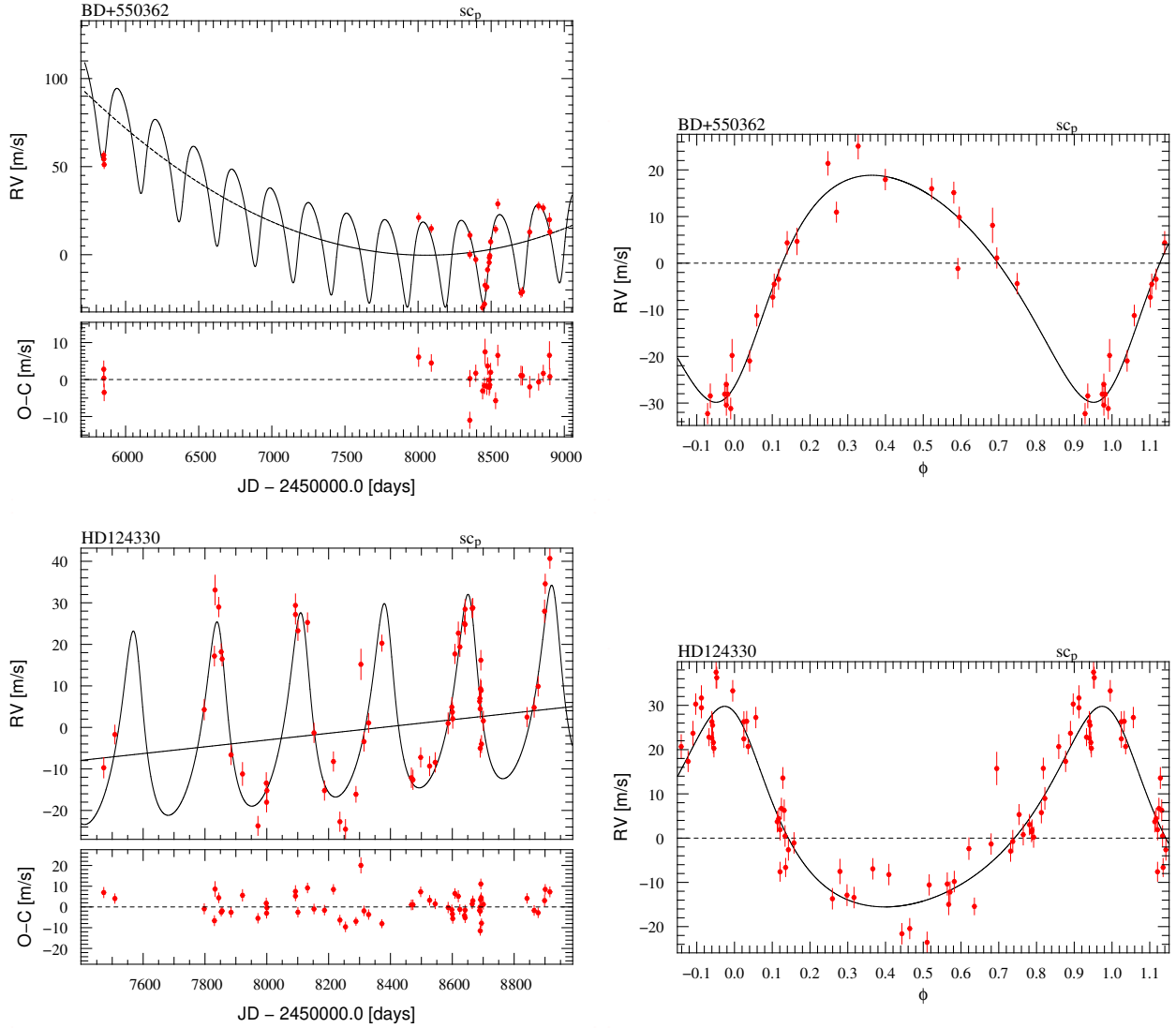
HD 124330

The HD 124330 is a G4IV type star which has a mass of $1.15 \pm 0.08 M_{\odot}$ and $\log R'_{\text{HK}} = -5.27$. Sixty radial velocity measurements were secured after the SOPHIE upgrade. The Lomb-Scargle periodogram shows a clear peak of around 270 days. The Keplerian fit of the radial velocities gives a significant eccentricity, $e = 0.34 \pm 0.04$ for the planet, and an orbital period of 270.6 ± 1.2 days. This Keplerian has a semi-amplitude of $22.78 \pm 1.19 \text{ ms}^{-1}$, which corresponds to a planet of mass $m \sin I_p = 0.75 \pm 0.06 M_{\text{J}}$ that orbits its host star in 270.58 days. The residuals show a dispersion of 5.4 ms^{-1} , which is slightly higher than the accuracy of the RV measurements. Apart from that, the radial velocity also shows a linear shift of $2.98 \text{ ms}^{-1}\text{yr}^{-1}$. Assuming a circular orbit, the shift would correspond to a planet with an orbital period of at least 6100 days and a mass of at least $0.69 M_{\text{J}}$. Other solutions for the mass and orbital period are also possible for the different values of eccentricity.

Parameter	Unit	BD +550362	HD 124330
P	days	260.249 ± 0.835	270.577 ± 1.162
K	ms^{-1}	24.771 ± 1.425	22.782 ± 1.195
e	-	0.275 ± 0.051	0.338 ± 0.04
ω	($^{\circ}$)	-143.297 ± 50.287	18.634 ± 9.968
T0	days	58246.763 ± 6.812	58394.738 ± 2.756
$m \sin I_p$	M_{J}	0.702 ± 0.072	0.749 ± 0.058
a	A.U.	0.773 ± 0.051	0.858 ± 0.037
$N_{\text{S}+}$	-	26	60
$\gamma_{\text{S}+}$	kms^{-1}	-25.648 ± 0.002	2.978 ± 0.051
$\sigma_{\text{O-C, S}+}$	ms^{-1}	3.83	5.36
RV Drift	-	Quadratic ($2.27 \text{ ms}^{-1}\text{yr}^{-2}$)	Linear ($2.98 \text{ ms}^{-1}\text{yr}^{-1}$)

Table 4.2 – Keplerian solutions of the radial velocity variations of the BD +550362 and HD 124330.

Figure 4.5: Keplerian orbit of the radial velocity variations for BD +550362 and HD 124330 are plotted here. The left panel shows the RV vs time with O-C residuals below and RV vs phase is on the right panel. SOPHIE+ measurements are plotted in red circles.



4.3.3 Brown Dwarfs

Out of the six new brown dwarf candidates, four of them have mass $m \sin I_p \leq 80 M_J$ and the remaining two brown dwarf candidates lie in the transition zone between the upper-limit of brown-dwarfs and the lower-limit of M-dwarf, 80–90 M_J . The results from the Keplerian fit are presented in Table 4.3 and the Keplerian fit are shown in Figure A.1 in Appendix A.

4.3.4 Stellar Companions

15 stellar companions are detected with SOPHIE. All of them have mass $m \sin I_p > 90 M_J$ and have period longer than 300 days except for HD 151465 and HD 153915. The results from the Keplerian fit is presented in Table 4.4 and the Keplerian fit are shown in figure A.2 in the Appendix A.

Table 4.3 – Table of Keplerian fits for the 6 Brown Dwarfs with mass $20 \leq m \sin I_p \leq 90 M_{\text{Jup}}$. The uncertainty on stellar mass was quadratically added to calculate the uncertainty on $m \sin I_p$ and a . SOPHIE measurements taken after the instrument upgrade in June 2011 are referred as S+. T0 is the time of passage at periastron for eccentric brown dwarfs and T0 is the time of primary transit for circular or nearly circular brown dwarfs.

* - HD 187057 is considered in brown dwarf and low mass stars grey zone (80–90 M_J) as the uncertainty on its mass is quite high.

Name	Unit	BD-004475	HD 166356	HD 184601	HD 205521	HD 5433	HD 187057*
P	days	723.718±1.026	261.541±0.061	849.224±1.356	2031.688±3.788	576.353±1.567	48.401±0.002
K	ms^{-1}	739.902±14.575	2756.747±16.097	1531.12±16.628	405.566±009.00	2088.701±163.753	4317.915±5.024
e	-	0.387±0.012	0.453±0.004	0.49±0.005	0.17±0.013	0.813±0.016	0.098±0.001
ω	(°)	-93.695±2.983	95.544±0.398	137.653±0.691	-139.574±4.831	77.062±3.491	-108.946±0.718
T0	days	58804.726±4.130	58341.603±0.156	58480.304±1.031	58469.052±21.180	58031.929±0.273	58352.826±0.097
$\Upsilon_{\text{S+}}$	km s^{-1}	23.603±0.022	-6.279±0.012	-63.487±0.02	-7.961±0.009	30.965±0.16	21.843±0.006
Υ_{S}	km s^{-1}	23.617±0.030	-6.25±0.035	-	-	30.975±0.191	21.782±0.096
$\sigma_{\text{O-C, S+}}$	ms^{-1}	11.09	11.13	7.45	4.27	9.37	5.23
$\sigma_{\text{O-C, S}}$	ms^{-1}	5.72	12.96	-	-	17.14	10.01
$m \sin I_p$	M_J	26.138±2.325	90.6±5.2	60.248±3.64	26.534±1.717	49.028±3.411	91.859±5.135
a	A.U.	1.484±0.105	0.885±0.039	1.761±0.08	3.265±0.15	1.368±0.06	0.29±0.012

Table 4.4 – Table of orbital fits for the stellar Companion with $M \sin i > 90 M_{\text{Jup}}$. The error on stellar mass was added to calculate the uncertainty on $M_2 \sin i$ and a . SOPHIE measurements after the instrument upgrade in June 2011 are referred as S+. The uncertainties on $m \sin I_p$ and a are mainly due to the uncertainties on the host-star masses.

Name	Period (day)	K (m s^{-1})	e	ω ($^\circ$)	T0 (day)	$m \sin I_p$ (M_{Jup})	a (AU)
BD +031552	879.034 ± 0.39	3432.224 ± 8.26	0.473 ± 0.002	-35.428 ± 0.616	$57630.2545322 \pm 1.3041277$	133.293 ± 49.052	1.814 ± 0.577
HD 140208	326.422 ± 0.02	8807.016 ± 12.93	0.281 ± 0.003	-176.181 ± 0.587	$57564.8367537 \pm 0.3640253$	324.27 ± 18.512	1.065 ± 0.046
HD 151465	54.439 ± 0.002	6066.407 ± 19.206	0.243 ± 0.005	24.948 ± 0.697	$57984.7754352 \pm 0.1526895$	122.553 ± 7.186	0.307 ± 0.014
HD 153915	30.131 ± 0.0	5860.87 ± 3.897	0.036 ± 0.001	78.745 ± 1.225	$58224.1673661 \pm 0.1026421$	101.79 ± 5.748	0.207 ± 0.009
HD 158573	643.102 ± 0.057	8022.899 ± 12.595	0.242 ± 0.002	136.205 ± 0.252	$58401.1143219 \pm 0.488384$	395.484 ± 21.884	1.735 ± 0.072
HD 162735	4195.724 ± 31.308	3427.176 ± 3.85	0.65 ± 0.002	1.746 ± 0.173	$58373.2349741 \pm 0.6875655$	227.289 ± 13.044	5.653 ± 0.246
HD 211961	789.659 ± 1.321	3377.341 ± 68.342	0.367 ± 0.009	7.568 ± 1.519	$57877.1189585 \pm 5.0398762$	138.966 ± 8.612	1.721 ± 0.079
HD 238135	1805.254 ± 0.67	5782.54 ± 191.856	0.403 ± 0.016	-89.859 ± 1.48	$57345.9845014 \pm 7.0351439$	279.236 ± 18.065	2.989 ± 0.135
HD 25603	1868.924 ± 15.37	4579.82 ± 13.569	0.217 ± 0.004	-129.817 ± 0.566	$58518.5871339 \pm 2.0852495$	272.815 ± 15.713	3.216 ± 0.141
HD 26596	889.826 ± 0.264	2808.549 ± 6.246	0.441 ± 0.002	-113.04 ± 0.355	$57332.1542194 \pm 1.2263345$	120.987 ± 6.918	1.889 ± 0.082
HD 30311	2424.173 ± 24.444	3261.211 ± 79.795	0.383 ± 0.01	-54.843 ± 2.332	$58828.8450989 \pm 11.4762372$	215.416 ± 13.812	3.884 ± 0.169
HD 352975	302.687 ± 0.049	7235.338 ± 30.09	0.253 ± 0.002	-156.682 ± 0.433	$58222.2175044 \pm 0.5117854$	208.058 ± 12.402	0.897 ± 0.041
HD 76332	2491.268 ± 22.83	3351.192 ± 121.826	0.135 ± 0.044	61.838 ± 10.079	$57466.8018509 \pm 368.3112031$	218.438 ± 14.354	3.81 ± 0.169
HD 8291	1847.518 ± 7.651	2204.029 ± 12.792	0.632 ± 0.002	-61.81 ± 0.428	$58795.5812933 \pm 0.7539695$	98.748 ± 5.782	2.977 ± 0.131
HD 98451	1179.599 ± 0.231	2607.72 ± 5.295	0.189 ± 0.003	-94.404 ± 0.843	$58445.0929324 \pm 2.1407829$	122.026 ± 7.124	2.18 ± 0.097

4.4 False Positive Indicator Analysis

The shape of spectral lines is affected by stellar activity (Queloz et al., 2001) or face-on binaries (e.g., Díaz et al., 2012; Wright et al., 2013) which can produce apparent RV signatures down to a few ms^{-1} . Following Santos et al. (2000), the expected activity-related RV scatter σ_a is estimated using our mean measurements of the $\log R'_{\text{HK}}$ index. The value of σ_a for the host of giant planets and brown dwarfs is given in Table 4.5.

The most active target in the sample that shows high activity is HD 187057 with $\log R'_{\text{HK}} = -4.26$. The value of σ_a for HD 187057 is found to be 20.2 ms^{-1} , which is small compared to the observed dispersion of the measured RVs. The second most active target is HD 204277 with $\log R'_{\text{HK}} = -4.50$ that corresponds to $\sigma_a \approx 21.8 \text{ ms}^{-1}$. The value of σ_a is the same amplitude as the observed dispersion of the measured RVs. Further analysis to confirm the nature of the signal is presented below. For the remaining stars, σ_a ranges between 5 and 10 ms^{-1} , which is smaller than the observed dispersion of the measured RVs. The variations of the measured RVs are larger than σ_a except for HD 204277. Thus, it is concluded that they are unlikely to be caused by stellar activity.

Table 4.5 – Pearson Correlation Analysis for BIS and FWHM along with the expected dispersion (σ_a) in RV due to stellar activity.

Target	σ_a (ms^{-1})	BIS (p-value)	FWHM (p-value)
BD +450564	7.85	0.034 (0.901)	0.483 (0.058)
BD +550362	7.55	0.103 (0.615)	0.473 (0.015)
BD +631405	7.97	0.382 (0.088)	0.228 (0.321)
BD -004475	7.05	0.054 (0.841)	0.013 (0.961)
HD 124330	5.61	-0.006 (0.964)	-0.019 (0.887)
HD 155193	9.36	0.261 (0.021)	0.029 (0.799)
HD 166356	7.41	-0.346 (0.125)	0.154 (0.504)
HD 184601	7.23	0.285 (0.284)	0.313 (0.238)
HD 187057	20.17	-0.146 (0.669)	-0.205 (0.544)
HD 204277	21.82	0.094 (0.363)	0.358 (0.0)
HD 331093	7.57	0.084 (0.719)	0.425 (0.055)
HD 205521	6.79	0.238 (0.326)	0.257 (0.288)
HD 5433	7.05	-0.283 (0.227)	0.372 (0.106)

To investigate further if the RV signal is caused by stellar activity, any possible correlations between RVs and two derived parameters, namely FWHM (Full Width at Half Maximum), and BIS (Bisector Inverse Span) are studied. I calculated the Pearson correlation coefficients and the significance of the correlation by computing the p-value and did not find any significant correlation. The values of Pearson correlation coefficients and their p-values are presented in Table 4.5.

HD 204277 b - Not a planet

HD 204277 is an active star which has the highest $\sigma_a = 21.8 \text{ ms}^{-1}$ among all the targets presented in Table 4.5. No correlation between observed RVs and BIS for HD 204277 (Pearson correlation coefficient = 0.09, $p=0.36$) and between RVs and FWHM for HD 204277 (0.36, 0.0) is found. However, the periodograms of BIS and FWHM show a peak at the period at which the planet is detected in RVs. Figure 4.6 shows the periodogram for the RVs, BIS and FWHM. So it is concluded that the observed RV variations are likely due to the stellar activity and unlikely due to a planet.

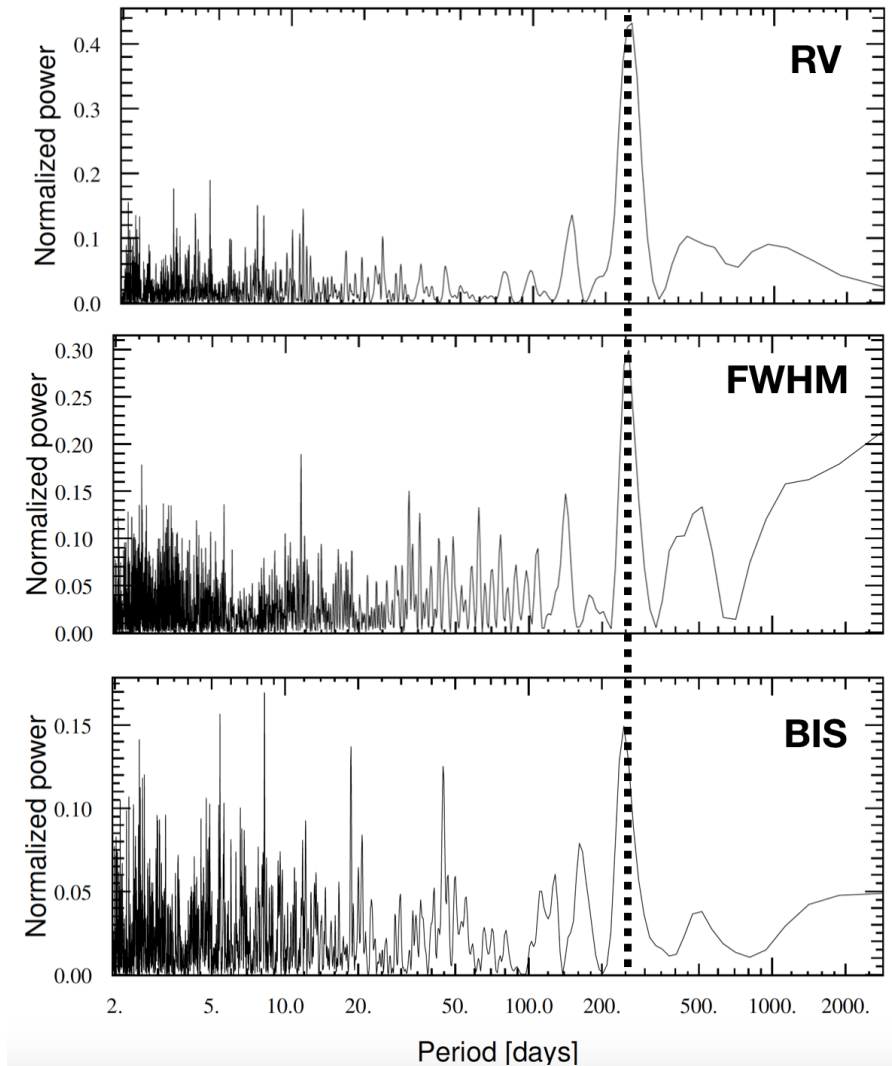


Figure 4.6 – Lomb-Scargle periodogram for HD 204277 for the observed radial velocities, BIS and FWHM.

4.5 Summary and Conclusion

In this chapter, we report the discovery of 6 new giant planets, six brown dwarf candidates, and 15 stellar companions with the SOPHIE spectrograph at OHP.

The newly detected giant planets have periods in the range of 260–1196 days and minimum masses between 0.70 – 3.95 M_J . They show a wide range in eccentricities from nearly circular orbit for BD +450564 b with $e=0.09$ to highly eccentric orbit around BD +631405 with $e=0.881$. Additional drifts are also found in the radial velocity of two targets pointing towards the possibility of an additional companion at a long period in the planetary system. More observations of these targets will be able to reveal such companions. All the detected giant planets candidates can be classified as Cool Jupiters. Most of the stars that host giant planets in this paper have significant metallicity excess (with $[Fe/H] > 0.0$ dex), as shown in Fig 4.7. This small sample seems to agree with previous observations that giant planets occur significantly around stars that are more metal-rich (Rickman et al., 2019; Santos et al., 2004).

The minimum masses of the six brown dwarf companions fall within between 26 and 91 M_J . They have an orbital period between 48 to 2031 days. All the detected brown dwarf companions have significant eccentricity except for the heaviest brown dwarf companion around HD 187057. The period–eccentricity distribution of brown dwarfs is shown in figure 4.8 with (minimum) masses

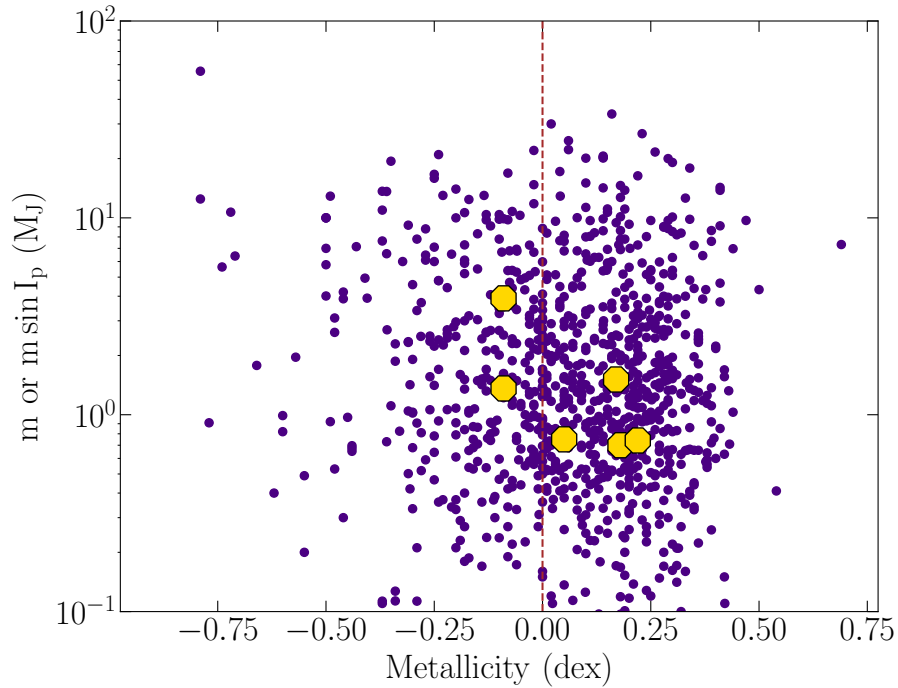


Figure 4.7 – Planetary mass (minimum mass) as a function of the host star metallicity. The new giant planets that presented in this chapter are shown by the yellow octagons and the known exoplanets are marked in purple solid circles. The brown dashed line shows the metallicity of the Sun. All of the stars with detected companions in this paper have a significant metallicity excess. (Credits: NASA’s Exoplanet Archive for the data of known exoplanets)

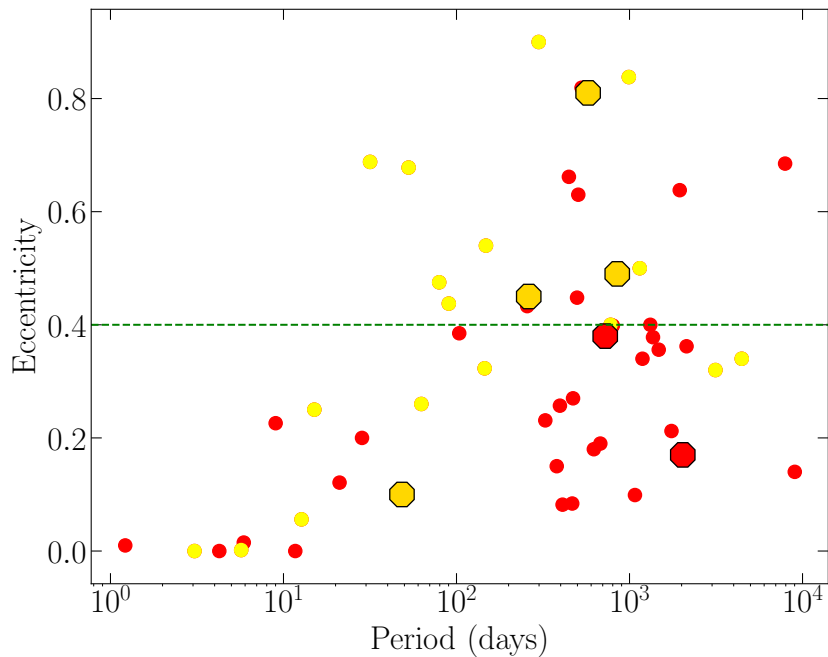


Figure 4.8 – Period - eccentricity distribution of brown dwarfs - The new brown dwarfs presented in this paper are shown in octagons and previous brown dwarfs data taken from Table 1 of [Ma & Ge \(2014\)](#) are plotted in circles. Yellow represents brown dwarfs with m or $m \sin I_p > 42.5 M_J$ and red represents brown dwarfs with m or $m \sin I_p < 42.5 M_J$.

greater than 42.5 M_J in yellow and (minimum) masses less than 42.5 M_J in red. These new detections are consistent with the observations of [Ma & Ge \(2014\)](#) who reported that there are a significant number of brown dwarfs with (minimum) masses less than 42.5 M_J that have an orbital period in between 300 and 3000 d and have eccentricities less than 0.4.

The Keplerian solution for stellar companions more massive than $0.09 M_{\odot}$ is also presented. These objects are followed with SOPHIE for the brown dwarf detection, which finally turned out to be low mass stars. Astrometry with the Gaia and Hipparcos catalog will also allow us to put constraints on the orbital inclination and the true mass of these objects. The heaviest giant planet/brown dwarf companions in our small sample have higher eccentricities, as reported by [Ma & Ge \(2014\)](#). The increase in the detection of giant planets and brown dwarfs is an important step for building a statistically significant sample, which is crucial for understanding the formation and subsequent evolution of such objects.

An ongoing study will report another six giant planets (Demangeon, Dalal, et al., 2020 (in prep)). These giant planets are also cool Jupiters, similar to those reported in this chapter.

4.6 References

- Alibert Y., Mordasini C., Benz W., Winisdoerffer C., 2005, [A&A](#), **434**, 343 43
- Baranne A., et al., 1996, [A&AS](#), **119**, 373 44
- Borgniet S., Lagrange A. M., Meunier N., Galland F., 2017, [A&A](#), **599**, A57 43
- Boss A. P., 2011, [ApJ](#), **731**, 74 40
- Bouchy F., et al., 2009, [A&A](#), **505**, 853 40, 44
- Bouchy F., Díaz R. F., Hébrard G., Arnold L., Boisse I., Delfosse X., Perruchot S., Santerne A., 2013, [A&A](#), **549**, A49 44
- Bouchy F., et al., 2016, [A&A](#), **585**, A46 44
- Cai K., Pickett M. K., Durisen R. H., Milne A. M., 2010, [ApJ](#), **716**, L176 40
- Chabrier G., Baraffe I., 1997, [A&A](#), **327**, 1039 42
- Dawson R. I., Johnson J. A., 2018, [ARA&A](#), **56**, 175 41
- Díaz R. F., et al., 2012, [A&A](#), **538**, A113 44, 53
- Díaz R. F., et al., 2014, [A&A](#), **572**, A109 44
- Fernandes R. B., Mulders G. D., Pascucci I., Mordasini C., Emsenhuber A., 2019, [ApJ](#), **874**, 81 41
- Grether D., Lineweaver C. H., 2004, in Dupree A. K., Benz A. O., eds, IAU Symposium Vol. 219, Stars as Suns : Activity, Evolution and Planets. p. 798 43
- Grether D., Lineweaver C. H., 2006, [ApJ](#), **640**, 1051 43
- Guilera O. M., Brunini A., Benvenuto O. G., 2010, [A&A](#), **521**, A50 40
- Hayashi C., Nakano T., 1963, [Progress of Theoretical Physics](#), **30**, 460 42
- Howard A. W., et al., 2010, [Science](#), **330**, 653 41

- Ida S., Lin D. N. C., 2004, *ApJ*, 616, 567 43
- Kiefer F., et al., 2019, *A&A*, 631, A125 44
- Ma B., Ge J., 2014, *MNRAS*, 439, 2781 43, 55, 56
- Marcy G. W., Butler R. P., 2000, *PASP*, 112, 137 43
- Morales J. C., et al., 2019, *Science*, 365, 1441 40
- Morbidelli A., Tsiganis K., Crida A., Levison H. F., Gomes R., 2007, *AJ*, 134, 1790 42
- Mordasini C., Alibert Y., Benz W., 2009, *A&A*, 501, 1139 40, 43
- Pepe F., et al., 2002, *The Messenger*, 110, 9 44
- Perruchot S., et al., 2008, in *Proc. SPIE*. p. 70140J, doi:10.1117/12.787379 44
- Pollack J. B., Hubickyj O., Bodenheimer P., Lissauer J. J., Podolak M., Greenzweig Y., 1996, , 124, 62 40
- Queloz D., et al., 2001, *A&A*, 379, 279 53
- Raymond S. N., Izidoro A., 2017, , 297, 134 42
- Rickman E. L., et al., 2019, *A&A*, 625, A71 54
- Sahlmann J., et al., 2011a, *A&A*, 525, A95 43
- Sahlmann J., Lovis C., Queloz D., Ségransan D., 2011b, *A&A*, 528, L8 44
- Santerne A., et al., 2016, *A&A*, 587, A64 44
- Santos N. C., Mayor M., Naef D., Pepe F., Queloz D., Udry S., Blecha A., 2000, *A&A*, 361, 265 53
- Santos N. C., Israelian G., Mayor M., 2004, *A&A*, 415, 1153 54
- Santos N. C., et al., 2017, *A&A*, 603, A30 40
- Ségransan D., et al., 2011, *A&A*, 535, A54 44
- Spiegel D. S., Burrows A., Milsom J. A., 2011, *ApJ*, 727, 57 42
- Wilson P. A., et al., 2016, *A&A*, 588, A144 44
- Wittenmyer R. A., et al., 2020, *MNRAS*, 492, 377 41
- Wright J. T., Marcy G. W., Howard A. W., Johnson J. A., Morton T. D., Fischer D. A., 2012, *ApJ*, 753, 160 41
- Wright J. T., et al., 2013, *ApJ*, 770, 119 53

Chapter 5

Obliquity Measurements

*“ Somewhere, something
incredible is waiting to be known.
”*

Carl Sagan

Contents

5.1 Why measure star-planets alignment/misalignment?	60
5.2 Obliquity measurement of a sub-Neptune HD 3167 c	62
5.2.1 Stellar and planetary parameters	63
5.2.2 Spin-Orbit (mis)alignment measurement	64
5.2.3 Results and Conclusion	77
5.2.4 Additional Information - True Obliquity	77
5.3 Revisiting obliquity of HD 189733 with SPIRou	78
5.3.1 Stellar and planetary parameters	78
5.3.2 Keplerian Orbit of HD 189733 in near infrared	78
5.3.3 Observation and Analysis	80
5.3.4 Obliquity measurement using classical RM Fit	81
5.3.5 Obliquity measurement using Doppler Shadow	83
5.3.6 Results and Conclusion	84
5.4 Summary	85
5.5 References	85

In this chapter, I present the new obliquity measurement for the exoplanet HD 3167 c. I also present obliquity measurements for a well-known exoplanet HD 189733A b using the new spectropolarimeter SPIRou. In Section 5.2, I discuss the planetary system HD 3167 and explain the findings of [Dalal et al. \(2019\)](#), where the obliquity measurement of HD 3167 c is reported using HARPSN data. In Section 5.3, I discuss the planetary system HD 189733 and the first results of the SPIRou instrument, which are tested on HD 189733.

5.1 Why measure star-planets alignment/misalignment?

Obliquity is the angle between the stellar rotation axis and the orbital axis of an exoplanet. One can measure the obliquity projected onto the sky through the Rossiter–McLaughlin (RM) effect (see details in Sec 2.4). Other techniques can be used to measure obliquity, such as using starspots ([Dai et al., 2017](#)) and through asteroseismology ([Van Eylen et al., 2014](#)). Obliquity is an important probe to understand the formation and, subsequently, the dynamical history of an exoplanetary system. In the Solar System, the orbits of all the planets are nearly aligned with respect to the Sun’s stellar spin and have obliquities lower than 7° ([Beck & Giles, 2005](#)). The aligned orbits can be explained by the standard paradigm of planet formation from the rotating protoplanetary disk ([Woolfson, 1993](#)). Exoplanets, however, exhibit a wide range of obliquities, including polar orbits ($\lambda \sim 90^\circ$) and retrograde orbits ($\lambda > 90^\circ$). Some of the mechanisms proposed to explain the misaligned orbits of various exoplanets are:

- * **Kozai-Lidov Mechanism** is a process in which an outer companion on an inclined orbit causes periodic changes in the orbital inclination and eccentricity by perturbing the orbit of the inner body (e.g., [Anderson et al., 2016](#); [Fabrycky & Tremaine, 2007](#); [Naoz et al., 2011](#)).
- * **Planet-Planet Scattering** in which planets interact and may migrate from the position of their formation, resulting in misaligned orbits (e.g., [Chatterjee et al., 2008](#); [Nagasawa & Ida, 2011](#)).
- * **Inhomogeneous accretion** assumes that star-formation is a chaotic process, and a highly oblique planet is a by-product. (e.g., [Bate et al., 2010](#); [Fielding et al., 2015](#)).
- * **Early-on interaction between the magnetic field of the star and the protoplanetary disk** can lead to misaligned orbits (e.g., [Lai et al., 2011](#)).
- * **Stellar flybys** can induce retrograde orbits (e.g., [Breslau & Pfalzner, 2019](#)).
- * **Excitation by an outer companion** (e.g., [Anderson & Lai, 2018](#); [Batygin, 2012](#)).

By carefully studying the distribution of obliquities, one can distinguish between different planet formation and evolution models. For example, hot Jupiter obliquities revealed that most of the hot Jupiters have been affected by tidal evolution, i.e., hot Jupiters have experienced more violent and disruptive scenarios during their migration either due to the Kozai-Lidov Mechanism or planet-planet scattering ([Albrecht et al., 2013](#)). Apart from that, other scenarios, such as in-situ formation or disk migration, can also explain misaligned hot Jupiters. [Morton & Johnson \(2011\)](#) found that the planet-planet scattering model is much more likely to explain the trend of projected obliquity for hot Jupiters when compared to the Kozai-Lidov migration model. There are many trends that are the outcomes of studying obliquity distribution. For example, hot Jupiters around stars with effective temperatures above 6000–6300 K are more oblique (e.g., [Albrecht et al., 2012, 2013](#); [Winn et al., 2010a](#)), and that hot Jupiters’ obliquities can be related to the stellar age, i.e., hot Jupiters in non-coplanar orbits are placed early in their history which supports the planet-planet

scattering model (Triaud, 2011). Muñoz & Perets (2018) reported that more tightly packed systems or those with higher total planet masses exhibit more oblique orbits than the overall sample.

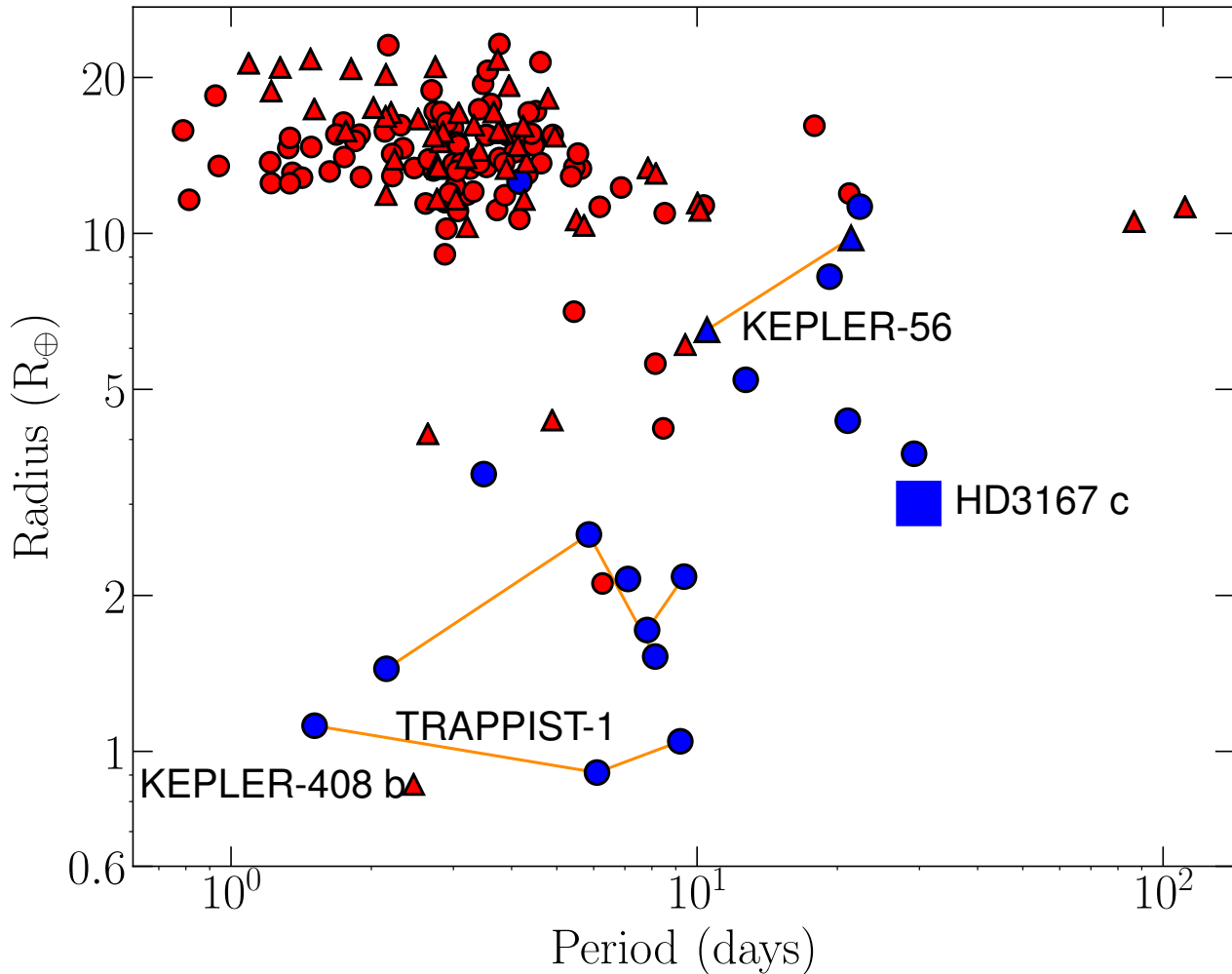


Figure 5.1 – Radius of planets in earth radii (R_{\oplus}) versus orbital periods of the planets for which the obliquity has been measured. Data is taken from TEPcat. The solid circles represent planetary systems that are aligned, and the solid triangle shows the misaligned planetary systems. The blue color corresponds to multi-planet systems, and the red color corresponds to the single planet systems. Measurement for HD 3167 c in the blue square is presented in this thesis.

More obliquity measurements are thus required to identify such trends that can relate the obliquity distribution to different stellar and planetary properties. Figure 5.1 shows the distribution of the period and radius of exoplanets, available on TEPcat for transiting exoplanets, which have obliquity measurements. TEPcat is an online catalog of the physical properties of known transiting extrasolar planets, which also include obliquity measurements¹. Exoplanets with $|\lambda| > 30^\circ$ are considered as misaligned systems. There are 144 single exoplanet systems and 13 multi-planet systems for which TEPcat has either sky-projected obliquity and/or true obliquity measurements (see 2.4.2 for the definition of true obliquity).

Many systems have well-aligned orbits such as HD 189733 (Cegla et al., 2016; Collier Cameron et al., 2010; Triaud et al., 2009; Winn et al., 2006) and WASP-18 (Albrecht et al., 2012; Triaud et al., 2010). Numerous systems with misaligned orbits such as X0-3 (Hébrard et al., 2008), WASP-1

¹<https://www.astro.keele.ac.uk/jkt/tepcat/tepcat.html>

(Simpson et al., 2011) and retrograde orbits such as HAT-P-6 (Albrecht et al., 2012; Hébrard et al., 2011) and WASP-8 (Bourrier et al., 2017; Queloz et al., 2010) exist. It is clear from Figure 5.1 that the majority of the obliquity measurements are available for planets with larger radii such as hot Jupiters. While the obliquity measurements are extended to smaller exoplanets such as HAT-P-11 b (Winn et al., 2010b), GJ436 b (Bourrier et al., 2018), Kepler-408 b (Kamiaka et al., 2019) and DS Tuc Ab (Zhou et al., 2020), little is known for multi-planet systems. Kepler-408 b is by far the smallest planet with a misaligned orbit. There are only a few obliquity measurements available for a few multi-planet systems. Most multi-planet systems are well aligned such as Kepler 30 (Sanchis-Ojeda et al., 2012), Kepler 25 (Albrecht et al., 2013), Kepler 89 (Hirano et al., 2012) and TRAPPIST-1 (Hirano et al., 2020). Two multi-planetary systems that have misaligned orbits with respect to its host star are Kepler 56 (Huber et al., 2013) and HD 3167 (Dalal et al., 2019). The misalignment in the Kepler 56 system was, however, explained by the presence of a massive companion in a wide orbit. Recently Hirano et al. (2020) reported that the TRAPPIST-1 system is not strongly misaligned, although more observations are required to confirm their results. The obliquity measurements of planets e, f, and b are plotted and are labeled as TRAPPIST-1 (see Fig. 5.1). HD 3167 c (marked in the plot) is a sub-Neptune for which the obliquity measurement reported in Dalal et al. (2019) is presented here. The unexplored multiple transiting planets are particularly interesting as they provide the opportunity to probe the 'primordial' (i.e., the result of planet formation) obliquities of exoplanetary systems.

Therefore, it is extremely useful to measure obliquity as it provides constraints on planet formation, migration, and evolution along with the architecture of planetary systems.

5.2 Obliquity measurement of a sub-Neptune HD 3167 c

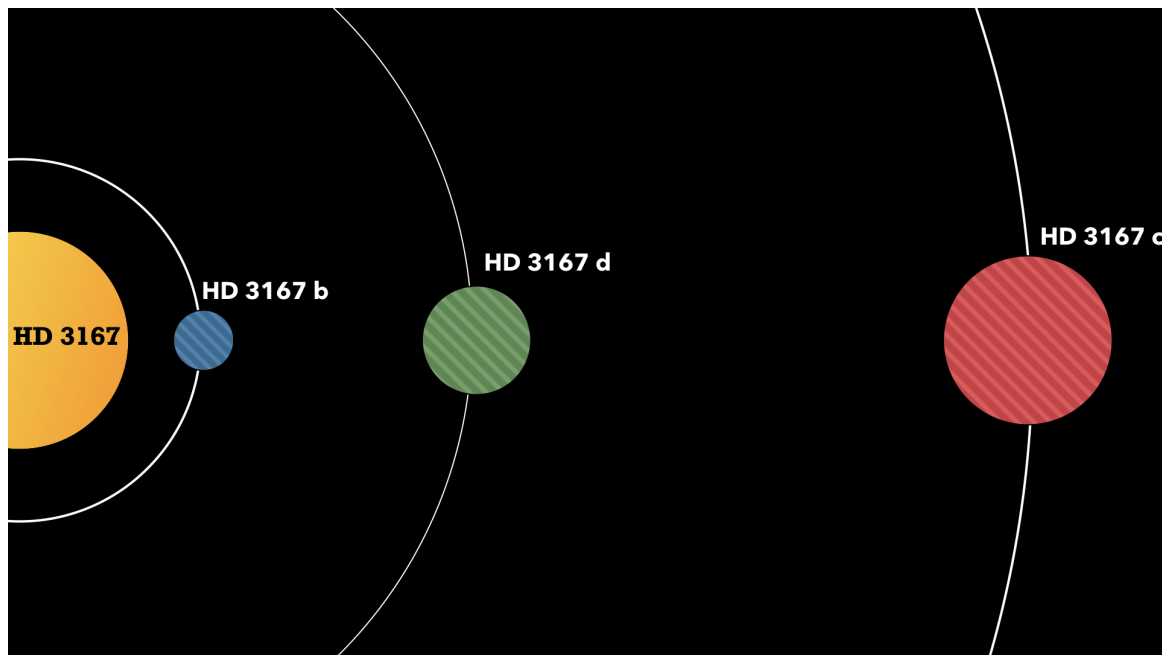


Figure 5.2 – An illustration of the planetary system HD 3167 (Not to scale)

HD 3167 is a bright ($V=8.94$) nearby K0 star that hosts two transiting and one non-transiting planet. Figure 5.2 shows a sketch of the planetary system HD 3167. Vanderburg et al. (2016) first reported the presence of two transiting planets using the data from NASA's K2 mission. Figure 5.3

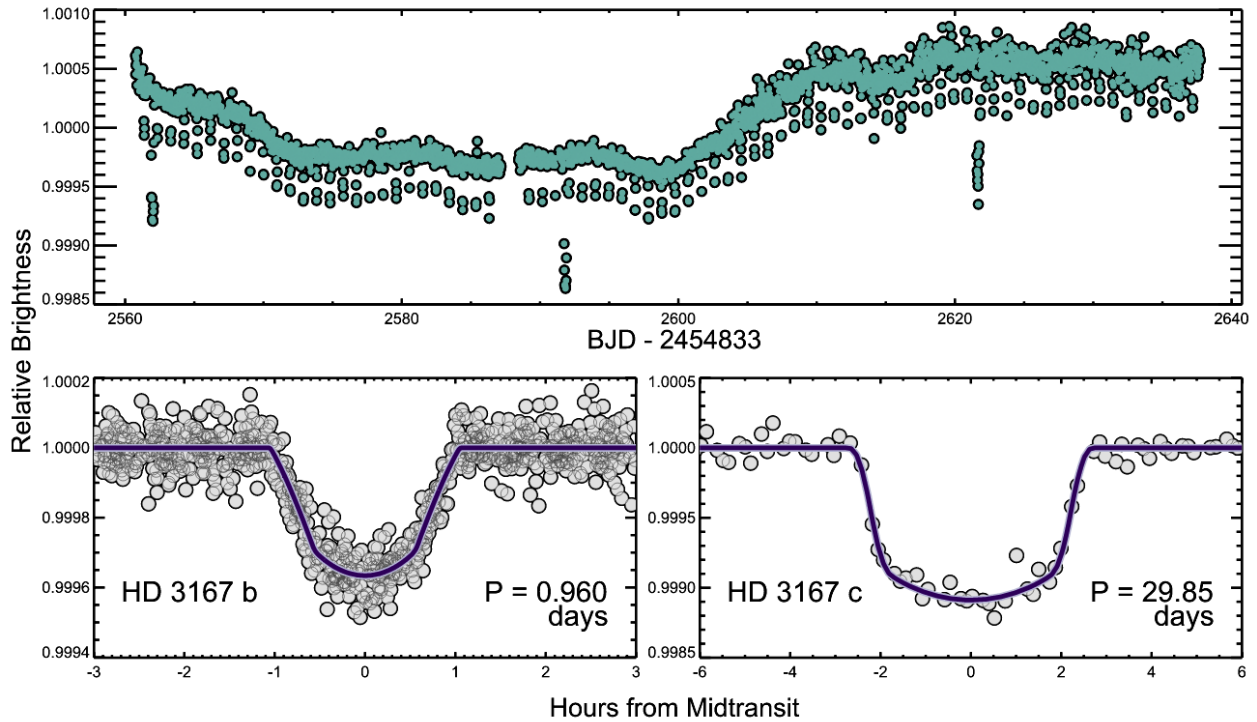


Figure 5.3 – K2 transit light curve: The top panel shows the full K2 light curve and the bottom panel shows the phase folded K2 photometry for planets b (left) and c (right) along with the best-fit model as a solid purple line. Figure credits: (Vanderburg et al., 2016)

shows the full K2 transit curve² which was analyzed to detect the two transiting planets of HD 3167.

Later Gandolfi et al. (2017) and Christiansen et al. (2017) both simultaneously performed a radial velocity analysis from independent observations. Gandolfi et al. (2017) found two additional periodic signals in the radial velocity data at 6.0 days and 10.7 days. The nature of these two signals was, however, not confirmed by the authors. Christiansen et al. (2017) was successful in detecting the third non-transiting planet. Figure 5.4 shows the best-fit three-planet Keplerian model along with the radial velocity data for HD 3167.

5.2.1 Stellar and planetary parameters

HD 3167 is a K-type main-sequence star that is too faint to be seen with the naked eye. The star is chromospherically inactive with a $\log R_{\text{HK}}$ of -5.04. It has a projected rotational velocity of about 1.7 km s^{-1} , and a metallicity (Fe/H) of 0.04 dex. The star has a mass of $0.872 M_{\odot}$ and a radius of $0.866 R_{\odot}$.

HD 3167 b is one of the transiting planets and has an orbital period of 0.96 days. It is a hot super-Earth of mass $5.02 \pm 0.38 M_{\oplus}$ and radius $1.70^{+0.18}_{-0.15} R_{\oplus}$ which correspond to a density of $5.60^{+2.15}_{-1.43} \text{ g cm}^{-3}$. HD 3167 b has a predominantly rocky composition with the potential of having a thin envelope of H/He or other low-density volatiles. HD 3167 c is the second transiting planet and has an orbital period of 29.84 days. It is a sub-Neptune (or mini-Neptune) of mass $9.80^{+1.30}_{-1.24} M_{\oplus}$ and radius $3.01^{+0.42}_{-0.28} R_{\oplus}$. It has a low bulk density of $1.97^{+0.95}_{-0.59} \text{ g cm}^{-3}$ with a gaseous envelope consisting mainly of hydrogen and helium, or it is a planet consisting of mostly water. HD 3167 d is the third non-transiting planet and orbits the star in 8.51 days. Its minimum mass is $6.70 \pm 0.71 M_{\oplus}$. Since

²The drop in the flux in the first half of the observation, as seen in the light curve of HD 3167 is likely an instrumental artifact caused by the spacecraft pointing jitter.

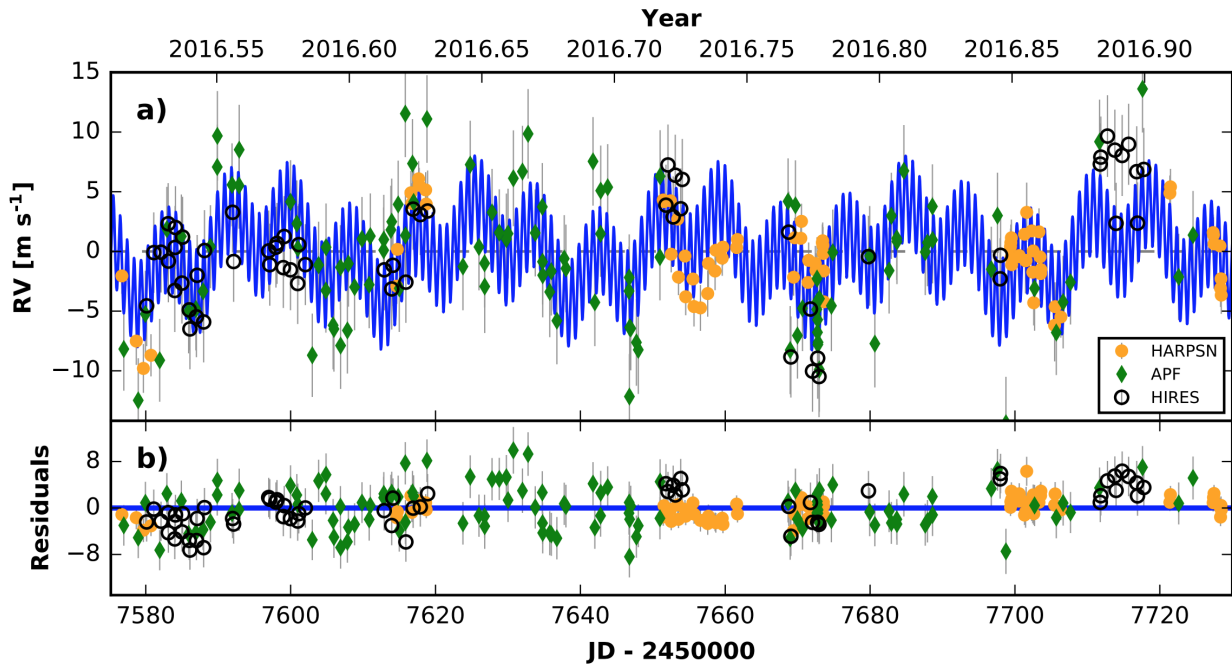


Figure 5.4 – Radial velocity data from HARPSN (in yellow circles), APF (in green diamonds) and, HIRES (in open black circles) for HD 3167 along with the best-fit Keplerian orbital model as a solid blue line. The residuals after the best-fit three-planet model are also shown in the bottom. Figure credits: (Christiansen et al., 2017)

it is a non-transiting planet, its radius and density cannot be computed from the current data.

5.2.2 Spin-Orbit (mis)alignment measurement

As discussed in Section 5.1, there are only a few obliquity measurements available for small planets and even less for multi-planet systems. This work aims to measure the obliquity for the sub-Neptune HD 3167 c, which is part of a multi-planet system. This measurement will help to populate the previously unexplored regions of the obliquity distribution of small size planets. In addition to that, the gradual increase in the number of obliquity measurements for small (multiple) exoplanets will help to build statistical studies which will eventually help in distinguishing between different theoretical scenarios of planet formation and evolution. Planets with larger radii give a larger amplitude of the RM effect (see Eq. 2.19). The expected amplitude of the RM anomaly for HD 3167 b and HD 3167 c is 0.56 ms^{-1} , and 1.7 ms^{-1} respectively. HD 3167 c is, therefore, the most favorable planet for the obliquity measurement. Apart from that, the longer transit duration of HD 3167 c allows three times better data sampling during a given transit. This work was first published in Dalal et al. (2019), with a detailed analysis of the dynamics of the system. All this work is presented hereafter. The work associated with the obliquity measurement using reloaded RM, the constraint on the obliquity of b, and d from geometry and the dynamics was done in collaboration with the co-authors of the paper.

Nearly polar orbit of the sub-Neptune HD 3167 c

Constraints on the dynamical history of a multi-planet system

S. Dalal¹, G. Hébrard^{1,2}, A. Lecavelier des Étangs¹, A. C. Petit³, V. Bourrier⁴, J. Laskar³,
P.-C. König¹, and A. C. M. Correia^{5,3}

¹ Institut d'astrophysique de Paris (IAP), UMR 7095 CNRS, Université Pierre & Marie Curie, 98bis Boulevard Arago, 75014 Paris, France

e-mail: shweta.dalal@iap.fr

² Observatoire de Haute-Provence (OHP), CNRS, Université d'Aix-Marseille, 04870 Saint-Michel-l'Observatoire, France

³ IMCCE, CNRS-UMR 8028, Observatoire de Paris, PSL University, Sorbonne Université, 77 avenue Denfert-Rochereau, 75014 Paris, France

⁴ Observatoire de l'Université de Geneve, 51 chemin des Maillettes, Versoix, Switzerland

⁵ CFisUC, Department of Physics, University of Coimbra, 3004-516 Coimbra, Portugal

Received 24 May 2019 / Accepted 26 June 2019

ABSTRACT

Aims. We present the obliquity measurement, that is, the angle between the normal angle of the orbital plane and the stellar spin axis, of the sub-Neptune planet HD 3167 c, which transits a bright nearby K0 star. We study the orbital architecture of this multi-planet system to understand its dynamical history. We also place constraints on the obliquity of planet d based on the geometry of the planetary system and the dynamical study of the system.

Methods. New observations obtained with HARPS-N at the Telescopio Nazionale *Galileo* (TNG) were employed for our analysis. The sky-projected obliquity was measured using three different methods: the Rossiter-McLaughlin anomaly, Doppler tomography, and reloaded Rossiter-McLaughlin techniques. We performed the stability analysis of the system and investigated the dynamical interactions between the planets and the star.

Results. HD 3167 c is found to be nearly polar with sky-projected obliquity, $\lambda = -97^\circ \pm 23^\circ$. This misalignment of the orbit of planet c with the spin axis of the host star is detected with 97% confidence. The analysis of the dynamics of this system yields coplanar orbits of planets c and d. It also shows that it is unlikely that the currently observed system can generate this high obliquity for planets c and d by itself. However, the polar orbits of planets c and d could be explained by the presence of an outer companion in the system. Follow-up observations of the system are required to confirm such a long-period companion.

Key words. techniques: radial velocities – planets and satellites: fundamental parameters – planet–star interactions – planets and satellites: individual: HD 3167

1. Introduction

Obliquity is defined as the angle between the normal angle of a planetary orbit and the rotation axis of the planet host star. It is an important probe for understanding the dynamical history of exoplanetary systems. Solar system planets are nearly aligned and have obliquities lower than 7° , which might be a consequence of their formation from the protoplanetary disk. However, this is not the case for all exoplanetary systems. Various misaligned systems, that is, $\lambda \gtrsim 30^\circ$, including some retrograde ($\lambda \sim 180^\circ$, e.g., Hébrard et al. 2008) or nearly polar ($\lambda \sim 90^\circ$, e.g., Triaud et al. 2010) orbits have been discovered. These misaligned orbits may result from Kozai migration and/or tidal friction (Nagasawa et al. 2008; Fabrycky & Tremaine 2007; Guillochon et al. 2011; Correia et al. 2011), where the close-in planets migrate as a result of scattering or of early-on interaction between the magnetic star and its disk (Lai et al. 2011), or the migration might be caused later by elliptical tidal instability (Cébron et al. 2011). Another possibility is that the star has been misaligned since the days when the protoplanetary disk was present as a result of inhomogeneous accretion (Bate et al. 2010) or a stellar flyby (Batygin 2012).

Most of the obliquity measurements are available for single hot Jupiters. Some of the smallest planets detected with a Rossiter measurement are GJ 436 b ($4.2 \pm 0.2 R_\oplus$) and HAT-P-11 b ($4.4 \pm 0.1 R_\oplus$), which are nearly polar (Bourrier et al. 2018; Winn et al. 2010), and 55 Cnc e ($1.94 \pm 0.04 R_\oplus$), which is also misaligned (Bourrier & Hébrard 2014), although the latest result has been questioned (López-Morales et al. 2014). Kepler 408 b is the smallest planet with a misaligned orbit among all planets that are known to have an obliquity measurement (Kamiaka et al. 2019). A few obliquity detections have been reported for multi-planet systems such as KOI-94 and Kepler 30 (Hirano et al. 2012; Albrecht et al. 2013; Sanchis-Ojeda et al. 2012), whose planets have coplanar orbits that are aligned with the stellar rotation.

We study the multi-planet system hosted by HD 3167. This system includes two transiting planets and one non-transiting planet. Vanderburg et al. (2016) first reported the presence of two small short-period transiting planets from photometry. The third planet HD 3167 d was later discovered in the radial velocity (RV) analysis by Christiansen et al. (2017). Gandolfi et al. (2017) found evidence of two additional signals in the RV measurements of HD 3167 with periods of 6.0 and 10.7 days. However, they were unable to confirm the nature of these two signals. Furthermore,

Christiansen et al. (2017) did not find any signal at 6 or 10.7 days. The masses of the transiting planets were found to be $5.02 \pm 0.38 M_{\oplus}$ for HD 3167 b, a hot super-Earth, and $9.80^{+1.30}_{-1.24} M_{\oplus}$ for HD 3167 c, a warm sub-Neptune. The non-transiting planet HD 3167 d with a mass of at least $6.90 \pm 0.71 M_{\oplus}$ orbits the star in 8.51 days. The two transiting planets have orbital periods of 0.96 days and 29.84 days and radii of $1.70 R_{\oplus}$ and $3.01 R_{\oplus}$, respectively. We measure the sky-projected obliquity for HD 3167 c, whose larger radius makes it the most favorable planet for the obliquity measurements. Because the period of planet c is longer than that of planet b, the data sampling during a given transit is three times better.

It is difficult to measure the true 3D obliquity, and most methods only access the projection of the obliquity. The sky-projected obliquity for a transiting exoplanet can be measured by monitoring the stellar spectrum during planetary transits. During a transit, the partial occultation of the rotating stellar disk causes asymmetric line profiles that can be detected using different methods such as the Rossiter-McLaughlin (RM) anomaly, Doppler tomography, and the reloaded RM method. These methods use different approaches to retrieve the path of the planet across the stellar disk. This allows us to quantify the systematic errors related to the data analysis method. The RM anomaly takes into account that asymmetry in line profiles induces an anomaly in the RV of the star (Queloz et al. 2000; Hébrard et al. 2008). However, changes in the cross-correlation function (CCF) morphology are not analyzed. Doppler tomography uses the spectral information present in the CCF of the star rather than just their RV centroids. This method entails tracking the full time-series of spectral CCF by modeling the additional absorption line profiles that are superimposed on the stellar spectrum during the planet transit (e.g., Collier Cameron et al. 2010; Bourrier et al. 2015; Crouzet et al. 2017). This model is then subtracted from the CCFs, and the spectral signature of the light blocked by the planet remains. Finally, the reloaded RM technique directly analyzes the local CCF that is occulted by the planet to measure the sky-projected obliquity (e.g., Cegla et al. 2016a; Bourrier et al. 2017). It isolates the CCFs outside and during the transit with no assumptions about the shape of the stellar line profiles.

The amplitude of the RM anomaly is expected to be below 2 m s^{-1} for HD 3167 c. Detecting such a low-amplitude effect is challenging, therefore we decided to determine the robustness and significance of our results using the three different methods described above. The different methods have their respective advantages and limitations. A combined analysis involving the three complementary approaches therefore provides an obliquity measurement that is more robust against systematic effects that are due to the analysis method.

We measure the sky-projected obliquity of HD 3167 c using the three methods and finally discuss the dynamics of the system. This paper is structured as follows. We describe the spectroscopic observations during the transit in Sect. 2. The detection of spectroscopic transit followed by the data analysis using the RM anomaly, Doppler tomography, and the reloaded RM is presented in Sect. 3. We discuss the obliquity of planets b and d from geometry in Sect. 4. We study the dynamics of the system in Sect. 5 and explore the possible outer companion in Sect. 6. Finally, we conclude in Sect. 7.

2. Observations

We obtained the spectra of HD 3167 during the two transits of planet c on 2016 October 1 and 2017 November 23 with the

spectrograph HARPS-N with a total of 35 observations and 24 observations, respectively. HARPS-N, which is located at the 3.58 m Telescopio Nazionale *Galileo* (TNG, La Palma, Spain), is an echelle spectrograph that allows high-precision RV measurements. Observations were taken with resolving power $R = 115\,000$ with 15 min of exposure time. We used the spectrograph with one fiber on the star and the second fiber on a thorium-argon lamp so that the observation had high RV precision. The signal-to-noise ratio (S/N) per pixel at 527 nm for the spectra taken during the 2016 transit was 56–117 with an average $S/N = 87$. The 2017 transit was observed in poor weather conditions with S/N values ranging from 34 to 107 with an average $S/N = 72$. We primarily worked with the 2016 transit data for the reasons explained in Sect. 3.2.3.

The Data Reduction Software (DRS version 3.7) pipeline was used to extract the HARPS-N spectra and to cross-correlate them with numerical masks following the method described in Baranne et al. (1996) and Pepe et al. (2002). The CCFs obtained were fit by Gaussians to derive the RVs and their uncertainties. We tested different numerical masks such as G2, K0, and K5 and also determined the effect of removing some low S/N spectral orders to obtain the CCFs. These tests were performed to improve the data dispersion after the Keplerian fit. The method of fitting a Keplerian is discussed in detail in Sect. 3.1. Final RVs were obtained from CCFs that we produced using the K5 mask and removing the first 15 blue spectral orders with low S/N.

The resulting RVs with their uncertainties are listed in Table 1 for the 2016 observations and in Table B.1 for the 2017 observations. The typical uncertainties were between 0.6 and 1.5 m s^{-1} with a mean value of 0.9 m s^{-1} for the 2016 data. The stellar and planet parameters for HD 3167 that we used were taken from Tables 1 and 5 of Christiansen et al. (2017), except for the value of limb-darkening coefficient (ϵ), which was taken from Gandolfi et al. (2017).

3. Analysis

3.1. Detection of a spectroscopic transit

Figure 1 displays the RV measurements of HD 3167 during the 2016 transit of planet c. The upper panel shows RVs along with the best-fit RM model found from χ^2 minimization (discussed in Sect. 3.2), and the lower panel shows residual RVs after the fit. The red dashed line is the Keplerian model for the orbital motion of the three planets. During the transit, the deviation between the Keplerian model and the observed RVs is caused by the RM anomaly.

To separate the observation taken during the planet transit, only RVs between the beginning of the ingress (T_1) and end of the egress (T_4) were considered. The photometric values of mid-transit (T_0), period (P), and transit duration (T_{14}) of HD 3167 c along with their uncertainties were taken from Christiansen et al. (2017). The total uncertainty of ~ 16 min on T_0 , inferred from the respective uncertainties of 15, 6, and 2 min on P , T_1/T_4 , and T_0 from Christiansen et al. (2017), was taken into account in determining the RVs outside the transit. Thirteen RVs (8 before and 5 after the transit) lay outside the transit, while 18 RVs were present inside the transit. Because of the uncertainty in the observed T_0 , it was not clear whether the remaining 4 RVs were present inside or outside the transit. In the following analysis, T_0 is fixed to the photometric value as the uncertainty on T_0 is negligible in our analysis, as shown in Sect. 3.2.2.

The 13 RVs outside the transit were not sufficient for an independent Keplerian model for the three planets. We therefore took the orbital parameters for the three planets to fit the Keplerian

Table 1. Radial velocities of HD 3167 measured on 2016 October 1 with HARPS-N.

BJD	RV (m s ⁻¹)	Uncertainty (m s ⁻¹)
57 663.38879	19 526.11	0.99
57 663.39881	19 525.6	0.89
57 663.4097	19 524.96	0.96
57 663.42026	19 525.43	0.86
57 663.43128	19 525.48	0.80
57 663.44191	19 527.08	0.89
57 663.45255	19 525.54	0.80
57 663.463	19 525.72	0.78
57 663.47382	19 526.8	0.69
57 663.48469	19 525.99	0.61
57 663.49535	19 528.41	0.65
57 663.5057	19 527.32	0.66
57 663.51666	19 528.51	0.69
57 663.52705	19 529.29	0.76
57 663.53812	19 528.75	0.71
57 663.54859	19 530.09	0.66
57 663.5594	19 529.57	0.71
57 663.56994	19 530.79	0.73
57 663.58084	19 529.89	0.74
57 663.59121	19 529.66	0.75
57 663.60227	19 531.37	0.78
57 663.61288	19 530.97	0.79
57 663.62363	19 529.69	0.83
57 663.63458	19 530.74	0.79
57 663.64483	19 533.16	0.83
57 663.65581	19 531.99	0.85
57 663.66643	19 530.85	0.77
57 663.67668	19 532.44	0.90
57 663.68756	19 532.86	1.01
57 663.69801	19 532.29	1.30
57 663.70995	19 530.61	1.23
57 663.7196	19 531.13	1.17
57 663.73065	19 532.3	1.16
57 663.74124	19 532.95	1.32
57 663.75162	19 532.51	1.49

from Table 5 of [Christiansen et al. \(2017\)](#) in Eq. (1) as

$$RV = \gamma + \sum_{i=1}^3 K_i [\cos(f_i + \omega_i) + e_i \cos \omega_i]. \quad (1)$$

Here K_i represents the RV semi-amplitude, the true anomaly and eccentricity are denoted by f_i and e_i , respectively, and ω_i is the argument of periastron. Finally, a Keplerian model was fit by minimizing the χ^2 considering only one free parameter, that is, the systemic velocity γ . The average of the residual RVs that were taken outside the transit was found to be 0.11 ± 0.72 m s⁻¹, in agreement with the expected uncertainties.

After the Keplerian fit, we noted that the average of residual RVs inside the transit was 1.17 ± 0.76 m s⁻¹, showing an indication of an RM anomaly detection. We fit this using the RM model in Sect. 3.2.2. According to [Gaudi & Winn \(2007\)](#), the expected amplitude of the RM anomaly is 1.7 m s⁻¹, which is within the order of magnitude of the deviation from the Keplerian model observed during the transit.

Furthermore, the slope that is visible in RVs within the observation time (8.7 h) was due to the short periodicity of HD 3167 b

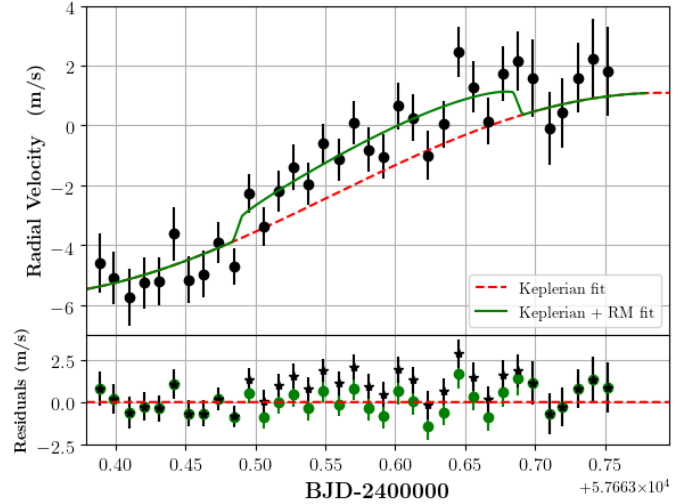


Fig. 1. RV measurements of HD 3167 taken on 2016 October 1 as function of time. *Upper panel:* solid black circles represent the HARPS-N data, the dashed red line indicates the Keplerian fit, and the solid green line depicts the final best fit with the RM effect. *Lower panel:* black solid circles are the residuals after subtracting the Keplerian, and green solid circles are the residuals after subtracting the best-fit RM model.

($P_b = 0.96$ day). To compute the mass of HD 3167 b, a Keplerian in the RVs outside the transit was fit in which K_b was kept as a free parameter. K_b was found to be 3.86 ± 0.35 m s⁻¹, corresponding to a planet mass of HD 3167 b of $M_b = 5.45 \pm 0.50 M_\oplus$. This is consistent with the measurements of [Christiansen et al. \(2017\)](#) ($K_b = 3.58 \pm 0.26$ m s⁻¹, $M_b = 5.02 \pm 0.38 M_\oplus$). K_b was fixed to the more accurate measurement of [Christiansen et al. \(2017\)](#) in the further analysis.

We note that the sky-projected obliquity λ was defined as the angle counted positive from the stellar spin axis toward the orbital plane normal, both projected in the plane of the sky. The sky-projected obliquity was fit using three different methods, as described in the following sections.

3.2. Rossiter-McLaughlin anomaly

The model to fit the RM anomaly is presented in the following section. We applied this model to fit both datasets to measure the sky-projected obliquity.

3.2.1. Model

The method developed by [Ohta et al. \(2005\)](#) was implemented to model the shape of the RM anomaly. These authors derived approximate analytic formulae for the anomaly in RV curves, considering the effect of stellar limb darkening. Following their approach, we adopted a model with five free parameters: γ , λ , the sky-projected stellar rotational velocity $v \sin i_\star$, the orbital inclination i_p , and the ratio of orbital semi-major axis to stellar radius a/R_\star . The values of the radius ratio r_p/R_\star , P , T_0 for HD 3167 c were fixed to their photometric values ([Christiansen et al. 2017](#)), and ε for HD 3167 was fixed to 0.54 ([Gandolfi et al. 2017](#)). The parameters i_p and a/R_\star were kept free because their values were poorly constrained from the photometry. Gaussian priors were applied to i_p and a/R_\star as obtained from photometry ([Christiansen et al. 2017](#)). We adopted a value of $v \sin i_\star$ as a Gaussian prior based on the spectroscopy analysis in [Christiansen et al. \(2017\)](#) ($v \sin i_\star = 1.7 \pm 1.1$ km s⁻¹). We performed a grid search for the free parameters and computed χ^2

at each grid point. The contribution from the uncertainties of i_p , a/R_* , and $v \sin i_*$ was also added quadratically to χ^2 .

3.2.2. 2016 dataset

The data taken on 2016 October 1 are the best dataset for the obliquity measurement in terms of data quality and transit sampling. The 2016 data were fit with the Ohta model, and the reduced χ^2 with 30 degrees of freedom (n) for the best-fit model (RM fit) was found to be 0.95. With the RM fit, the averages of residuals inside and outside the transit were 0.01 ± 0.75 and $0.11 \pm 0.72 \text{ m s}^{-1}$, respectively. The uncertainties agree with the expected uncertainties on the RVs (see Col. 3 of Table 1). The best-fit value for each parameter corresponds to a minimum of χ^2 . The 1σ error bars were determined for all five free parameters following the χ^2 variation as described in Hébrard et al. (2002). The best-fit values together with 1σ error bars are listed in Table 2. We measured $\lambda = -92^{+11}_{-20}$, indicating a nearly polar orbit.

The derived $v \sin i_*$ ($2.8^{+1.9}_{-1.3} \text{ km s}^{-1}$) from the RM anomaly suggested a 2σ detection of the spectral transit. In order to properly determine the significance of our RM detection, we performed Fischer’s classical test. The two models considered for the test were a K (only Keplerian) fit and an RM (Keplerian+RM) fit. The χ^2 for the K and RM fits is 63.55 ($n = 34$) and 28.76 ($n = 30$), respectively. A significant improvement was noted for the second model with $F = 1.95$ ($p = 0.03$) obtained using an F-test. The improvement to the χ^2 was attributed to the RM anomaly detection with 97% confidence. We conclude that the spectroscopic transit is significantly detected.

As a test, we applied a similar grid procedure without the spectroscopic constraint on $v \sin i_*$ from Christiansen et al. (2017). We obtained $\lambda = -91^{+7}_{-16}$, which is within the 1σ uncertainty. The large $v \sin i_*$ obtained here ($4.8 \pm 2.1 \text{ km s}^{-1}$) did not significantly affect the measurement of λ . Because the planetary orbit was found to be polar and it transits near the center of the star ($b = 0.50 \pm 0.32$, Christiansen et al. 2017), the corresponding RM anomaly shape did not place a strong constraint on $v \sin i_*$. The $v \sin i_*$ can be estimated more accurately using the Doppler tomography technique in Sect. 3.3.

Furthermore, the effect of fixed parameters such as r_p/R_* , P , T_0 , T_{14} , and K_b on λ was investigated. When these fixed parameters were varied within their 1σ uncertainty, λ was found to remain within the 1σ uncertainty derived above.

3.2.3. 2017 dataset

Here, we evaluate whether the lower-quality 2017 dataset agrees with the results obtained above using the 2016 dataset. We first determine the observations taken outside the 2017 transit using the same method as explained in Sect. 3.1. After considering uncertainty on T_0 , we found that only one RV measurement was taken clearly outside the transit. The scarcity of data and poor data sampling outside the transit and along with the low-quality observations during 2017 transit prevented us from finding a good model for a Keplerian and finally an independent value of λ . Thus the RM model parameters were fixed to the best-fit values from the 2016 transit, and the model derived previously was scaled to the RV level of this epoch. We also realized that during the 2017 transit, HD 3167 b and HD 3167 c transited simultaneously. However, the expected amplitude of the RM anomaly from HD 3167 b is 0.56 m s^{-1} , which is small compared to the RM signal from HD 3167 c and the RV measurement accuracy.

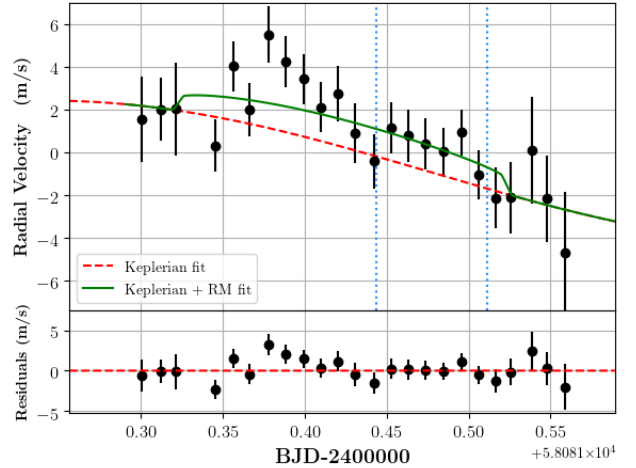


Fig. 2. RV measurement of HD 3167 taken on 2017 November 23 as a function of time. *Upper panel:* solid black circles represent the HARPS-N data, the dashed red line indicates the Keplerian fit, and the green line is the over plotted best-fit RM model from the 2016 transit. The blue dotted line marks the transit ingress and egress of planet b. The expected RM amplitude due to the transit of planet b is 0.6 m s^{-1} . *Lower panel:* residuals after the best-fit RM is subtracted.

Figure 2 shows the best-fit RM model from Sect. 3.2.2 during the 2017 transit and the residuals after the best-fit RM was subtracted. This fit shows that the 2017 dataset roughly agrees with the results obtained from the RM anomaly fit for the 2016 observations; despite its lower quality, it did not invalidate the results presented in Sect. 3.2.2. The residual average inside and outside the transit was found to be $0.23 \pm 1.29 \text{ m s}^{-1}$, and $0.39 \pm 1.66 \text{ m s}^{-1}$, respectively. The obtained uncertainties were slightly larger than the expected uncertainties on the RVs. The 2017 dataset presented short-term variations in the first half of the transit that could not be due to RM or Keplerian effects. We interpreted them as an artifact due to the bad weather conditions. We achieved no significant improvement from fitting the RM anomaly ($F = 0.97$, $p = 0.44$), therefore we considered the spectroscopic transit to be not significantly detected in the 2017 data and did not consider it for further analysis.

3.3. Doppler tomography

Here we present the obliquity measurement we performed on the 2016 dataset using Doppler tomography in order to compare it with the measurement from the RM anomaly technique presented above. When a planet transits its host star, it blocks different regions of the rotating stellar disk, which introduces a Gaussian bump in the spectral lines of the star. This bump can be tracked by inspecting the changes in the CCF, which allows us to measure the obliquity. The stellar rotational speed can also be obtained independent from the spectroscopic estimate by Christiansen et al. (2017). The CCFs obtained from the DRS with the K5 mask were used for this analysis (Sect. 2). Following the approach of Collier Cameron et al. (2010), we considered a model of the stellar CCF, which is the convolution of limb-darkened rotation profile with a Gaussian corresponding to the intrinsic photospheric line profile and instrumental broadening. When the CCFs are fit by the model including the stellar spectrum and the transit signature, some residual fixed patterns appear that are constant throughout the whole night. These patterns, also called “sidelobes” by Collier Cameron et al. (2010), are produced by coincidental random alignments between some

stellar lines and the lines in the mask when the mask is shifted to calculate the CCFs. To remove these patterns, we assumed that they do not vary during the night, and we averaged the residuals of the out-of-transit CCFs after subtracting the best fit to the CCFs that was calculated by considering the stellar spectrum alone. We made a tomographic model that depended on the same parameters as the Keplerian plus RM model (Sect. 3.2), and added the local line profile width, s (non rotating local CCF width) expressed in units of the projected stellar rotational velocity (Collier Cameron et al. 2010). The most critical free parameters to fit the Gaussian bump were λ , $v \sin i_*$, γ , i_p , a/R_* , and s . Other parameters such as P , r_p/R_* , T_0 , and ε were fixed to the same values as were used for the RM fit.

The following merit function was used to fit the CCFs following Bourrier et al. (2015),

$$\chi^2 = \sum_i^{n_{\text{CCF}}} \sum_j^{n_\mu} \left[\frac{f_{i,j}(\text{model}) - f_{i,j}(\text{obs})}{\sigma_i} \right]^2 + \sum_{a_p/R_*, i_p} \left[\frac{x_{\text{tomo}} - x_{\text{photo}}}{\sigma_{x_{\text{photo}}}} \right]^2, \quad (2)$$

where $f_{i,j}$ is the flux at the velocity point j in the i_{th} observed or model CCFs. The error on the CCF estimate was assumed to be constant over the full velocity range for a given CCF. To find the errors σ_i in the CCF profiles, we first used the constant errors, which are the dispersion of the residuals between the CCFs and the best-fit model profiles. As the CCFs were obtained using DRS pipeline with a velocity resolution of 0.25 km s^{-1} and the spectra have a resolution of 7.5 km s^{-1} , the residuals were found to be strongly correlated. This led to an underestimation of the error bars on the derived parameters. A similar analysis as in Bourrier et al. (2015) was used to retrieve the uncorrelated Gaussian component of the CCFs. The residual variance as a function of data binning size (n_{bin}) is well represented by a quadratic harmonic combination of a white and red noise component,

$$\sigma^2(n_{\text{bin}}) = \left(\left(\frac{n_{\text{bin}}}{\sigma_{\text{Uncorr}}^2} \right)^2 + \left(\frac{1}{\sigma_{\text{Corr}}^2} \right)^2 \right)^{-\frac{1}{2}}, \quad (3)$$

where $\sigma_{\text{Uncorr}}/\sqrt{n_{\text{bin}}}$ is the intrinsic uncorrelated noise and σ_{Corr} is the constant term characterizing the correlation between the binned pixels. We adopted Gaussian priors for i_p and a/R_* from photometry (Christiansen et al. 2017).

The planet transit was clearly detected in the CCF profiles, as shown in Fig. 3. The $v \sin i_*$ was found to be $2.1 \pm 0.4 \text{ m s}^{-1}$, which is consistent with the estimate from spectroscopy ($v \sin i_* = 1.7 \pm 1.1 \text{ km s}^{-1}$). The sky-projected obliquity was measured to be $\lambda = -88^\circ \pm 15^\circ$, which is in accordance with the result from the RM analysis (see Sect. 3.2.2). Table 2 lists the best-fit values together with 1σ error bars.

We also performed a test to check the effect of the fixed parameter T_0 by varying it within 1σ error bars. The value of λ remained within the 1σ uncertainty derived above.

3.4. Reloaded Rossiter-McLaughlin technique

We applied the reloaded RM technique (Cegla et al. 2016a; Bourrier et al. 2018) to the HARPS-N observations of HD 3167 c. CCFs computed with the K5 mask (Sect. 2) were first corrected for the Keplerian motion of the star induced by the three planets in the system (calculated with the properties from Christiansen et al. 2017). The CCFs outside of the transit were co-added to build a master-out CCF, whose continuum was normalized to unity. The centroid of the master-out CCF, derived with a

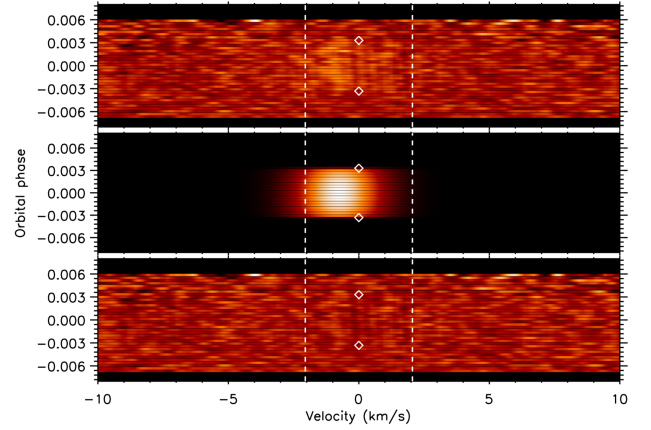


Fig. 3. Maps of the time-series CCFs as a function of RV relative to the star (in abscissa) and orbital phase (in ordinate). The dashed vertical white lines are marked at $\pm v \sin i_*$, and first and fourth contact of transit is indicated by white diamonds. *Upper panel:* map of the transit residuals after the model stellar profile was subtracted. The signature of HD 3167 c is the moderately bright feature that is visible from ingress to egress. *Middle panel:* transiting signature of HD 3167 c using the best-fit model, obtained with $\lambda = -88^\circ$. *Lower panel:* overall residual map after the model planet signature was subtracted.

Gaussian fit, was used to align the CCFs in the stellar rest frame. The continuum of all CCFs was then scaled to reflect the planetary disk absorption by HD 3167 c, using a light curve computed with the batman package (Kreidberg 2015) and the properties from Christiansen et al. (2017). Residual CCFs were obtained by subtracting the scaled CCF from the master-out (Fig. 4).

No spurious features are observed in the residual CCFs out of the transit. Within the transit, the residual RM spectrally and spatially resolve the photosphere of the star along the transit chord. The average stellar lines from the planet-occulted regions are clearly detected and were fit with independent Gaussian profiles to derive the local RVs of the stellar surface. We used a Levenberg-Marquardt least-squares minimization, setting flux errors on the residual CCFs to the standard deviation in their continuum flux. Because the CCFs are oversampled in RV, we kept one in four points to perform the fit. All average local stellar lines were well fit with Gaussian profiles, and their contrast was detected at more than 3σ (using the criterion defined by Allart et al. 2017). The local RV series was fit with the model described in Cegla et al. (2016a) and Bourrier et al. (2017), assuming solid-body rotation for the star. We sampled the posterior distributions of $v \sin i_*$ and λ using the Markov chain Monte Carlo (MCMC) software emcee (Foreman-Mackey et al. 2013), assuming uniform priors. Best-fit values were set to the medians of the distributions, with 1σ uncertainties derived by taking limits at 34.15% on either side of the median. The best-fit model shown in Fig. 4 corresponds to $v \sin i_* = 1.9 \pm 0.3 \text{ km s}^{-1}$ and $\lambda = -112.5^\circ_{-8.5}^{+8.7}$, which agrees at better than 1.4σ with the results obtained from the RM and Doppler tomography (Sects. 3.2 and 3.3). The error bars on λ are small because i_p and a/R_* were fixed in this particular analysis. However, when i_p , T_0 , and a/R_* were varied within their 1σ uncertainty, λ did not vary significantly and remained within 1σ uncertainty. The best-fit values with their 1σ uncertainties are listed in Table 2.

3.5. Comparison between the three methods

The most commonly used method to estimate sky-projected obliquity using RV measurements is the analysis of the RM

Table 2. Best-fit parameters using three methods.

Parameter (unit)	RM fit	Doppler tomography	Reloaded RM	Previously published values
λ (degrees)	-92.0^{+11}_{-20}	-88 ± 15	$-112.5^{+8.7}_{-8.5}$	–
$v \sin i_*$ (km s ⁻¹)	$2.8^{+1.9}_{-1.3}$	2.1 ± 0.4	1.9 ± 0.3	1.7 ± 1.1 (1)
γ (km s ⁻¹)	$19.5310^{+0.0003}_{-0.0002}$	19.530 ± 0.009	19.5286 ± 0.0062	–
i_p (degrees)	$89.5^{+0.3}_{-1.2}$	88.91 ± 0.6	$89.3^{(*)}$	$89.3^{+0.5}_{-0.96}$ (1)
a/R_*	$43.3^{+3.5}_{-16.0}$	36^{+10}_{-7}	$40.323^{(*)}$	$40.323^{+5.55}_{-12.62}$ (1)

Notes. ^(*)Fixed to their photometric value (Christiansen et al. 2017).

References. (1) Christiansen et al. (2017).

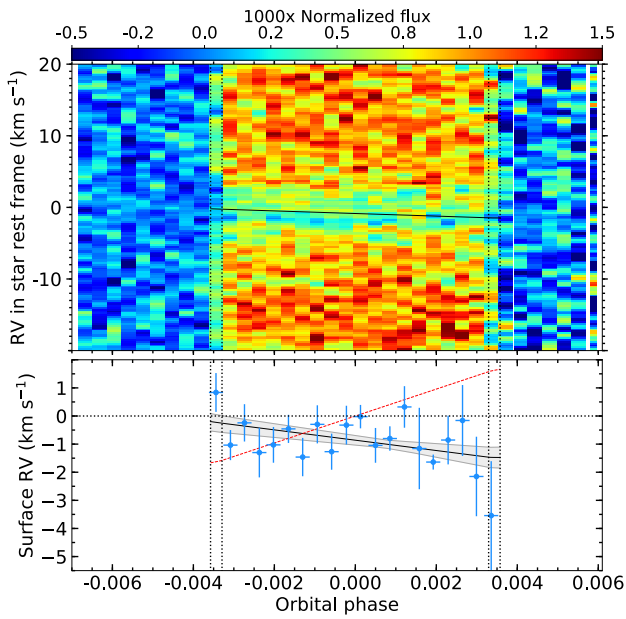


Fig. 4. *Upper panel:* map of the residual CCF series as a function of orbital phase (in abscissa) and RV in the stellar rest frame (in ordinate). Colors indicate flux values. The four vertical dashed black lines show the times of transit contacts. The in-transit residual CCFs correspond to the average stellar line profiles from the regions that are occulted by HD 3167 c across the stellar disk. The solid black line is the best-fit model to the local RVs of the planet-occulted regions ($\lambda = -112.5^\circ$), assuming solid-body rotation for the star ($v \sin i_* = 1.89 \text{ km s}^{-1}$). *Lower panel:* RVs of the stellar surface regions occulted by the planet (blue points), best fit with the solid black line (same as in the upper panel). The gray area corresponds to the 1σ envelope of the best fit, derived from the MCMC posterior distributions. The dashed red line shows a model obtained with the same stellar rotational velocity, but an aligned orbit ($\lambda = 0^\circ$). This highlights the large orbital misalignment of HD 3167 c.

anomaly. However, the RM method does not exploit the full spectral CCF. In some extreme cases, the classical RM method can introduce large biases in the sky-projected obliquity because of asymmetries in the local stellar line profile or variations in its shape across the transit chord (Cegla et al. 2016b). The Doppler tomography method is less affected than the RM anomaly method because it explores the full information in the CCF. However, a bias in the obliquity measurements can also be introduced by assuming a constant, symmetric line profile and ignoring the effects of the differential rotation. Results from the reloaded RM technique suggest that the bias is not significant here. The

reloaded RM technique does not make prior assumptions of the local stellar line profiles and allows a clean and direct extraction of the stellar surface RVs along the transit chord. This results in an improved precision on the obliquity, albeit under the assumption that the transit light-curve parameters (in particular the impact parameter and the ratio of the planet-to-star radius) are known to a good enough precision to be fixed. In the present case, we might thus be underestimating the uncertainties on λ with this method.

The sky-projected obliquities measured by all three methods agree to better than 1.4σ . This confirms that the spectroscopic transit in the 2016 data is significantly detected and suggests that the corresponding obliquity measurement is not reached by strong systematics that would be due to the method. Combining the λ values from all three methods, we estimated the sky-projected obliquity for HD 3167 c to be $\lambda = -97^\circ \pm 23^\circ$, after taking into account both the systematic and statistical errors. We adopted this conservative value in our final obliquity measurement.

As discussed in Sect. 3.2.2, the stellar rotation speed was poorly constrained by the RM method. However, the $v \sin i_*$ more accurately measured from Doppler tomography and the reloaded RM technique was consistent with the measurements of Christiansen et al. (2017). The $v \sin i_*$ from three methods was also found to be within 1σ . Furthermore, the two photometric parameters a/R_* and i_p also agreed within their uncertainties for the RM and Doppler tomography methods. The systemic velocity γ is slightly different in each case because a different definition was employed in each method.

4. Obliquity of planets b and d from geometry

The spectroscopic transit observations gave constraints only on the obliquity of planet c. Although planet b is also transiting, the low amplitude for the RM signal during the transit precludes measuring its obliquity with the present data. However, because both planets b and c are transiting planets, the mutual inclination can be constrained.

We denote by \mathbf{u}_0 the unit vector along the line of sight directed toward Earth and \mathbf{u}_1 a unit vector perpendicular to \mathbf{u}_0 , that is, in the plane of the sky (see Fig. 5). The orbital planes of planets b and c are characterized by the perpendicular unit vectors \mathbf{u}_b and \mathbf{u}_c . The inclination of their orbits, i_b and i_c , is constrained to be $i_b = 83.4^{+4.6}_{-7.7}$ and $i_c = 89.3^{+0.5}_{-0.96}$ (Christiansen et al. 2017). For a planet k (here k stands for either b or d), we define ϕ_k as the angle between \mathbf{u}_1 and the projection of \mathbf{u}_k on the plane of the sky (this is equivalent to the longitude of the ascending node in the plane of the sky). With these definitions,

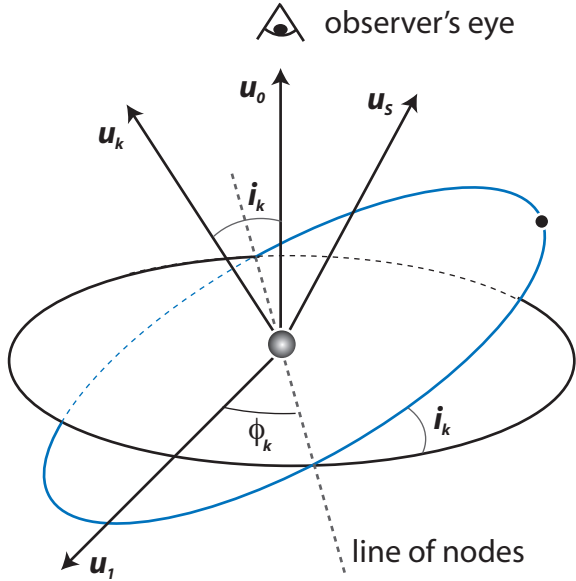


Fig. 5. Pictorial representation of the reference angles and the unit vectors. \mathbf{u}_s corresponds to the direction of the stellar spin.

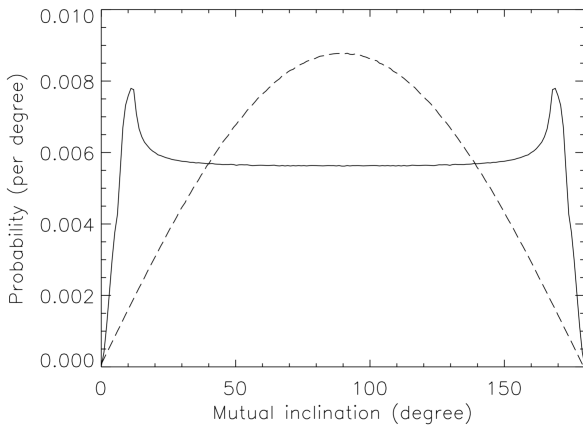


Fig. 6. Probability distribution of the mutual inclination between the planets b and c (solid line). For comparison, the dotted line shows the probability distribution when neither planet transits.

the mutual inclination between the planets b and c, i_{bc} , is given by

$$\cos i_{bc} = \cos i_b \cos i_c + \sin i_b \sin i_c \cos(\phi_b - \phi_c). \quad (4)$$

With $\cos i_b$ and $\cos i_c$ uniformly distributed within their 1σ error bars and assuming that ϕ_b and ϕ_c are uniformly distributed between 0 and 2π , we calculated the probability distribution of i_{bc} (Fig. 6). The probability distribution was found to be close to a uniform distribution, except that it is low for i_{bc} below 10° and above 170° . Based on geometry, no information on the obliquity of planet b can therefore be derived from our measurement of the obliquity of planet c. We note that in the case of two non-transiting planets, the probability distribution of i_{bc} would peak around 90° , as shown by the dotted line in Fig. 6.

Planet d would transit if the condition

$$i_{dc} \leq \arctan\left(\frac{R_\star}{a_d}\right) - (90 - i_c) \quad (5)$$

were fulfilled, where R_\star is the stellar radius and a_d is the semi-major axis of planet d. Because planet d does not transit, the mutual inclination between planets c and d must be at least 2.3° .

As a result, the obliquity of planets b and d cannot be constrained well from the geometry of the planetary system alone. We place constraints on the obliquity of planet d from the dynamics of the planetary system in Sect. 5.

5. Dynamics

We study the dynamics of the system to investigate the interactions between planets and stellar spin which could explain the polar orbit of planet c. We also perform the Hill stability analysis to set bounds on the obliquity of planet d in the following section.

5.1. Planet mutual inclinations

While the available observations were unable to geometrically constrain the mutual inclination of the planets, a bound is given by the stability analysis of the system. Short-period planets with an aligned orbit such as KELT-24 b and WASP-152 b (Rodríguez et al. 2019; Santerne et al. 2016), or with a misaligned orbit such as Kepler-408 b and GJ436 b (Kamiaka et al. 2019; Bourrier et al. 2018) have been detected. The obliquity distribution of short-period planets is not clear. However, because planet b is close to the star, its orbit is most likely circular and its inclination is governed by the interaction with the star, as shown in Appendix A.2. The exact inclination of planet b is not important from a dynamical point of view, and it is safe to neglect the influence of planet b when the stability of the system is investigated. We focus here on the outer pair of planets to constrain the system and study the simplified system that is only composed of the star and the two outer planets. Our goal is to determine the maximum mutual inclination between planets d and c such that the outer pair remains Hill-stable (Petit et al. 2018; Marchal & Bozis 1982). We first created 10^6 realizations of the HD 3167 system by drawing from the best fit of masses, eccentricities, and semi-major axis distributions given by Christiansen et al. (2017). To each of these copies of the system, we set the mutual inclination between planets c and d with uniformly spaced values of between 0° and 90° .

We assumed that the orbit of planet b is in the invariant plane, that is, the plane perpendicular to the angular momentum vector of the whole system¹. As a result, we computed the inclinations i_c and i_d with respect to the invariant plane because the projection of the angular momentum onto the invariant plane gives

$$G_c \sin(i_c) = G_d \sin(i_d), \quad (6)$$

where $G_k = m_k \sqrt{\mathcal{G}M_s a_k (1 - e_k^2)}$ is the norm of the angular momentum of planet k . Then, we computed the total angular momentum deficit (AMD, Laskar 1997) of the system

$$C = \sum_{k=b,c,d} m_k \sqrt{\mathcal{G}M_s a_k} \left(1 - \sqrt{1 - e_k^2} \cos(i_k)\right), \quad (7)$$

and we determined whether the pair d–c is Hill-stable. To do so, we compared the AMD to the Hill-critical AMD of the pair (Eq. (30), Petit et al. 2018). We plot in Fig. 7 the proportion of the Hill-stable system binned by mutual inclination i_{dc} . We also plot the proportion of the Hill-stable pair for a system with circular orbit.

¹ We assumed that planet b is within the invariant plane in order to be able to compute the AMD as a function of the mutual inclination i_{dc} . Nevertheless, the actual planet b's inclination has little influence on the stability of the pair d–c.

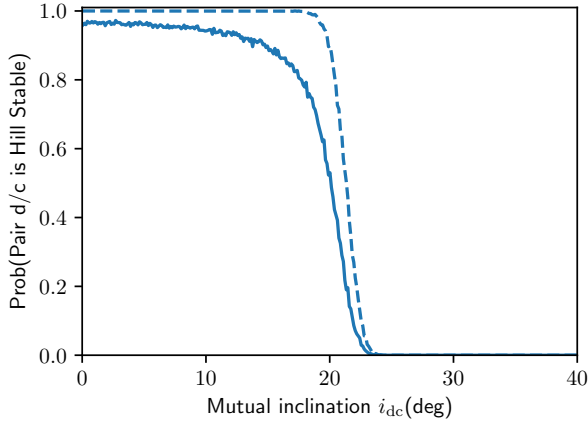


Fig. 7. Probability of the pair d–c to be Hill-stable as a function of the mutual inclination of d and c, assuming planet b is within the invariant plane. The masses, semi-major axes, and eccentricity are drawn from the best-fit distribution (Christiansen et al. 2017). The dashed curve corresponds to a system where every planet is on a circular orbit.

We observe that for an inclination i_{dc} below 21° , the system is almost certainly Hill-stable. This means that for any orbital configuration and masses that are compatible with the observational constraints, the system will be long-lived with this low mutual inclination. We emphasize that long-lived configurations with higher mutual inclination than 21° exist. Christiansen et al. (2017) gave the example of Kozai-Lidov oscillations with initial mutual inclinations of up to 65° . However, the choice of initial conditions is fine-tuned because of the circular orbits (a configuration that is rather unlikely for such dynamically excited systems).

When we assume that the stellar spin is aligned with the total angular momentum of the planets, the planet obliquity corresponds to the planet inclination with respect to the invariant plane. When we assume $i_{dc} < 21^\circ$, the maximum obliquity of planet c is about 9° . Even if the mutual inclination $i_{dc} = 65^\circ$, the obliquity only reaches 32° . Thus, the observed polar orbit shows that the stellar spin cannot be aligned with the angular momentum of the planet.

From Sect. 4 and the previous paragraphs, we deduce that the most likely value for i_{dc} is between 2.3° and 21° . Because the mutual inclination of planets c and d is low, we can conclude that planet d is also nearly polar.

5.2. Interactions of planets and stellar spin

Because the system’s eccentricities and mutual inclinations are most likely low to moderate, we considered the interaction between the stellar spin and the planetary system. In particular, we investigated whether the motion of the planets can effectively tilt the star up to an inclination that could explain the polar orbit of planets c and d. The currently known estimate of Christiansen et al. (2017) of the stellar rotation period is 27.2 ± 7 days, but the period may have slowed down by a factor 10 (Bouvier 2013). In order to investigate the evolution of the obliquity that could have occurred in earlier stages in the life of the system, we studied the planet-star interaction as a function of the stellar rotation period.

To do so, we applied the framework of the integrable three-vector problem to the star and the angular momenta of planets d and c (Boué & Laskar 2006; Boué & Fabrycky 2014; Correia 2015). This model gives both the qualitative and quantitative behavior of the evolution of three vectors that represent different

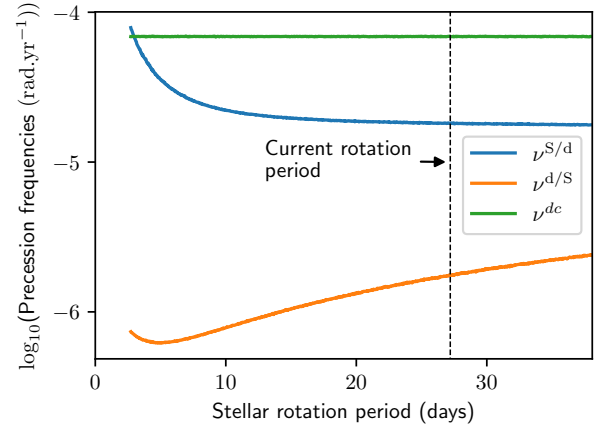


Fig. 8. Characteristic frequencies defined in Eq. (A.5) as a function of stellar period. The current estimated stellar rotation period is marked with a vertical dashed line. The two terms $\nu^{d/S}$ and $\nu^{c/d}$ are merged into a single curve ν^{dc} because they are almost equal.

angular momenta directions \mathbf{u}_S , \mathbf{u}_d , and \mathbf{u}_c under their mutual interactions. We describe the model in Appendix A.

As shown in Boué & Fabrycky (2014), the mutual interactions of the three vectors can be described by comparing the different characteristic frequencies² of the system $\nu^{d/S}$, $\nu^{S/d}$, $\nu^{d/c}$, and $\nu^{c/d}$ with the expressions given in Eq. (A.5). The frequency $\nu^{j/k}$ represents the relative influence of the body j over the motion of \mathbf{u}_k . In other words, if $\nu^{k/j} \ll \nu^{j/k}$, \mathbf{u}_j is almost constant while \mathbf{u}_k precesses around. We here neglect the interactions between the star and planet c versus the interaction between the star and planet d because they are smaller by two orders of magnitude.

Because it is coupled with the star, planet b acts as a bulge on the star that enhances the coupling between the orbits of the outer planets and the star (see Appendix A.2). We limit our study to the configuration where the strongest coupling occurs, that is, when the orbit of planet b lies within the stellar equatorial plane. The influence of planet b modifies the characteristic frequencies $\nu^{d/S}$ and $\nu^{S/d}$, as we show in Appendix A.2. The model is valid in the secular approximation if the eccentricities of planets d and c remain low such that G_d and G_c are constant. Boué & Laskar (2006) showed that the motion is quasi-periodic. It is possible to give the maximum spin-orbit angle of planet c as a function of the initial inclination of planet d.

Using the classification of Boué & Fabrycky (2014), we can determine the maximum misalignment between \mathbf{u}_S and \mathbf{u}_c as a function of the initial inclination between \mathbf{u}_S and \mathbf{u}_d . We plot the frequencies (cf. Eq. (A.5)) as a function of the stellar rotation period in Fig. 8. We merged the curves that represent $\nu^{d/c}$ and $\nu^{c/d}$ into ν^{dc} because the two terms are almost equal.

We are in a regime where $(\nu^{d/c} \sim \nu^{c/d}) \gg (\nu^{d/S}, \nu^{S/d})$ and the orbital frequencies dominate the interactions with the star. For the shorter periods we have $(\nu^{d/c} \sim \nu^{c/d} \sim \nu^{S/d}) \gg \nu^{d/S}$. Nonetheless, in both cases the dynamics are purely orbital, however, meaning that the star acts as a point mass and is never coupled with the orbits of the outer planets. It is not possible for planets c and d to reach a high mutual inclination with the stellar spin axis starting from almost coplanar orbits or an even

² The characteristic frequencies designate the coupling parameters between the different vectors, as explained in Appendix A. They have the dimension of a frequency, but are not properly speaking the frequencies of the system. Here, we use the terminology introduced in Boué & Fabrycky (2014).

moderate inclination. When planet b is misaligned with the star, it is even harder for the planets to tilt the star.

We conclude that even if the star has had a shorter period in the past, it is unlikely that the currently observed system can by itself generate such a high obliquity for planets c and d. However, high initial obliquities are almost conserved, which means that the observed polar orbits are possible under the assumptions made, even though they are not explained by this scenario.

5.3. System tilt due to an unseen companion

We now assume that while the system only presents moderate inclinations, a distant companion on an inclined orbit exists. We consider the configurations that can cause the system to be tilted with respect to the star. Once again, we used the framework of [Boué & Fabrycky \(2014\)](#). We considered the vectors \mathbf{u}_S , \mathbf{u} , and \mathbf{u}' that give the direction of the stellar spin axis \mathbf{S} , the total angular momentum of the planetary system \mathbf{G} , and the angular momentum of the companion \mathbf{G}' , respectively. The outer companion is described by its mass m' , its semi-major axis a' , its semi-minor axis $b' = a' \sqrt{1 - e'^2}$, and its initial inclination I_0 with respect to the rest of the system, which is assumed to be nearly coplanar or to have moderate inclinations. Moreover, we assumed that \mathbf{G} is initially aligned with \mathbf{S} , while the companion is highly inclined with respect to the planetary system, that is to say, I_0 is larger than 45° up to 90° . According to [Boué & Fabrycky \(2014\)](#), all interactions between planets cancel out because we only consider the dynamics of their total angular momentum \mathbf{G} .

As in the previous part, we can compare the different characteristic frequencies of the system $\nu^{\text{pla}/S}$, $\nu^{S/\text{pla}}$, $\nu^{\text{comp}/\text{pla}}$, and $\nu^{\text{pla}/\text{comp}}$ of expression given in Eqs. (A.6) and (A.7). The companion effectively tilts the planetary system as a single body if its influence on planet c is weaker than the interaction between planets d and c. In the other case, planet c will enter Lidov-Kozai oscillations, which can lead to the destabilization of the system through the interactions with planet d. [Boué & Fabrycky \(2014\)](#) reported the limit at which the outer companion starts to perturb the planetary system and excites the outer planet through Kozai-Lidov cycles. They explained that if the coefficient β_{KL} is defined as

$$\beta_{\text{KL}} = \frac{m'}{m_d} \left(\frac{a_c}{a_d} \right)^2 \left(\frac{a_c}{b'} \right)^3 \quad (8)$$

and verifies $\beta_{\text{KL}} \ll 1$, the companion's influence does not perturb the system and tilts it as a whole.

We plot in Fig. 9 the frequencies $\nu^{\text{pla}/S}$, $\nu^{S/\text{pla}}$, $\nu^{\text{comp}/\text{pla}}$, and $\nu^{\text{pla}/\text{comp}}$ as a function of β_{KL} and observe different regimes. In the first regime, we have $\beta_{\text{KL}} < 0.1$ and $\nu^{\text{pla}/\text{comp}} \ll \nu^{\text{comp}/\text{pla}} \ll \nu^{S/\text{pla}}$. The influence of the companion is too weak to change the obliquity of the planetary system. For $\beta_{\text{KL}} > 1$, we have $(\nu^{\text{pla}/\text{comp}} \sim \nu^{\text{comp}/\text{pla}}) \gg \nu^{S/\text{pla}}$, in which regime the system obliquity can reach I_0 . However, the companion destabilizes the orbit of planet c, which can lead to an increase in eccentricity and mutual inclination between the planets. For $0.1 \lesssim \beta_{\text{KL}} \lesssim 1$, we remark that $\nu^{\text{pla}/S} \ll (\nu^{\text{pla}/\text{comp}} \sim \nu^{\text{comp}/\text{pla}} \sim \nu^{S/\text{pla}})$. According to [Boué & Fabrycky's](#) classification, the maximum possible inclination between the star and the planet, that is, their obliquity, is almost twice I_0 for $I_0 \lesssim 80^\circ$. In this regime, an unseen companion can explain the observed polar orbits of HD 3167 c and d.

We conclude that some stable configurations with an additional outer companion may explain the high obliquity of planets c and d. We further discuss the possible presence of outer companion signals in the existing RV data in Sect. 6. Accurate

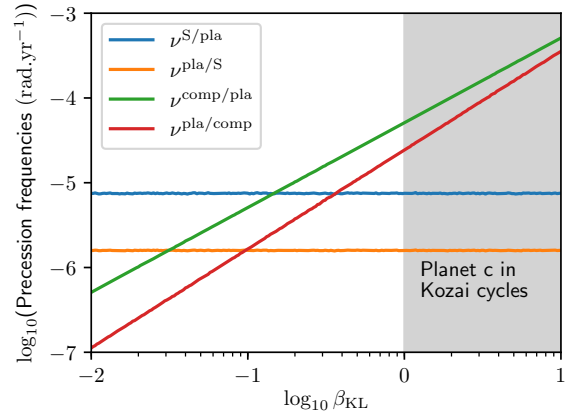


Fig. 9. Characteristic frequencies defined in Eq. (A.6) as a function of β_{KL} (see Eq. (8)). For $\beta_{\text{KL}} > 1$, the outer companion can destabilize the observed system.

measurement of the eccentricities of planets d and c will also help to constrain this scenario better.

6. Outer companion

To find the possible signatures of an outer companion, we performed two different tests on the RV data from [Christiansen et al. \(2017\)](#), which cover a span of five months. First we obtained the residual RV after we removed the Keplerian signal caused by the three planets. In the analysis performed by [Christiansen et al. \(2017\)](#), the linear drift was fixed to $0 \text{ m s}^{-1} \text{ yr}^{-1}$ before the Keplerian was fit. However, we detected a linear drift of about $7.6 \pm 1.6 \text{ m s}^{-1} \text{ yr}^{-1}$ in the residual velocities. When we assume a circular orbit for the outer companion, this linear drift corresponds to a period of at least 350 days and a mass of at least $0.1 M_{\text{Jup}}$. A body like this has a $\beta_{\text{KL}} \approx 0.08$, which makes it unlikely that it is able to incline planets c and d with respect to the star.

Second, we generated the periodogram of the RV before and after we removed the known periodic signals of the three planets using the Lomb-Scargle method, as shown in Fig. 10. In addition to the detected planets, two other peaks at 11 days and 78 days were found at a false-alarm probability (FAP) higher than 0.1% in the Fourier power. The peak at 11 days was an alias caused by the concentration of the sampling around lunar cycles, as explained in [Christiansen et al. \(2017\)](#). In the lower panel of Fig. 10, no peak at 11 days was detected, but the peak at 78 days was persistent in both periodograms. The peak around 20 days in the lower panel may be caused by stellar rotation, and the peak around one day was an alias due to data sampling. When we assume a circular orbit with a period of 78 days, this corresponds to a mass of at least $0.03 M_{\text{Jup}}$ for the outer companion, which gives $\beta_{\text{KL}} \approx 0.5$. This potential outer companion might explain the high obliquity of HD 3167 c if its initial inclination I_0 was high enough.

We found possible indications of an additional outer companion in the system. Additional RV observations of HD 3167 on a long time span are necessary to conclusively establish its presence and determine its orbital characteristics, and thus confirm (or refute) our hypothesis.

7. Conclusion

We used new observations obtained with HARPS-N to measure the obliquity of a sub-Neptune in a multi-planetary system. The three different methods we applied on this challenging dataset

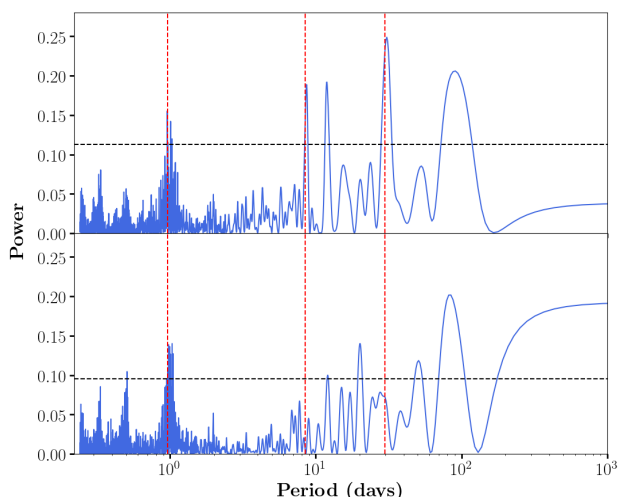


Fig. 10. *Upper panel:* Lomb-Scargle periodogram of the RV of HD 3167 taken from Christiansen et al. (2017). The black dashed line represents the false-alarm probability at 0.1%, and the three vertical red dashed lines correspond to the periods of the three planets that are currently detected around HD 3167. *Lower panel:* Lomb-Scargle periodogram of the RV data after the three known periodic signals are removed.

agree, which means that the sky-projected obliquity we measured is reliable. We report a nearly polar orbit for the HD 3167 c with $\lambda \sim -97^\circ \pm 23^\circ$. The measurements of λ from RM anomaly, Doppler tomography, and reloaded RM technique agree at better than 1.4σ standard deviation with this value. The $v \sin i_*$ from the three methods also agree within their uncertainties. To our knowledge, we are the first to apply these three methods and compared them to the spectroscopic observation of a planetary transit.

These observations are a valuable addition to the known planetary obliquity sample, extending it further beyond hot Jupiters. Several small-radius multi-planet systems with aligned spin-orbits such as Kepler 30 (Sanchis-Ojeda et al. 2012) and with a misaligned spin-orbit such as Kepler 56 (Huber et al. 2013) have been reported. Additionally, single small exoplanets with high-obliquity measurement such as Kepler 408 (Kamiaka et al. 2019) and GJ436 (Bourrier et al. 2018) have also been reported. Some of the misalignments might be explained by the presence of an outer companion in the system. One particularly interesting planetary system is Kepler 56, in which two of its transiting planets are misaligned with respect to the rotation axis of their host star. This misalignment was explained by the presence of a massive non-transiting companion in the system (Huber et al. 2013). A third planet in the Kepler 56 system was later discovered by Otor et al. (2016). This supported the finding of Huber et al. (2013). Similarly, the misalignment in HAT-P-11 b may be explained by the presence of HAT-P-11 c (Yee et al. 2018).

Our dynamical analysis of the system HD 3167 places constraints on the obliquity of planet d. We cannot determine the obliquity of planet b with the current data and information about the system. The Hill-stability criterion shows that the orbits of planets c and d are nearly coplanar, so that both planets are in nearly polar orbits. The interactions of the planets with the stellar spin cannot satisfactorily explain the polar orbits of planets c and d. We postulate that an additional unseen companion exists in the system. This might explain the polar orbits of planets c and d. Indications for additional outer companions are present in the available RV dataset. Continued RV measurements of HD 3167

on a longer time span might reveal the outer companion and confirm our speculation.

Acknowledgements. A.P. thanks G. Boué for the helpful discussions during the study. A.C. acknowledges support from the CFISUC strategic project (UID/FIS/04564/2019), ENGAGE SKA (POCI-01-0145-FEDER-022217), and PHOBOS (POCI-01-0145-FEDER-029932), funded by COMPETE 2020 and FCT, Portugal. V.B. acknowledges support by the Swiss National Science Foundation (SNSF) in the frame of the National Centre for Competence in Research PlanetS, and has received funding from the European Research Council (ERC) under the European Union's Horizon 2020 research and innovation programme (project Four Aces; grant agreement No 724 427). S.D. acknowledges Vaibhav Pant for insightful discussions.

References

- Albrecht, S., Winn, J. N., Marcy, G. W., et al. 2013, *ApJ*, 771, 11
Allart, R., Lovis, C., Pino, L., et al. 2017, *A&A*, 606, A144
Baranne, A., Queloz, D., Mayor, M., et al. 1996, *A&AS*, 119, 373
Bate, M. R., Lodato, G., & Pringle, J. E. 2010, *MNRAS*, 401, 1505
Batygin, K. 2012, *Nature*, 491, 418
Boué, G., & Fabrycky, D. C. 2014, *ApJ*, 789, 111
Boué, G., & Laskar, J. 2006, *Icarus*, 185, 312
Bourrier, V., & Hébrard, G. 2014, *A&A*, 569, A65
Bourrier, V., Lecavelier des Etangs, A., Hébrard, G., et al. 2015, *A&A*, 579, A55
Bourrier, V., Cegla, H. M., Lovis, C., & Wyttenbach, A. 2017, *A&A*, 599, A33
Bourrier, V., Lovis, C., Beust, H., et al. 2018, *Nature*, 553, 477
Bouvier, J. 2013, *EAS Pub. Ser.*, 62, 143
Cébron, D., Moutou, C., Le Bars, M., Le Gal, P., & Farès, R. 2011, *Eur. Phys. J. Web Conf.*, 11, 03003
Cegla, H. M., Lovis, C., Bourrier, V., et al. 2016a, *A&A*, 588, A127
Cegla, H. M., Oshagh, M., Watson, C. A., et al. 2016b, *ApJ*, 819, 67
Christiansen, J. L., Vanderburg, A., Burt, J., et al. 2017, *AJ*, 154, 122
Collier Cameron, A., Bruce, V. A., Miller, G. R. M., Triaud, A. H. M. J., & Queloz, D. 2010, *MNRAS*, 403, 151
Correia, A. C. M. 2015, *A&A*, 582, A69
Correia, A. C. M., Laskar, J., Farago, F., & Boué, G. 2011, *Celest. Mech. Dyn. Astron.*, 111, 105
Crouzet, N., McCullough, P. R., Long, D., et al. 2017, *AJ*, 153, 94
d'Alembert, J. L. R. 1749, Recherches sur la précession des équinoxes: et sur la nutation de l'axe de la Terre, dans le système newtonien (Chez David l'ainé)
Fabrycky, D., & Tremaine, S. 2007, *ApJ*, 669, 1298
Foreman-Mackey, D., Hogg, D. W., Lang, D., & Goodman, J. 2013, *PASP*, 125, 306
Gandolfi, D., Barragán, O., Hatzes, A. P., et al. 2017, *AJ*, 154, 123
Gaudi, B. S., & Winn, J. N. 2007, *ApJ*, 655, 550
Guillochon, J., Ramirez-Ruiz, E., & Lin, D. 2011, *ApJ*, 732, 74
Hébrard, G., Lemoine, M., Vidal-Madjar, A., et al. 2002, *ApJS*, 140, 103
Hébrard, G., Bouchy, F., Pont, F., et al. 2008, *A&A*, 488, 763
Hirano, T., Narita, N., Sato, B., et al. 2012, *ApJ*, 759, L36
Huber, D., Carter, J. A., Barbieri, M., et al. 2013, *Science*, 342, 331
Kamiaka, S., Benomar, O., Suto, Y., et al. 2019, *AJ*, 157, 137
Kreidberg, L. 2015, *PASP*, 127, 1161
Lai, D., Foucart, F., & Lin, D. N. C. 2011, *MNRAS*, 412, 2790
Lambeck, K. 1988, *Geophysical Geodesy – The Slow Deformations of the Earth* (New York: Oxford University Press)
Landin, N. R., Mendes, L. T. S., & Vaz, L. P. R. 2009, *A&A*, 494, 209
Laskar, J. 1997, *A&A*, 317, L75
López-Morales, M., Triaud, A. H. M. J., Rodler, F., et al. 2014, *ApJ*, 792, L31
Marchal, C., & Bozis, G. 1982, *Celest. Mech.*, 26, 311
Nagasawa, M., Ida, S., & Bessho, T. 2008, *ApJ*, 678, 498
Ohta, Y., Taruya, A., & Suto, Y. 2005, *ApJ*, 622, 1118
Otor, O. J., Montet, B. T., Johnson, J. A., et al. 2016, *AJ*, 152, 165
Pepe, F., Mayor, M., Rupprecht, G., et al. 2002, *The Messenger*, 110, 9
Petit, A. C., Laskar, J., & Boué, G. 2018, *A&A*, 617, A93
Queloz, D., Eggenberger, A., Mayor, M., et al. 2000, *A&A*, 359, L13
Rodríguez, J. E., Eastman, J. D., Zhou, G., et al. 2019, *AJ*, accepted [arXiv:1906.03276]
Sanchis-Ojeda, R., Fabrycky, D. C., Winn, J. N., et al. 2012, *Nature*, 487, 449
Santerne, A., Hébrard, G., Lillo-Box, J., et al. 2016, *ApJ*, 824, 55
Tremaine, S. 1991, *Icarus*, 89, 85
Triaud, A. H. M. J., Collier Cameron, A., Queloz, D., et al. 2010, *A&A*, 524, A25
Vanderburg, A., Bieryla, A., Duvv, D. A., et al. 2016, *ApJ*, 829, L9
Winn, J. N., Johnson, J. A., Howard, A. W., et al. 2010, *ApJ*, 723, L223
Yee, S. W., Petigura, E. A., Fulton, B. J., et al. 2018, *AJ*, 155, 255

Appendix A: Details on the three-vector model

A.1. Generic three-vector problem

The three-vector problem (Boué & Laskar 2006; Boué & Fabrycky 2014) studies the evolution of the direction of three angular momenta that are represented by the unit vectors \mathbf{u}_k for $k = 1, 2, 3$ in equations

$$\begin{aligned} \frac{d\mathbf{u}_1}{dt} &= -\nu^{2/1}(\mathbf{u}_1 \cdot \mathbf{u}_2) \mathbf{u}_2 \times \mathbf{u}_1 - \nu^{3/1}(\mathbf{u}_1 \cdot \mathbf{u}_3) \mathbf{u}_3 \times \mathbf{u}_1 \\ \frac{d\mathbf{u}_2}{dt} &= -\nu^{1/2}(\mathbf{u}_1 \cdot \mathbf{u}_2) \mathbf{u}_1 \times \mathbf{u}_2 - \nu^{3/2}(\mathbf{u}_2 \cdot \mathbf{u}_3) \mathbf{u}_3 \times \mathbf{u}_2 \\ \frac{d\mathbf{u}_3}{dt} &= -\nu^{1/3}(\mathbf{u}_1 \cdot \mathbf{u}_3) \mathbf{u}_1 \times \mathbf{u}_3 - \nu^{2/3}(\mathbf{u}_2 \cdot \mathbf{u}_3) \mathbf{u}_2 \times \mathbf{u}_3. \end{aligned} \quad (\text{A.1})$$

The constants $\nu^{k/j}$ are called the characteristic frequencies and represent the relative influence of the body k over the evolution of j . Their expression depends on the considered problem. The three-vector problem is integrable (Boué & Laskar 2006), and the solution is quasi-periodic with two different frequencies. Given an initial state where two vectors are aligned and a third is misaligned, it is possible to compute the maximum inclination between the two initially aligned vectors as a function of the initial inclination with the third (Boué & Fabrycky 2014). The maximum inclination depends on the characteristic frequencies, and the different cases have been classified in Sect. 5.3 of Boué & Fabrycky (2014).

A.2. Influence of planet b

In Sects. 5.1 and 5.2, we claimed that the inclination dynamics of planet b are most likely governed by the star and only influence planets d and c through a modification of the planet–star coupling. We present here the justification for this assumption as well as details on the expressions of the coupling constants.

We first focus on the three-vector problem ($\mathbf{u}_S, \mathbf{u}_b$, and \mathbf{u}_d). For now, we neglect the effect of planet c because we focus on the dynamics of planet b. Following Boué & Laskar (2006) and Boué & Fabrycky (2014), the characteristic frequencies that appear in Eq. (A.1) are expressed as

$$\begin{aligned} \nu^{b/S} &= \frac{\alpha_{Sb}}{S}, & \nu^{d/S} &= \frac{\alpha_{Sd}}{S}, & \nu^{b/d} &= \frac{\beta_{bd}}{G_d}, \\ \nu^{S/b} &= \frac{\alpha_{Sb}}{G_b}, & \nu^{S/d} &= \frac{\alpha_{Sd}}{G_d}, & \nu^{d/b} &= \frac{\beta_{bd}}{G_b}, \end{aligned} \quad (\text{A.2})$$

where G_k is the angular momentum of planet k , $S = C_S \omega_S$ is the angular momentum of the stellar rotation, with C_S the stellar moment of inertia and

$$\begin{aligned} \alpha_{Sj} &= \frac{3 \mathcal{G} M_S m_j J_2 R_\star^2}{2 a_j^3}, \\ \beta_{jk} &= \frac{1}{4} \frac{\mathcal{G} m_j m_k a_j}{a_k^2} b_{3/2}^{(1)} \left(\frac{a_j}{a_k} \right). \end{aligned} \quad (\text{A.3})$$

Here α_{Sj} represents the coupling between the star and planet j , and β_{jk} is the Laplace-Lagrange coupling between planets j and k (we assume $a_j < a_k$). We also define

$$J_2 = \frac{k_2 \omega_S^2 R_\star^3}{3 \mathcal{G} M_S}, \quad (\text{A.4})$$

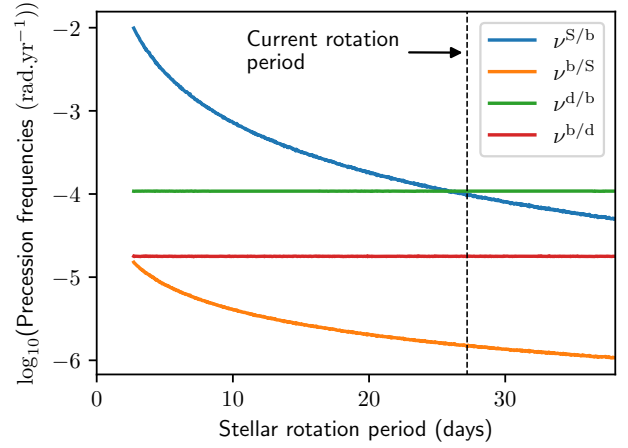


Fig. A.1. Characteristic frequencies defined in Eq. (A.2) as a function of the stellar period. The current stellar rotation period is marked with a vertical dashed line. $\nu^{b/S}$ dominates for most of the considered frequencies.

the gravitational quadrupole coefficient (Lambeck 1988), where k_2 is the second fluid Love number of the star and ω_S is the stellar rotation speed. For the numerical values of k_2 and C_S , we use Landin et al. (2009). For a star of mass $0.85 M_\odot$, we have $k_2 = 0.018$ and $C_S/(M_S R_\star^2) = 0.10$.

Independently of the stellar rotation speed, we have $\alpha_{Sd}/\alpha_{Sb} \leq 0.04$. We therefore neglect the terms depending on α_{Sd} in this analysis. As a result, we can directly apply the results of the analysis reported by Boué & Fabrycky (2014), with the four characteristic frequencies $\nu^{b/S}$, $\nu^{S/b}$, $\nu^{b/d}$, and $\nu^{d/b}$.

We plot the frequencies $\nu^{k/j}$ as a function of the stellar period in Fig. A.1. We average the frequencies in each point by randomly drawing the orbital elements from the best fit.

For the considered range of the stellar revolution period, $\nu^{S/b}$ dominates all other frequencies, and it becomes comparable to $\nu^{d/b}$ for the current rotation rate. Using the regime classification of Boué & Fabrycky (2014), we can determine the maximum misalignment between \mathbf{u}_S and \mathbf{u}_b as a function of the initial inclination between \mathbf{u}_S and \mathbf{u}_d .

For a faster-rotating star (i.e., a younger star), we have $\nu^{S/b} \gg (\nu^{b/S}, \nu^{d/b}, \nu^{b/d})$, in which regime no significant misalignment of planet b can be achieved. As a result, planet b is completely coupled with the star and remains within its equator even if the other planets are mutually inclined. The current rotation rate leads to the so-called Laplace regime where $(\nu^{S/b} \sim \nu^{d/b}) \gg (\nu^{b/S}, \nu^{b/d})$, in which the plane of planet b oscillates between the stellar equatorial plane and the plane of planet d. However, if the initial mutual inclination between planet b and the stellar equator is low, planet b remains close to the stellar equator.

We simplify the problem by considering that planet b is coupled to the star and modifies the stellar precession coupling constant α_{Sk} for planets d and c. The modification of the coupling constant can be found in Boué & Laskar (2006, Eq. (129))³. While the expression was derived for a planet in the presence of a satellite, it remains valid in our case. The expression is a generalization of the approximations for close satellites (Tremaine 1991) and far satellites (d’Alembert 1749). We denote with $\tilde{\alpha}_{Sk}$ the modified coupling constant to include the effect of planet b when it is considered as a bulge on the star.

³ This equation gives the value of $\tilde{\alpha}_{Sk}/S$, but it is straightforward to compute $\tilde{\alpha}_{Sk}$ from it.

A.3. Coupling constants for the interactions of the planet with the star

In Sect. 5.2 we considered the three vectors \mathbf{u}_s , \mathbf{u}_d , and \mathbf{u}_c . The coupling frequencies that appear in Eq. (A.1) for this particular problem are given by

$$\begin{aligned} \nu^{d/s} &= \frac{\tilde{\alpha}_{sd}}{S}, & \nu^{c/s} &= \frac{\tilde{\alpha}_{sc}}{S}, & \nu^{d/c} &= \frac{\beta_{dc}}{G_c}, \\ \nu^{s/d} &= \frac{\tilde{\alpha}_{sb}}{G_d}, & \nu^{s/c} &= \frac{\tilde{\alpha}_{sc}}{G_c}, & \nu^{c/d} &= \frac{\beta_{dc}}{G_d}, \end{aligned} \quad (\text{A.5})$$

where β_{bd} is defined in Eq. (A.3) and $\tilde{\alpha}_{sk}$ is the coupling between the star and planet k , modified to take the influence of planet b into account, as explained in Appendix A.2. We also simplified Eqs. (A.1) by neglecting $\tilde{\alpha}_{sc}$ over $\tilde{\alpha}_{sd}$ because $\tilde{\alpha}_{sc}/\tilde{\alpha}_{sd} < 0.05$ independently of the stellar rotation period.

A.4. Coupling constants for the problem with a companion

The characteristic frequencies that govern the evolution of the inclination of the planets under the influence of an outer companion as explained in Sect. 5.3 are given by

$$\begin{aligned} \nu^{\text{pla}/s} &= \frac{\alpha}{S}, & \nu^{\text{pla}/\text{comp}} &= \frac{\Gamma}{G'}, \\ \nu^{s/\text{pla}} &= \frac{\alpha}{G}, & \nu^{\text{comp}/\text{pla}} &= \frac{\Gamma}{G}, \end{aligned} \quad (\text{A.6})$$

where

$$\begin{aligned} \alpha &= \sum_{j=b,c,d} \frac{3 \mathcal{G} M_s m_j J_2 R_\star^2}{2 a_j^3}, \\ \Gamma &= \sum_{j=b,c,d} \frac{3 \mathcal{G} m' m_j a_j^2}{4 b'^3}. \end{aligned} \quad (\text{A.7})$$

We neglect the interaction between the star and the companion and as a result disregard the corresponding characteristic frequencies.

Appendix B: Radial velocity data

Table B.1. Radial velocities measured on 2017 November 23 with HARPS-N.

BJD	RV (m s ⁻¹)	Uncertainty (m s ⁻¹)
58 081.30053	19 534.14	1.79
58 081.31183	19 534.61	1.22
58 081.3213	19 534.61	2.02
58 081.34556	19 532.9	0.88
58 081.35606	19 536.62	0.84
58 081.36645	19 534.57	0.91
58 081.3777	19 538.11	0.99
58 081.38814	19 536.84	0.83
58 081.3992	19 536.02	0.79
58 081.40971	19 534.7	0.81
58 081.42024	19 535.33	0.97
58 081.43089	19 533.49	1.11
58 081.44223	19 532.18	0.95
58 081.45276	19 533.73	0.87
58 081.46325	19 533.37	0.89
58 081.47383	19 532.98	0.83
58 081.48465	19 532.62	0.71
58 081.49539	19 533.53	0.66
58 081.5059	19 531.55	0.77
58 081.51666	19 530.46	1.16
58 081.52598	19 530.48	1.45
58 081.53888	19 532.69	2.33
58 081.54778	19 530.42	1.85
58 081.55897	19 527.89	2.72

5.2.3 Results and Conclusion

New observations obtained with HARPS-N were used to measure the obliquity of a sub-Neptune HD 3167 c in a multi-planetary system. Three different methods - classical Rossiter-McLaughlin, Doppler Shadow and, Reloaded Rossiter-McLaughlin, were used to measure the sky-projected obliquity. HD 3167 c is found to be in a nearly polar orbit with $\lambda \sim -97 \pm 23$ degrees. The measurements of λ obtained from three methods agree at better than 1.4σ standard deviation with this value.

The dynamical analysis of the system HD3167 also places constraints on the obliquity of planet d. The Hill stability criterion shows that the planets c and d are nearly co-planar. HD 3167 c and d are thus both in nearly polar orbits. Additionally, it was postulated that an additional unseen companion exists in the system, which might explain the polar orbits of planets c and d. Indications for additional outer companions are present in the available RV dataset. Continued RV measurements of HD3167 on a longer time span might reveal the outer companion and confirm/refute this speculation.

5.2.4 Additional Information - True Obliquity

The true obliquity of HD 3167 c can be derived by using Eq. 2.14. To find the value of stellar inclination I_S , the values of the stellar radius and $V_S \sin I_S$ are taken from the C17 and star rotation period from [Gandolfi et al. \(2017\)](#). Using Eq. 2.15, the I_S is found to be nearly equator-on, but it has large uncertainties because of the large uncertainties in the above quantities. Therefore, this approach cannot be applied to find true obliquity for this system.

5.3 Revisiting obliquity of HD 189733 with SPIRou

HD 189733 is a binary star system at close distance, i.e., 19.3 pc, from the Sun. The primary star is a K dwarf star while the secondary star is an M red dwarf star. The star is visible using binoculars 0.3 degrees east of the Dumbbell Nebula (M27). HD 189733 hosts a transiting hot Jupiter HD 189733A b, around its primary star HD 189733 A. [Bouchy et al. \(2005\)](#) detected HD 189733A b using the radial velocity technique and the transit method at OHP in 2005 (see figure 5.5). They also found the RM anomaly signal due to the Rossiter-McLaughlin effect, but it was not fitted to obtain the sky projected obliquity.

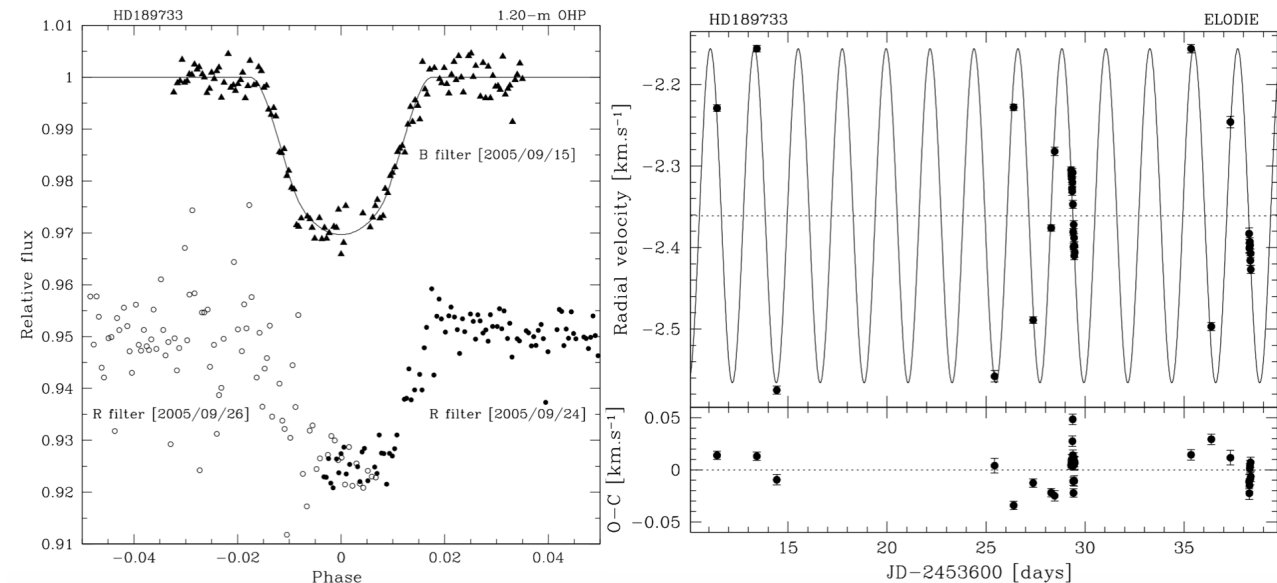


Figure 5.5 – *Left panel*: The transit light curve of HD 189733 observed with 1.2 m OHP telescope along with the best-fit model for the B-band transit. *Right panel*: Radial velocity measurements of HD 189733 with ELODIE spectrograph at OHP along with best Keplerian solution. Figure credits: ([Bouchy et al., 2005](#))

5.3.1 Stellar and planetary parameters

HD 189733 A (hereafter HD 189733) is a K-type star in the northern hemisphere with a visual magnitude $V = 7.67$. The star is a moderately active star with a $\log R_{HK}$ of -4.5 and has a metallicity (Fe/H) of -0.03 dex. It has a projected rotational velocity of about 3.3 km s^{-1} . HD 189733 has a mass of $0.806 M_{\odot}$ and a radius of $0.758 R_{\odot}$. This system has been extensively studied in different wavelengths since its discovery.

HD 189733 b is a transiting planet with an orbital period of 2.218 days. It is a hot Jupiter of the mass of $1.154 M_J$, and radius of $1.184 R_J$, which corresponds to a density of 0.86 g cm^{-3} . [Winn et al. \(2006\)](#) were the first to present the sky projected obliquity of the exoplanet HD 189733 b, $\lambda = -1.4 \pm 1.1$ degrees by modeling the Rossiter-McLaughlin effect (classical Rossiter-McLaughlin). HD 189733 has also been considered for testing new models for finding sky-projected obliquity such as Doppler Shadow by [Collier Cameron et al. \(2010\)](#) and Reloaded RM by [Cegla et al. \(2016\)](#).

5.3.2 Keplerian Orbit of HD 189733 in near infrared

SPIRou is a near-infrared (NIR) spectropolarimeter and a high-precision velocimeter at CFHT, Hawaii. The detailed description of SPIRou is given in Sec. 2.1.3 of Chapter 2.

HD 189733 is an interesting target as it is close to the celestial equator and can be observed from both hemispheres. Many astronomers, therefore, choose this target for examining their models or while investigating the potential of a new instrument. HD 189733 was observed with SPIRou to investigate its proficiency. Although SPIRou is optimized for cooler stars (mainly late M-dwarfs), it will be interesting to revisit this system with a new instrument and study the spectroscopic behavior in the NIR domain. In this chapter, I present the first near-infrared spectropolarimetric observation for HD 189733, as measured by SPIRou. The spectroscopic and polarimetric data obtained with SPIRou were analyzed for its first science results in Moutou et al. (2020) (Accepted in A&A). Particularly, I worked in analyzing the spectroscopic data to obtain the obliquity measurement for HD 189733 b using classical RM fit and Doppler Shadow.

Orbital Signal

Before analyzing the RM anomaly, it is interesting to see the orbital signal of HD 189733 obtained with SPIRou³. The data for HD 189733 were obtained with SPIRou with the time series spread over three commissioning runs from July to October 2018. Several tests are performed in the CCF analysis to improve radial velocity precision and to minimize systematic effects. The radial velocities are obtained using a K2 'filtered' mask⁴ as they showed minimum dispersion in their residuals. The planetary orbit is successfully recovered, as known from the literature (see Figure 5.6). The

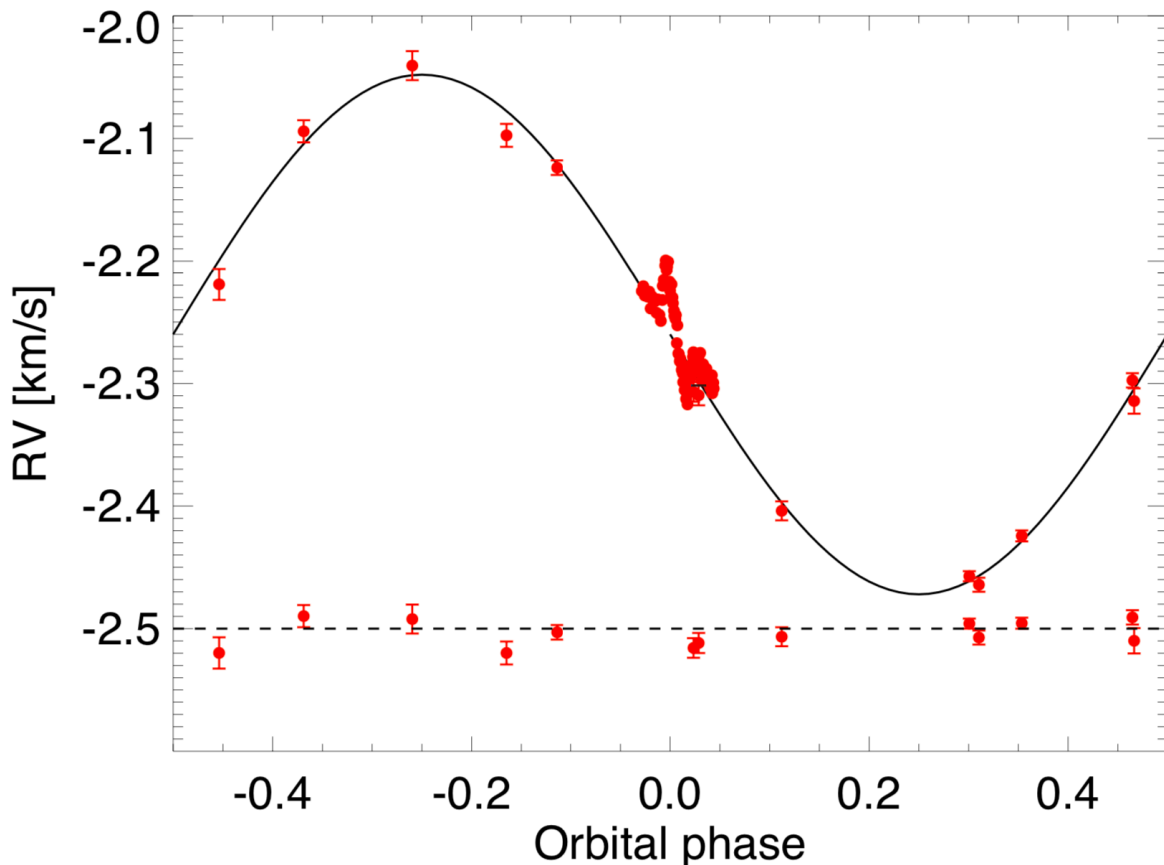


Figure 5.6 – The average RV per polarimetric sequence taken over the orbital cycles of HD 189733 as a function of orbital phase along with the residuals to the Keplerian model.

dispersion of the O-C residuals is found to be 10.2 m/s with the "K2-filtered" mask. This residual

³The data analysis to obtain the orbital signal of HD 189733 was done by Claire Moutou.

⁴Some lines are filtered from K2 mask based on a criterion described in Table 2 of Moutou et al. (2020)

scatter is compatible with the dispersion jitter previously found by [Bouchy et al. \(2005\)](#) (15 m/s, ELODIE), [Winn et al. \(2006\)](#) (12 m/s, HIRES) and [Boisse et al. \(2009\)](#) (9 m/s, SOPHIE) and with the 33.5 m/s peak-to-peak variations reported by [Triaud et al. \(2009\)](#) between several transit sequences (HARPS) – all obtained with optical spectrographs.

5.3.3 Observation and Analysis

The two transit sequences were obtained in spectroscopic mode on September 21-22, 2018, and June 14-15, 2019. The first transit sequence was taken during a commissioning night and lacked observations before the ingress of the planet. The second transit sequence is complete with data before the ingress and after the egress. Several tests are performed in the CCF analysis to improve radial velocity precision and minimize systematic effects in the short timescale. The dispersion of residuals is also inspected for out-of-transit data after subtracting the known orbital signal. Finally, the CCFs and the RVs are obtained using a K2-filtered mask. The dispersion of the residuals is minimal in both the Keplerian and RM fitting for the K2-filtered mask (see Table 2 for the dispersion from different masks in [Moutou et al. \(2020\)](#)).

Limb darkening in IR range

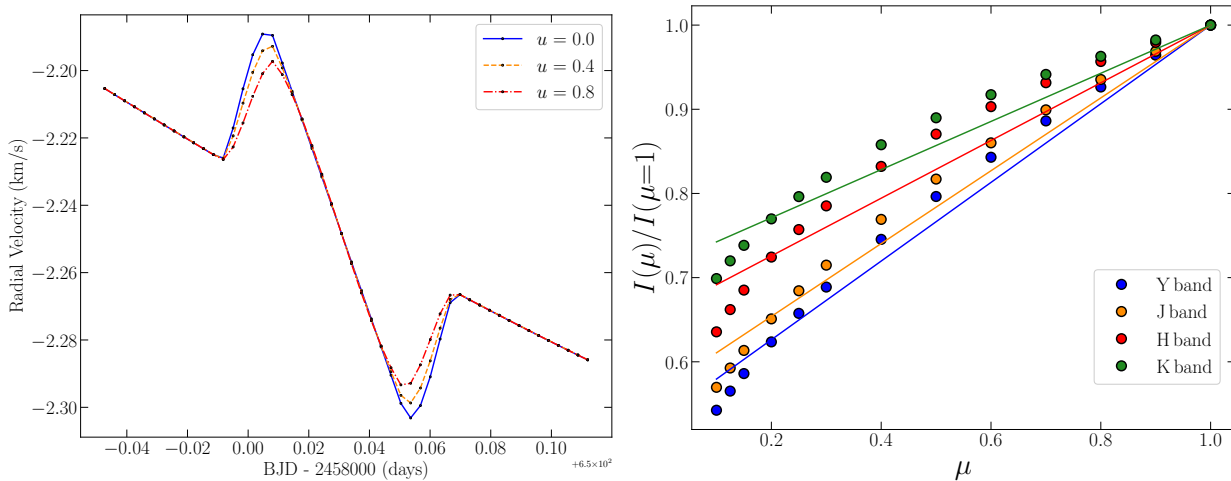


Figure 5.7 – *Left panel*: The shape of RM anomaly for different values of linear limb darkening coefficient. *Right panel*: The fitted linear limb darkening law in different bands of SPIRou (details are given in the text).

The radial velocity anomaly due to the RM effect is sensitive to the limb darkening coefficient. The left panel of figure 5.7 shows how the shape of the RM anomaly changes with the linear limb darkening coefficient. It is, therefore, important to consider a good value for the limb darkening coefficient. The limb darkening effect is dependent on wavelength. [Hayek et al. \(2012\)](#) provide limb darkening laws for HD 189733 derived from 3D stellar model atmospheres for different wavelengths. Their model in the infrared range is used to find a linear limb darkening coefficient (u). The right panel of the figure 5.7 shows the surface intensity $I(\mu)/I(\mu = 1)$ for HD 189733 at different angles (μ) and for different bands of the spectra. A simple linear limb darkening law is used to fit the surface intensity to obtain an approximate value of u . None of the RV measurements are taken with the planet too close to the limb, when $\mu < 0.1$. Therefore only surface intensities with $\mu \geq 0.1$ are considered while fitting the linear limb darkening law. For further analysis, the linear limb darkening coefficient fitted in the J-band, i.e., $u = 0.433$, is used.

5.3.4 Obliquity measurement using classical RM Fit

The model developed by [Ohta et al. \(2005\)](#) is used to fit the RM anomaly. This model takes into account the stellar limb darkening and derives accurate analytic formulae for the radial velocity anomaly. The two transits of HD 189733 b are fitted simultaneously using five free parameters: The sky-projected obliquity λ , the projected rotation velocity $V_S \sin I_S$, the transit epoch τ and two systematic velocities γ_1 and γ_2 for transit 1 and transit 2, respectively. All other transit and Keplerian parameters were fixed at the values reported in the literature (see Table 5.1).

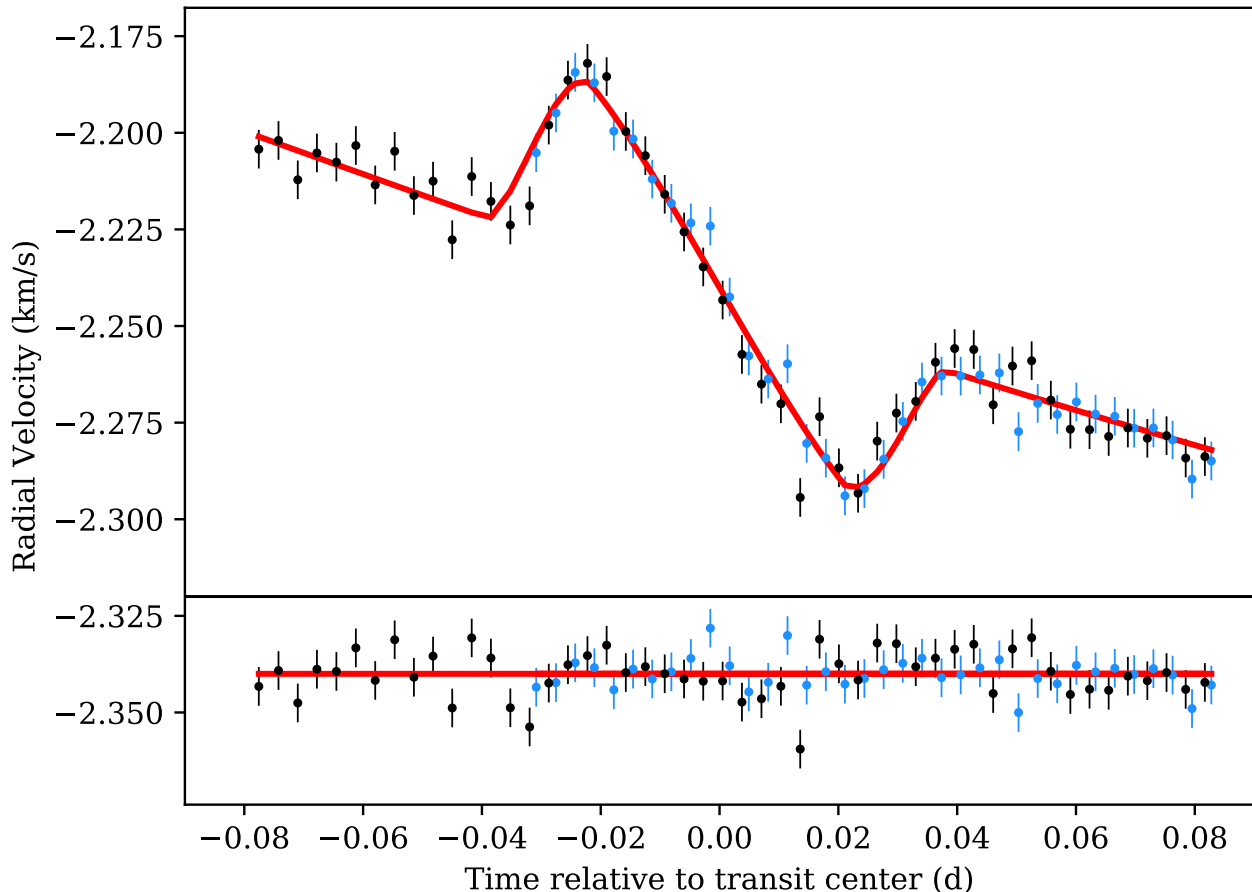


Figure 5.8 – The RV measurements of both the observed transits as obtained from the CCF analysis are indicated as blue (first transit sequence) and black circles (second transit sequence). The solid red line represents the best-fitted model obtained with the MCMC procedure. After subtracting the best-fitted model, the residuals are shifted by -2.34 km s^{-1} for better visualization.

An MCMC analysis is performed for measuring λ for HD 189733. The posterior distributions of λ , $V_S \sin I_S$ and τ are sampled assuming uniform priors using the public Markov-Chain Monte Carlo (MCMC) software emcee ([Foreman-Mackey et al., 2013](#)). Table 5.2 shows the priors adopted for the free parameters. 50 walkers and 2000 steps of MCMC are used, and the first 500 steps are discarded for burn-in. The best-fit values are the medians of the posterior distributions with 1σ uncertainties, which are derived by taking limits at 34% on either side of the median, as listed in Table 5.2. The RV measurements of HD 189733 taken during both transits of the planet on September 21, 2018, and June 14, 2019, along with the best-fitted model, are shown in Figure 5.8. The sky-projected obliquity is found to be, $\lambda = -3.6^{+1.5}_{-1.4}$ degrees and $V_S \sin I_S = 3.29^{+0.09}_{-0.09} \text{ km s}^{-1}$.

The values obtained with these two transits are in agreement within 2σ with the values obtained from data in the optical range: $\lambda = -0.85^{+0.32}_{-0.28}$ degrees and $V_S \sin I_S = 3.316^{+0.017}_{-0.067} \text{ km s}^{-1}$

Table 5.1 – Planetary parameters for the Rossiter-McLaughlin fit.

Parameter	Unit	Prior type	Value	Reference
Period	days	Fixed	2.21857545	Baluev et al. (2019)
K	kms ⁻¹	Fixed	0.201	Boisse et al. (2009)
ω	degrees	Fixed	90.0	Winn et al. (2007)
e		Fixed	0.0028	Baluev et al. (2019)
a/R		Fixed	8.7566	Triaud et al. (2009)
i_S	degrees	Fixed	85.712	Baluev et al. (2019)
r/R		Fixed	0.15703	Baluev et al. (2019)

from 4 transit sequences with HARPS, as analyzed by Triaud et al. (2009), or revised later with $\lambda = -0.4 \pm 0.2$ degrees from Cegla et al. (2016). Moreover, when the two data sets are fitted separately, the second transit shows a smaller offset on the λ value compared to the optical value, -1.9 ± 1.8 degrees, compared to both sequences combined. This is likely since the first sequence is not complete and has no RV data before the ingress. Such partial sequences may lead to increased systematics.

The dispersion of residuals after subtraction of the Keplerian+RM model is of 5.31 m/s for both transits with 4.08 m/s and 6.04 m/s for the September 2018 and June 2019 transit respectively. The out-of-transit RV data have a dispersion of 3.82 and 5.25 m/s for the first and second transit sequences (15 and 27 baseline data points, resp.) respectively. The final fit parameters did not change significantly for different values of the limb-darkening coefficient u corresponding to each band ($u_Y = 0.467$, $u_H = 0.343$ and $u_K = 0.286$). Apart from that, the best-fit value of the transit epoch, τ , is also consistent with the value of (τ_0) in Baluev et al. (2019) by propagating over different orbits using the orbital period from Table 2 of Baluev et al. (2019). Figure 5.9 shows the correlation diagrams for all five free parameters.

Table 5.2 – Best-fit parameters of the classical Rossiter-McLaughlin fit.

Parameter	Unit	Prior type	Value	Reference
$\tau - 245000$	BJD	$\mathcal{U}(8383.800, 58383.803)$	8383.8012189 ^{+0.00036} _{-0.00035}	This work
λ	degrees	$\mathcal{U}(-10, 10)$	-3.6 ^{+1.5} _{-1.4}	This work
$V_S \sin I_S$	kms ⁻¹	$\mathcal{U}(2, 5)$	3.29 ^{+0.09} _{-0.09}	This work
γ_1	kms ⁻¹	$\mathcal{N}(-2.3, 0.1)$	-2.15221 ^{+0.001} _{-0.001}	This work
γ_2	kms ⁻¹	$\mathcal{N}(-2.3, 0.1)$	-2.15745 ^{+0.0008} _{-0.0008}	This work

$\mathcal{U}(\text{min}, \text{max})$ corresponds to a uniform probability distribution with min. and max. as the minimum and maximum values, and $\mathcal{N}(\text{mean}, \text{sigma})$ corresponds to a normal probability distribution.

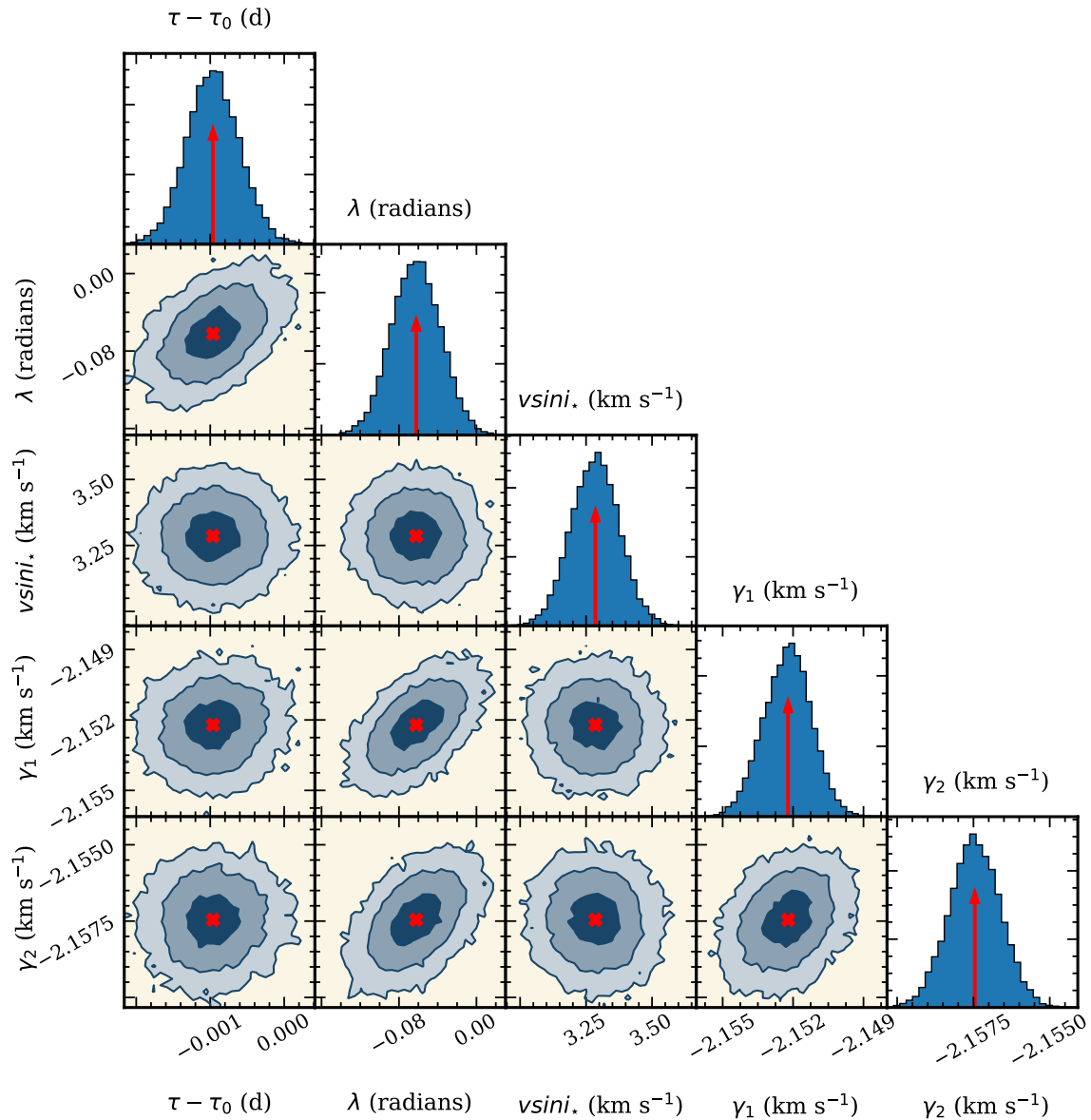


Figure 5.9 – The corner plot of the Rossiter-McLaughlin effect when both transit sequences are combined. Different color counters mark the 1σ , 2σ , and 3σ regions. The red arrows on the histograms correspond to the medians of the distributions. The parameter $vsini_*$ plotted here is same as $V_S \sin I_S$.

5.3.5 Obliquity measurement using Doppler Shadow

Another technique, Doppler Shadow, is also applied to the same data to find the obliquity measurement for HD 189733 b to check its consistency with the classical RM method. The values of the obliquity measurement from Doppler Shadow are obtained only for the second transit. The 50 CCFs from the second transit used for this analysis are obtained from the K2-filtered mask. The model of stellar CCF that includes a limb-darkened rotation profile convolved with a Gaussian corresponding to the intrinsic photospheric line profiles and instrumental broadening is considered following the approach of [Collier Cameron et al. \(2010\)](#). A tomographic model that depends on the same parameters as the classical RM fit (Sec. 5.3.4), and the local line profile width s (non rotating local CCF width) expressed in units of the projected stellar rotational velocity ([Collier Cameron et al., 2010](#); [Dalal et al., 2019](#)), is built.

The free parameters used to fit the Gaussian bump are λ , $V_S \sin I_S$, γ and s . The τ was fixed to τ_0 , and other parameters were taken from the literature. A linear limb darkening model was

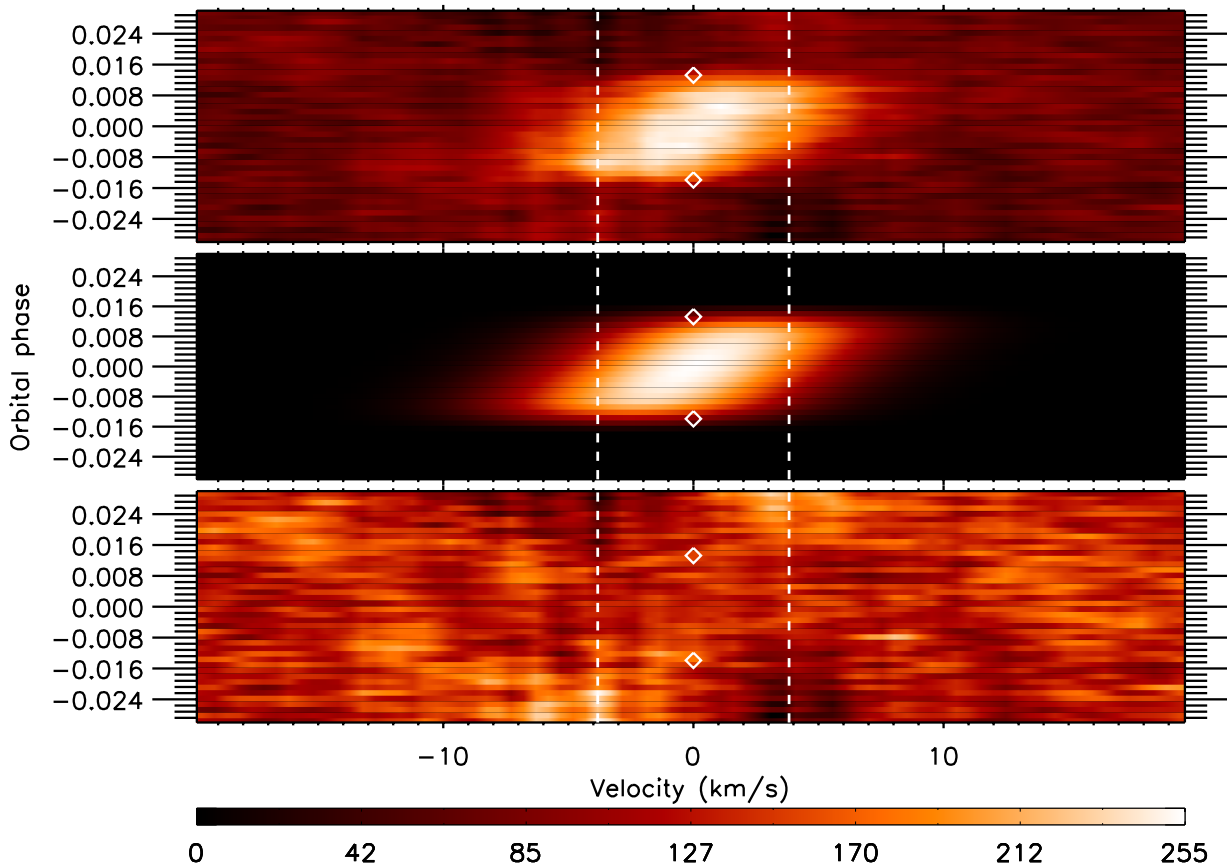


Figure 5.10 – Doppler Shadow results obtained for the second transit: the diamonds mark the ingress and egress from literature ephemeris, and the dashed line corresponds to the $V_S \sin I_S$ of the star. Top panel: The residuals after subtracting the stellar model CCF from the CCFs obtained. Middle panel: The best-fit model corresponding to $\lambda = -0.5$ degrees. Bottom panel: The residuals after subtracting the best-fit model.

considered with $u = 0.433$. The top panel in Figure 5.10 shows the bright signal corresponding to the stellar surface regions that are occulted by HD 189733 b. The best-fit model is plotted in the middle panel of Figure 5.10. It is obtained with $\lambda = -0.5^{+1.2}_{-1.3}$ degrees and $V_S \sin I_S = 3.80^{+0.16}_{-0.16}$ km/s. The bottom panel shows the residual CCFs after subtracting the best-fit model. The obliquity and rotational velocity from both the classical RM and the Doppler Shadow models are in good agreement (See Sec. 5.3.4).

5.3.6 Results and Conclusion

The Rossiter-McLaughlin signal is retrieved very well from the two transits of HD 189733 b. This is the first time that Doppler Shadow was used to measure the obliquity in the near-infrared range. The obliquity measurements obtained from classical RM fit and Doppler Shadow are compatible with the results obtained from the optical data. Modeling the data from the second sequence using classical RM fit alone yields a result closer to the optical data, although with slightly larger error bars.

SPIRou is a useful addition to the RV precision instruments in the near-infrared domain to detect and characterize exoplanets around young stars. In addition, the polarimeter on SPIRou

offers new ways to explore the surface activity of host stars that suppress the radial velocity data. With the help of SPIRou and supporting spectroscopic data from iSHELL, [Martioli et al. \(2020\)](#) recently measured the sky-projected obliquity and magnetic field of a young planet, AU Mic b. Using the classical Rossiter-McLaughlin technique, the Super Neptunes AU Mic b is found to be in aligned orbit. These recent observations also illustrate that SPIRou has the potential for detecting and characterizing new exoplanets.

5.4 Summary

This chapter discussed the measurement of sky-projected obliquity for two exoplanets, HD 3167 c, and HD 189733 b.

In the case of HD 3167 c, a new obliquity measurement with HARPSN data was obtained. HD 3167 is one of the few multi-planet systems which have only small known exoplanets. Three different techniques (classical RM fit, Doppler Shadow, and Reloaded RM) were applied to measure λ . HD 3167 c is found to be in a nearly polar orbit with $\lambda \sim -97 \pm 23$ degrees. The dynamical analysis was also performed for the planetary system to explain its polar orbit, which found that the planets HD 3167 c and d are co-planar. However, no clear conclusion was made for the misaligned orbits of HD 3167 c and d. Finally, it was postulated that the presence of an outer companion which (if detected) might explain the polar orbit of planets c and d.

In the case of HD 189733 b, the first obliquity measurement in the near-infrared for HD 189733 b was obtained by revisiting the system with the new spectropolarimeter SPIRou. To obtain the obliquity measurement, two different techniques (classical RM fit and Doppler Shadow) were implemented. The obliquity measurement obtained in the NIR wavelength is -3.6 ± 1.5 degrees (using classical RM) and -0.5 ± 1.3 degrees (using Doppler Shadow), which is also compatible with the obliquity measurement in the optical wavelength.

5.5 References

- Albrecht S., et al., 2012, [ApJ](#), **757**, 18 60, 61, 62
- Albrecht S., Winn J. N., Marcy G. W., Howard A. W., Isaacson H., Johnson J. A., 2013, [ApJ](#), **771**, 11 60, 62
- Anderson K. R., Lai D., 2018, [MNRAS](#), **480**, 1402 60
- Anderson K. R., Storch N. I., Lai D., 2016, [MNRAS](#), **456**, 3671 60
- Baluev R. V., et al., 2019, [MNRAS](#), **490**, 1294 82
- Bate M. R., Lodato G., Pringle J. E., 2010, [MNRAS](#), **401**, 1505 60
- Batygin K., 2012, [Nature](#), **491**, 418 60
- Beck J. G., Giles P., 2005, [ApJ](#), **621**, L153 60
- Boisse I., et al., 2009, [A&A](#), **495**, 959 80, 82
- Bouchy F., et al., 2005, [A&A](#), **444**, L15 78, 80
- Bourrier V., Cegla H. M., Lovis C., Wyttenbach A., 2017, [A&A](#), **599**, A33 62

- Bourrier V., et al., 2018, *Nature*, 553, 477 62
- Breslau A., Pfalzner S., 2019, *A&A*, 621, A101 60
- Cegla H. M., Lovis C., Bourrier V., Beeck B., Watson C. A., Pepe E., 2016, *A&A*, 588, A127 61, 78, 82
- Chatterjee S., Ford E. B., Matsumura S., Rasio F. A., 2008, *ApJ*, 686, 580 60
- Christiansen J. L., et al., 2017, *AJ*, 154, 122 63, 64
- Collier Cameron A., Bruce V. A., Miller G. R. M., TriAUD A. H. M. J., Queloz D., 2010, *MNRAS*, 403, 151 61, 78, 83
- Dai F., Winn J. N., Yu L., Albrecht S., 2017, *AJ*, 153, 40 60
- Dalal S., Hébrard G., Lecavelier des Étangs A., Petit A. C., Bourrier V., Laskar J., König P. C., Correia A. C. M., 2019, *A&A*, 631, A28 60, 62, 64, 83
- Fabrycky D., Tremaine S., 2007, *ApJ*, 669, 1298 60
- Fielding D. B., McKee C. F., Socrates A., Cunningham A. J., Klein R. I., 2015, *MNRAS*, 450, 3306 60
- Foreman-Mackey D., Hogg D. W., Lang D., Goodman J., 2013, *PASP*, 125, 306 81
- Gandolfi D., et al., 2017, *AJ*, 154, 123 63, 77
- Hayek W., Sing D., Pont F., Asplund M., 2012, *A&A*, 539, A102 80
- Hébrard G., et al., 2008, *A&A*, 488, 763 61
- Hébrard G., et al., 2011, *A&A*, 527, L11 62
- Hirano T., et al., 2012, *ApJ*, 759, L36 62
- Hirano T., et al., 2020, *ApJ*, 890, L27 62
- Huber D., et al., 2013, *Science*, 342, 331 62
- Kamiaka S., Benomar O., Suto Y., Dai F., Masuda K., Winn J. N., 2019, *AJ*, 157, 137 62
- Lai D., Foucart F., Lin D. N. C., 2011, *MNRAS*, 412, 2790 60
- Martioli E., et al., 2020, arXiv e-prints, p. arXiv:2006.13269 85
- Morton T. D., Johnson J. A., 2011, *ApJ*, 729, 138 60
- Moutou C., et al., 2020, arXiv e-prints, p. arXiv:2008.05411 79, 80
- Muñoz D. J., Perets H. B., 2018, *AJ*, 156, 253 61
- Nagasawa M., Ida S., 2011, *ApJ*, 742, 72 60
- Naoz S., Farr W. M., Lithwick Y., Rasio F. A., Teyssandier J., 2011, *Nature*, 473, 187 60
- Ohta Y., Taruya A., Suto Y., 2005, *ApJ*, 622, 1118 81
- Queloz D., et al., 2010, *A&A*, 517, L1 62

- Sanchis-Ojeda R., et al., 2012, *Nature*, 487, 449 62
- Simpson E. K., et al., 2011, *MNRAS*, 414, 3023 62
- Triaud A. H. M. J., 2011, *A&A*, 534, L6 61
- Triaud A. H. M. J., et al., 2009, *A&A*, 506, 377 61, 80, 82
- Triaud A. H. M. J., et al., 2010, *A&A*, 524, A25 61
- Van Eylen V., et al., 2014, *ApJ*, 782, 14 60
- Vanderburg A., et al., 2016, *ApJ*, 829, L9 62, 63
- Winn J. N., et al., 2006, *ApJ*, 653, L69 61, 78, 80
- Winn J. N., et al., 2007, *AJ*, 133, 1828 82
- Winn J. N., Fabrycky D., Albrecht S., Johnson J. A., 2010a, *ApJ*, 718, L145 60
- Winn J. N., et al., 2010b, *ApJ*, 723, L223 62
- Wolfson M. M., 1993, *QJRAS*, 34, 1 60
- Zhou G., et al., 2020, *ApJ*, 892, L21 62

Chapter 6

Conclusion & Prospects

*“ All truths are easy to understand,
once they are discovered; the point
is to discover them. ”*

Galileo Galilei

Contents

6.1 References	92
------------------------------------	-----------

In this chapter, I draw the main conclusions about the work presented in this thesis and prospects. This chapter aims to link this thesis to the bigger picture of existing exoplanet knowledge and reveal pathways for future research.

Despite the increasing number of exoplanets detection, no planetary system which truly resembles our Solar System has been discovered. However, giant planets that are analogous to Solar System giant planets have been detected. The detection of such long period planets is possible thanks to many radial velocity, microlensing, and imaging surveys. One such ongoing radial velocity survey to detect giant planets is with SOPHIE at OHP. This survey aims to perform a volume-limited study of giant planets to improve the constraints on the exoplanet parameters and their hosting stars by detecting giant planets. Having a well-defined catalog for such a volume-limited survey is important. Therefore I present the new-definition of the stellar catalog in Chapter 3 that will be used to obtain statistics on giant planets, using SOPHIE.

Among all the exoplanets detected so far, giant planets that orbit close enough to its host star, are the easiest to detect with any method. The radial velocity method is sensitive to the mass of the companion and has discovered many massive planets. The first exoplanets detected using the radial velocity method were hot Jupiters that are massive and have very short orbital periods. As a result, many hot Jupiters have been detected and characterized, which eventually helped in building good statistical studies (Albrecht et al., 2012a,b; Steffen et al., 2012; Wright et al., 2012). Apart from that, with the increase in the number of cool Jupiters, new statistical studies are done. Wittenmyer et al. (2020) recently found with their small sample of 33 cool Jupiters that the cool Jupiters are more abundant than the hot Jupiters by comparing their occurrence rates. Thanks to the long time (14 years) baseline of SOPHIE, the detection of such long period planets is possible. In chapter 4, I report the discovery of 6 new cool Jupiters in the Solar neighborhood with SOPHIE. These detections will contribute by helping in deriving the true distribution and occurrence of cool Jupiters. In the future, exploring these two populations of giant planets together (hot Jupiters and cool Jupiters) will allow in building giant planet formation and evolution models.

The mass range of massive exoplanets overlaps with the mass range of low mass brown dwarfs, and this mass regime is poorly understood. A previous statistical study found that the formation process of brown dwarfs with masses $\leq 40 M_J$ is similar to the formation process of massive giant planets, and massive brown dwarfs might be formed in the same way as the low mass stars (Ma & Ge, 2014). There is an ongoing survey of brown-dwarf companions with SOPHIE in the Northern hemisphere, allowing for deriving meaningful and unbiased statistics of brown dwarf population. Under this program, six new brown dwarf companions and fifteen stellar companions are discovered (Chapter 4).

As the radial velocity method only allows us to obtain the minimum mass of the companion, it is difficult to differentiate between massive exoplanets and brown dwarfs. With the help of Gaia and Hipparcos astrometry data, the stellar inclination can be constrained. The analysis to find the true masses of these companions will be done in the future.

Our Solar System's planets are well aligned with the Sun's rotation axis, which can be explained by the standard paradigm of planet formation from the rotating protoplanetary disk (Woolfson, 1993). However, this is not a case for all the planetary systems. Exoplanets have a wide range of obliquities, and various mechanisms such as the Kozai-Lidov mechanism, planet-planet scattering, or inhomogeneous accretion are proposed to explain such (mis)alignment. There are a lot of obliquity measurements available for hot Jupiters, and only a few obliquity measurements are available for small exoplanets and even fewer for small exoplanets in multi-planet systems. In this thesis, I measure the obliquity of a small exoplanet in a multi-planet system, i.e., sub-Neptune HD 3167 c (Chapter 5), which are also published in Dalal et al. (2019). This observation is a valuable addition to the known planetary obliquity sample, extending it further beyond hot Jupiters.

HD 3167 c is found to be in nearly polar orbit, and dynamics of the system postulates that the presence of an outer companion in the system might explain the misalignment of HD 3167 c. There is a hint of an outer companion in the RV data of HD 3167 at an orbital period of 78 days and a mass of at least 0.03 M_J . However, with the current data, it is difficult to confirm this outer companion. In the future, more RV data measurements of HD 3167 on a longer time span might be able to reveal the outer companion and finally confirm/refute the speculation. Contrary to HD 3167, many multi-planet systems are found to be well-aligned such as Kepler 30 (Sanchis-Ojeda et al., 2012), Kepler 25 (Albrecht et al., 2013), Kepler 89 (Hirano et al., 2012) and TRAPPIST-1 (Hirano et al., 2020). A multi-planet system that is interesting concerning this work is Kepler 56. The two transiting planets of Kepler 56 are in misaligned orbit around its host star due to an outer companion (Huber et al., 2013; Otor et al., 2016). An extended sample of similar multi-planetary systems will help in identifying the mechanisms responsible for misalignment in such systems.

Another obliquity measurement presented in this thesis is for a well-studied hot Jupiter HD 189733 b. The obliquity of this hot Jupiters has been revisited previously six times to test new models and to obtain better constraints on the obliquity. This measurement of obliquity is done with a new instrument, SPIRou: It is a new near-infrared spectropolarimeter designed for most precise infrared velocimeters worldwide. The observations in NIR are motivated as the influence of starspots is reduced in the near-infrared compared with the visible (Barnes et al., 2011; Desort et al., 2007). The measurement of sky-projected obliquity for HD 189733 in this thesis is found compatible with the previous measurements. It is also the first time that Doppler shadow is used to measure the obliquity of HD 189733 in the near-infrared wavelength range. Furthermore, the potential of SPIRou for short term RV accuracy is analyzed, which will also allow us to measure the obliquity of many exoplanets in the future.

In addition to obliquity measurements, SPIRou will unveil many new exoplanets around different stellar populations, mainly late M-dwarfs, which are brighter in the infrared wavelength. These observations in NIR wavelengths will offer an additional advantage as it can be used to distinguish between the stellar activity and planet signatures. For example, Setiawan et al. (2008) reported the discovery of a hot Jupiter around a young T-Tauri star, TW Hya, using RV variations in optical wavelengths. Later NIR observation of a TW Hya by Huélamo et al. (2008) showed that the RV variation was due to spots on the surface of the star and not due to a hot Jupiter. Therefore, in this era of new NIR spectrographs, SPIRou will not only detect exoplanets, but it will also allow stellar characterization to study magnetic fields.

In the last decade, the numbers of exoplanet detected have tripled, and with new and upcoming instruments such as SPIRou, TESS, PLATO, and JWST, this number will keep on increasing. Detection and characterizing of sub-stellar objects thus become crucial to put constraints on their formation and evolution mechanisms. This thesis is a collection of a few such studies, which will be a small step in this direction.

6.1 References

- Albrecht S., et al., 2012a, *ApJ*, 757, 18 90
- Albrecht S., et al., 2012b, *ApJ*, 757, 18 90
- Albrecht S., Winn J. N., Marcy G. W., Howard A. W., Isaacson H., Johnson J. A., 2013, *ApJ*, 771, 11 91
- Barnes J. R., Jeffers S. V., Jones H. R. A., 2011, *MNRAS*, 412, 1599 91
- Dalal S., Hébrard G., Lecavelier des Étangs A., Petit A. C., Bourrier V., Laskar J., König P. C., Correia A. C. M., 2019, *A&A*, 631, A28 90
- Desort M., Lagrange A. M., Galland F, Udry S., Mayor M., 2007, *A&A*, 473, 983 91
- Hirano T., et al., 2012, *ApJ*, 759, L36 91
- Hirano T., et al., 2020, *ApJ*, 890, L27 91
- Huber D., et al., 2013, *Science*, 342, 331 91
- Huélamo N., et al., 2008, *A&A*, 489, L9 91
- Ma B., Ge J., 2014, *MNRAS*, 439, 2781 90
- Otor O. J., et al., 2016, *AJ*, 152, 165 91
- Sanchis-Ojeda R., et al., 2012, *Nature*, 487, 449 91
- Setiawan J., Henning T., Launhardt R., Müller A., Weise P, Kürster M., 2008, *Nature*, 451, 38 91
- Steffen J. H., et al., 2012, *Proceedings of the National Academy of Science*, 109, 7982 90
- Wittenmyer R. A., et al., 2020, *MNRAS*, 492, 377 90
- Wolfson M. M., 1993, *QJRAS*, 34, 1 90
- Wright J. T., Marcy G. W., Howard A. W., Johnson J. A., Morton T. D., Fischer D. A., 2012, *ApJ*, 753, 160 90

Appendix A

Annexes

This appendix contains the figures of the radial velocity variations of brown dwarfs and stellar companions which were fitted with keplerian solution in section 4.3.3 and 4.3.4 of Chapter 4.

Figure A.1: Orbital solutions of the radial velocity variations of the new candidates of six BDs are plotted here. The left panel shows the RV vs time with O-C residuals below and RV vs phase is on the right panel. SOPHIE+ measurements are plotted in red circles. If the target is observed before and after the upgrade, SOPHIE and SOPHIE+ measurements are plotted in red circles and blue squares simultaneously.

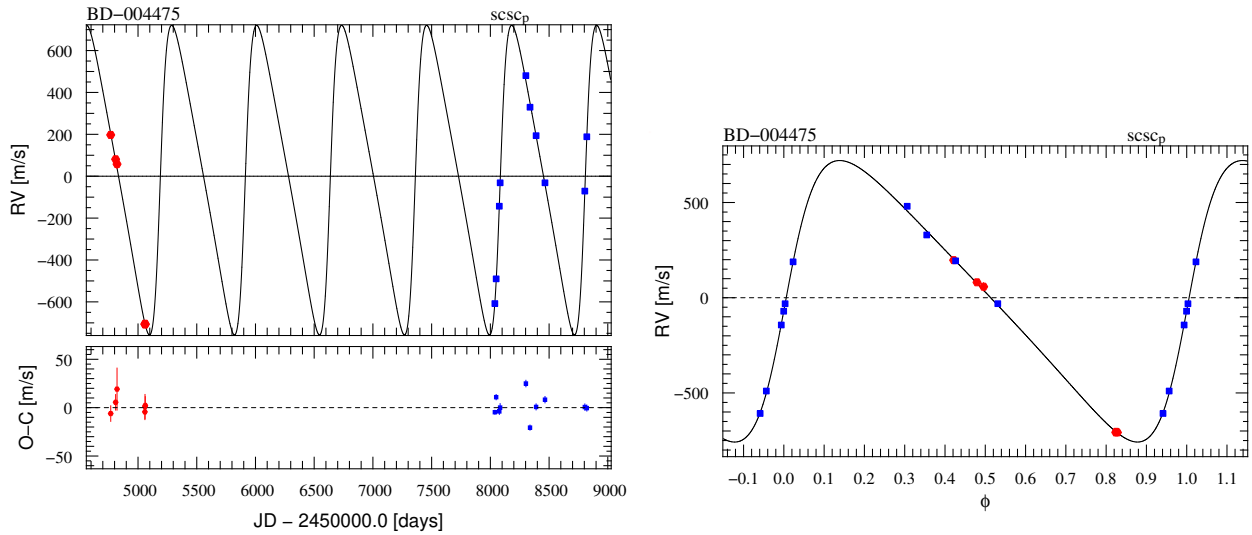


Figure A.1: Continued.

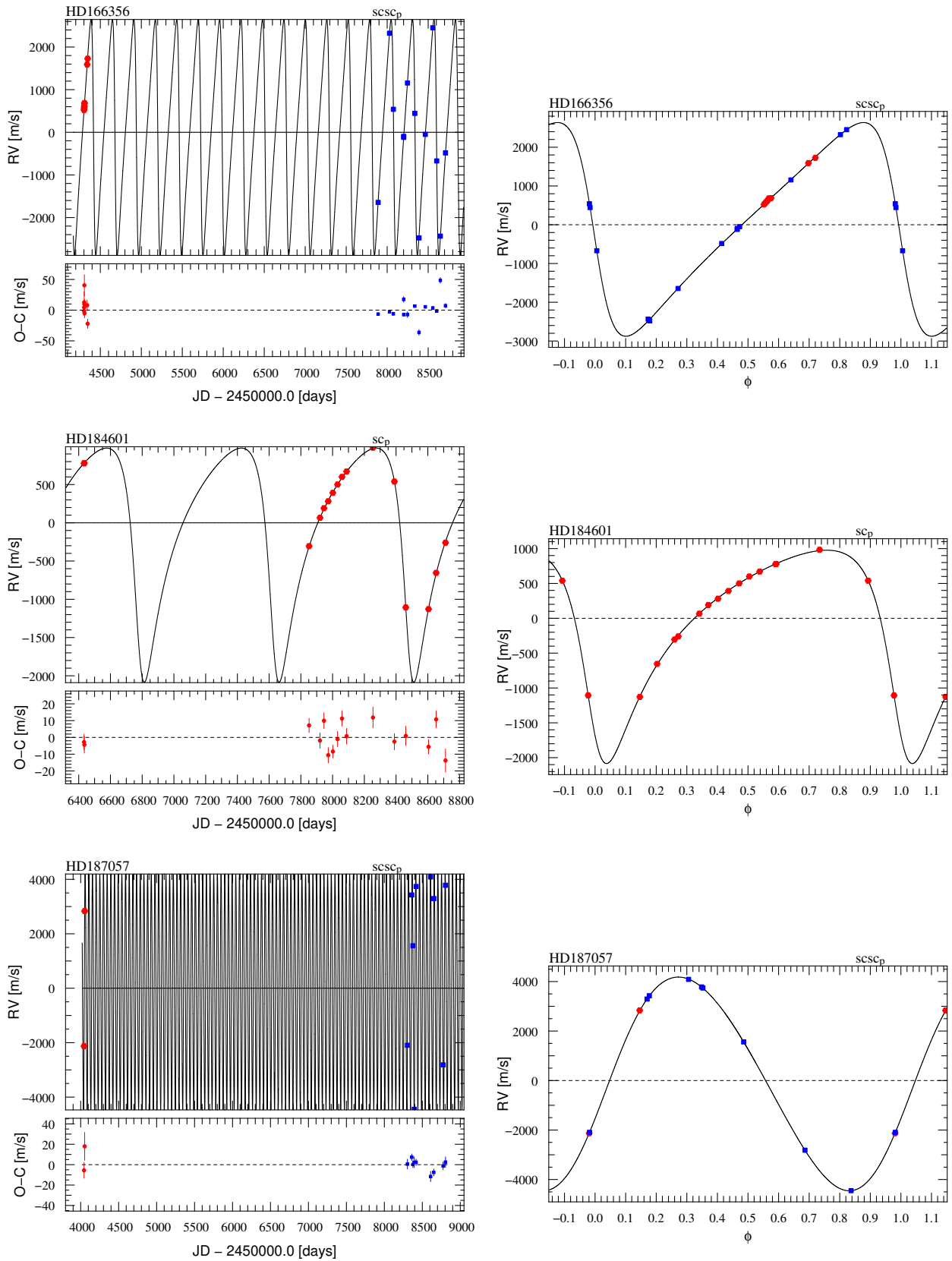


Figure A.1: Continued.

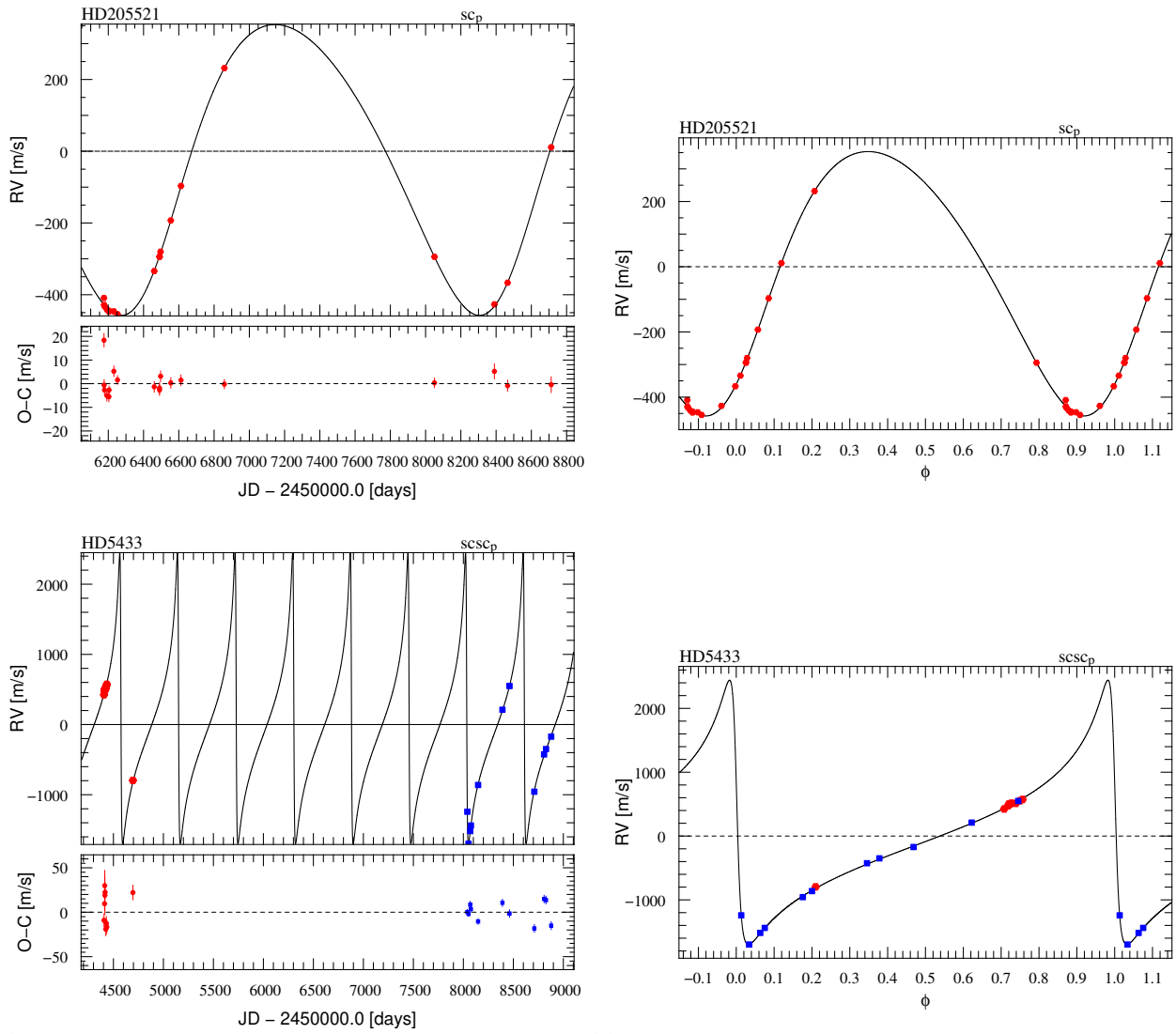


Figure A.2: Orbital solutions of the radial velocity variations of stellar companions obtained with SOPHIE spectrograph are plotted here. The left panel shows the RV vs time with O-C residuals below and RV vs phase is on the right panel. SOPHIE+ measurements are plotted in red circles. If the target is observed before and after the upgrade, SOPHIE and SOPHIE+ measurements are plotted in red circles and blue squares simultaneously.

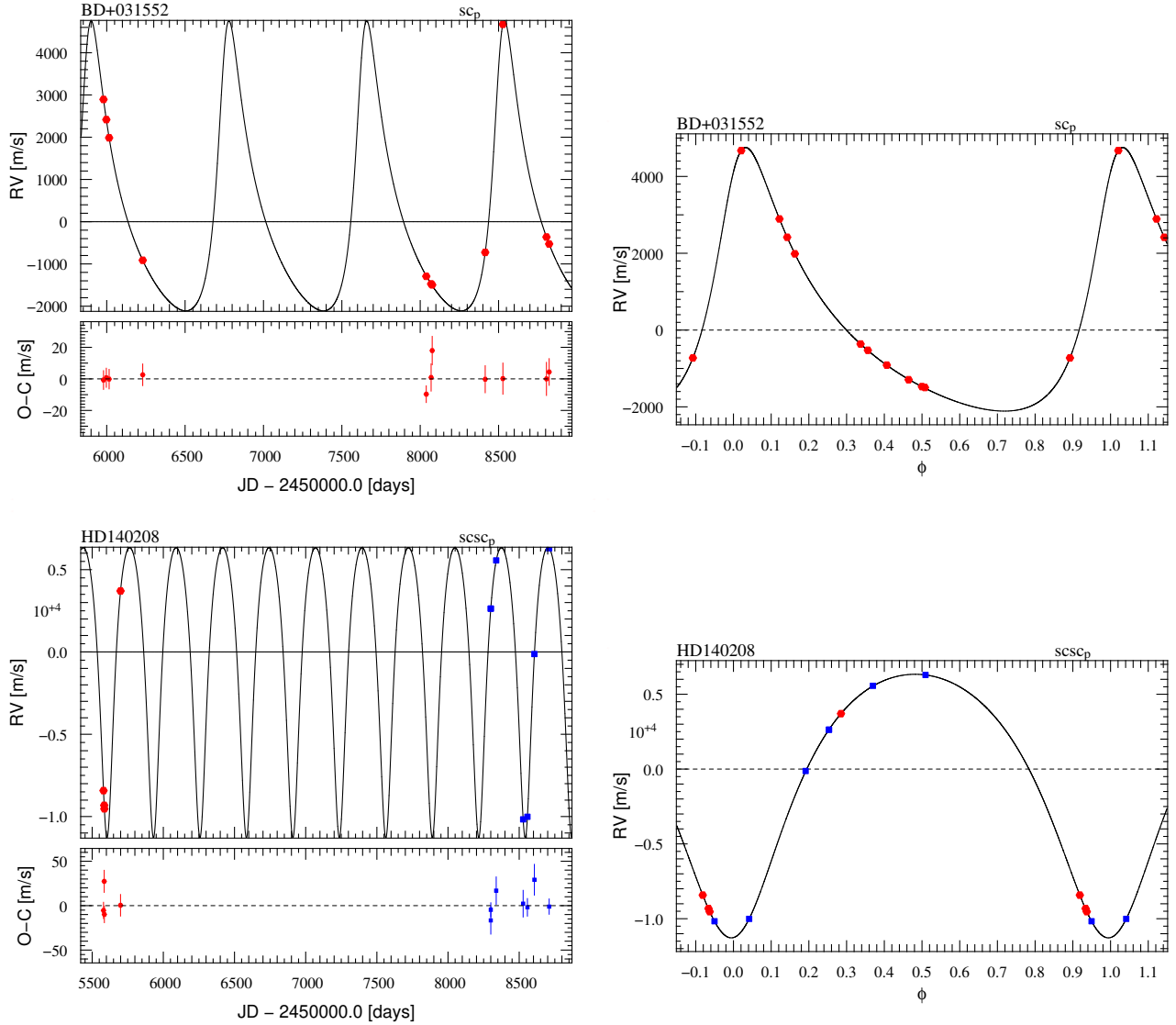


Figure A.2: Continued.

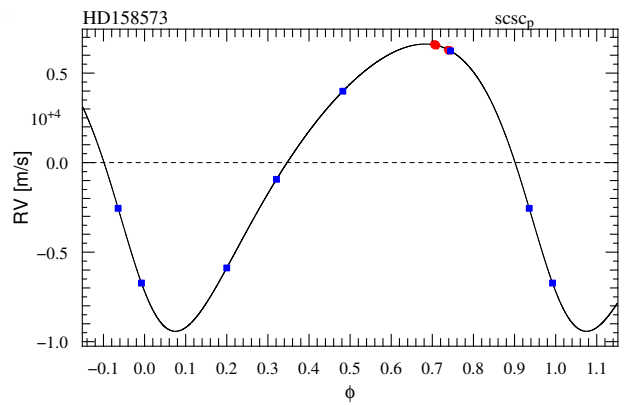
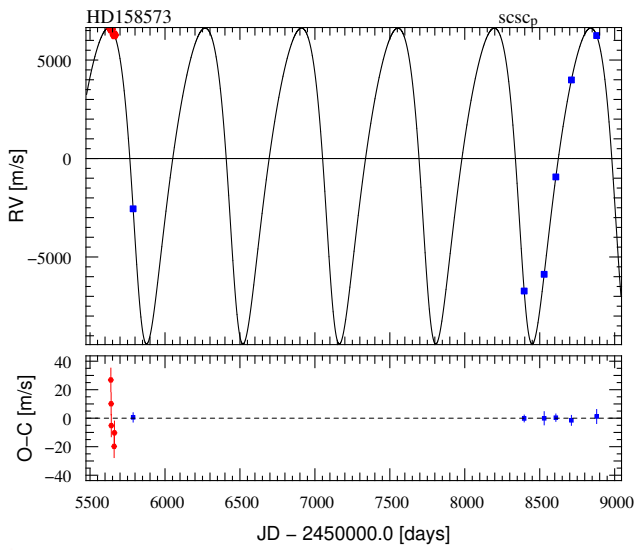
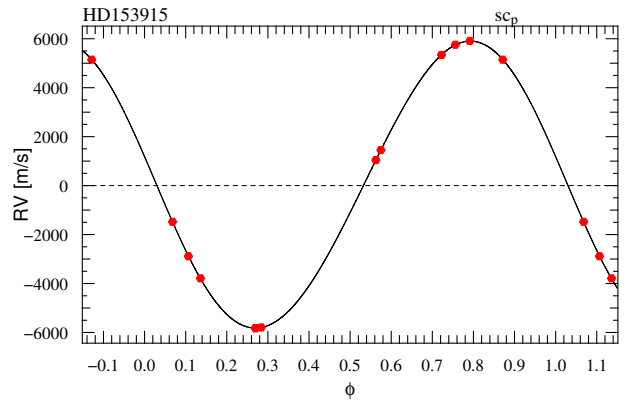
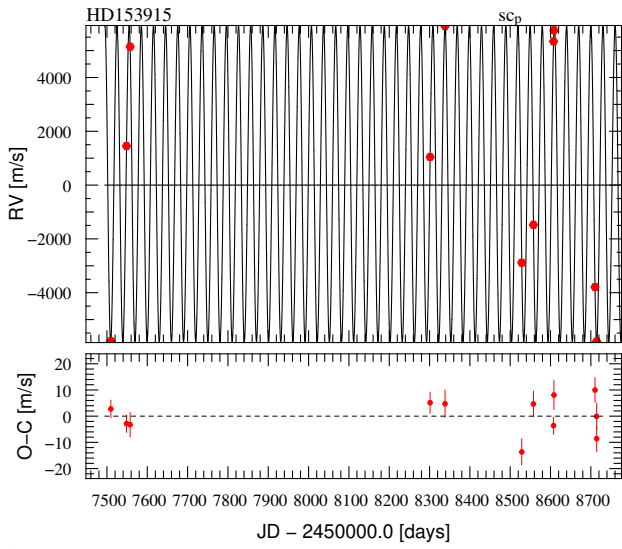
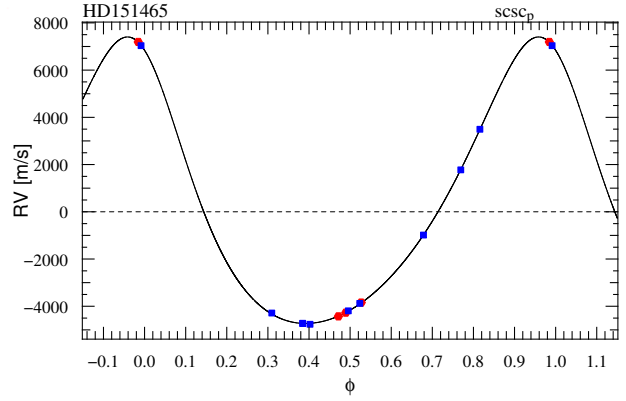
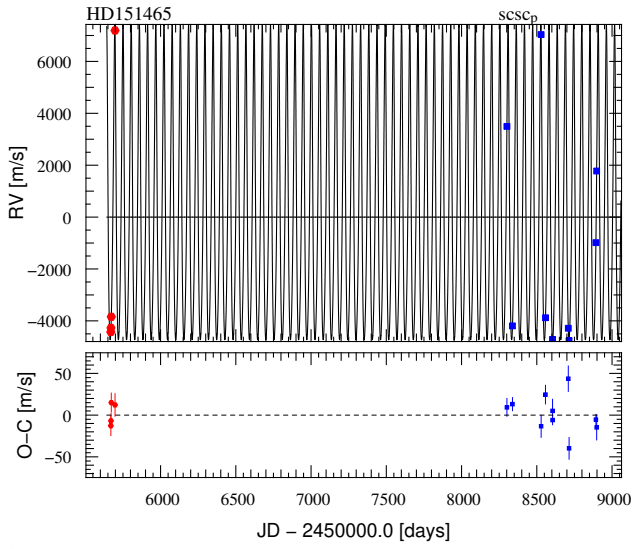


Figure A.2: Continued.

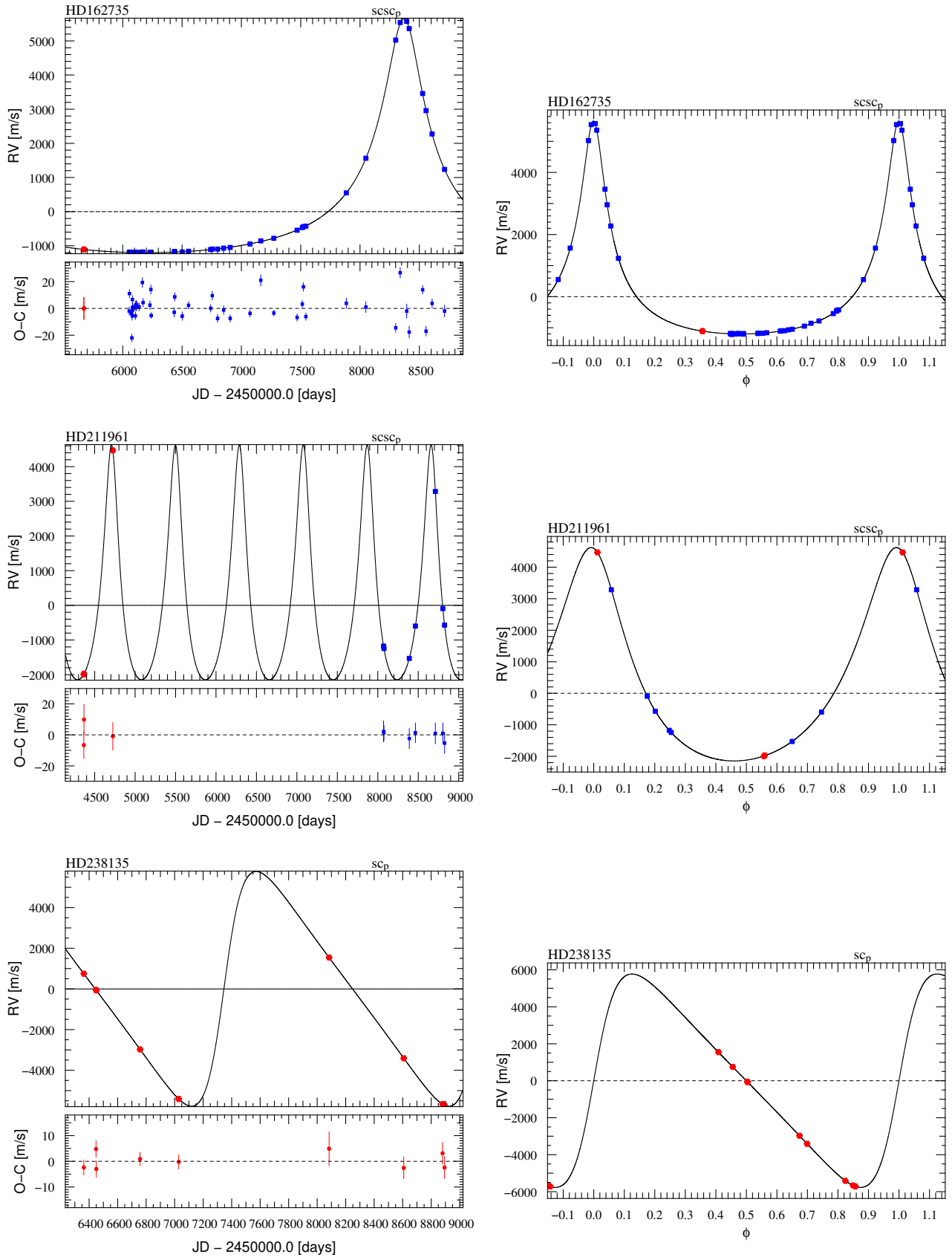


Figure A.2: Continued.

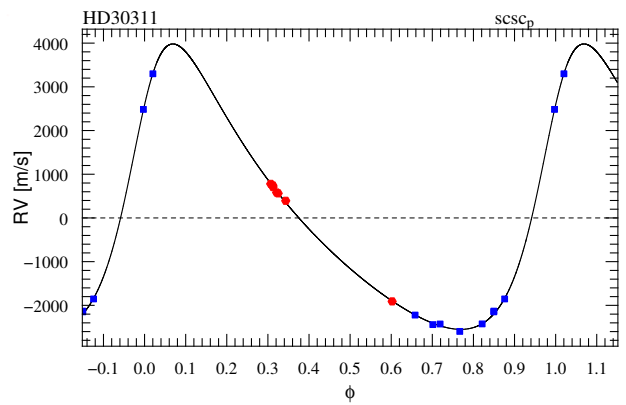
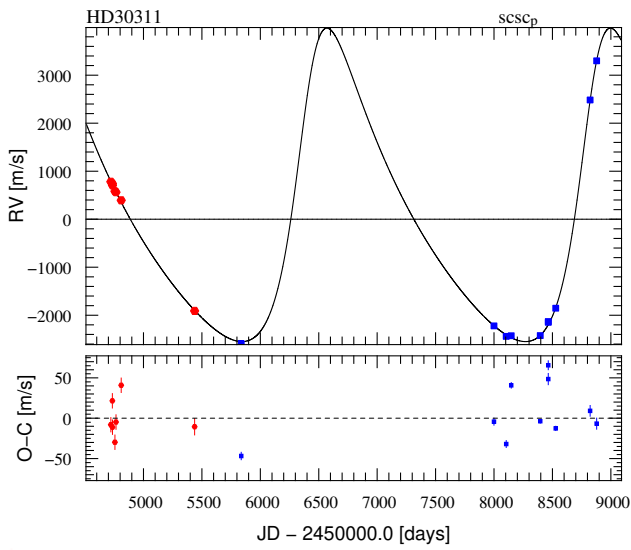
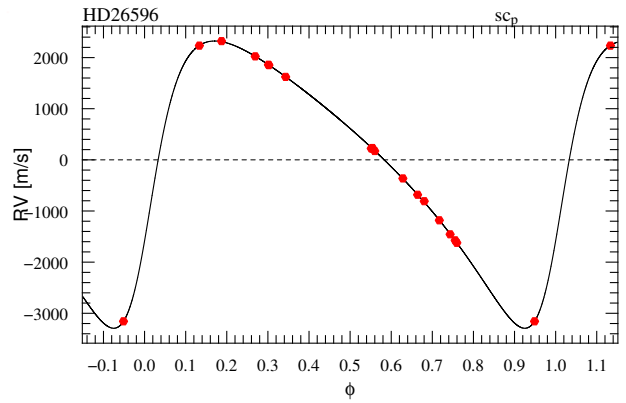
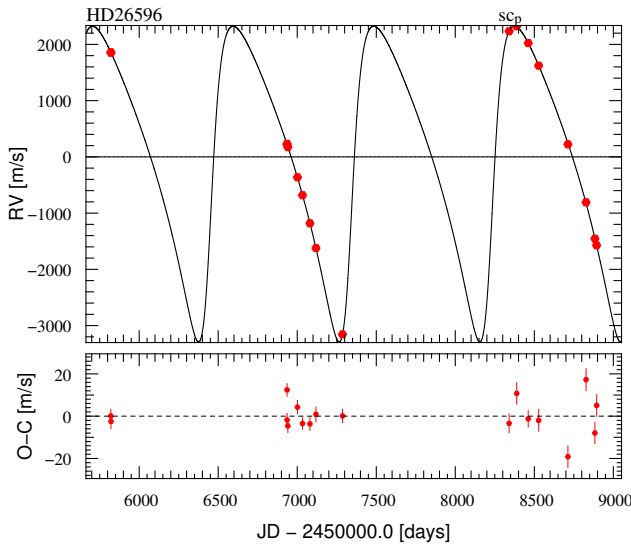
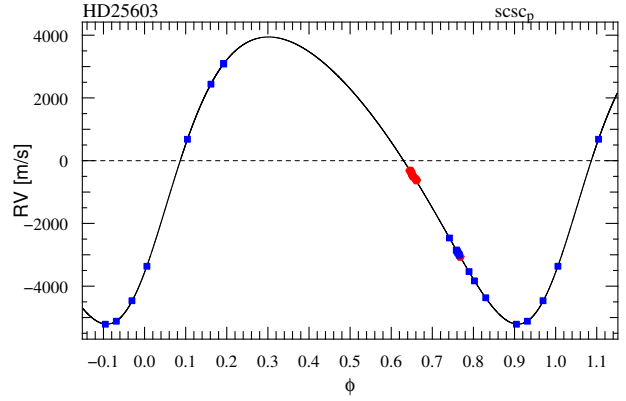
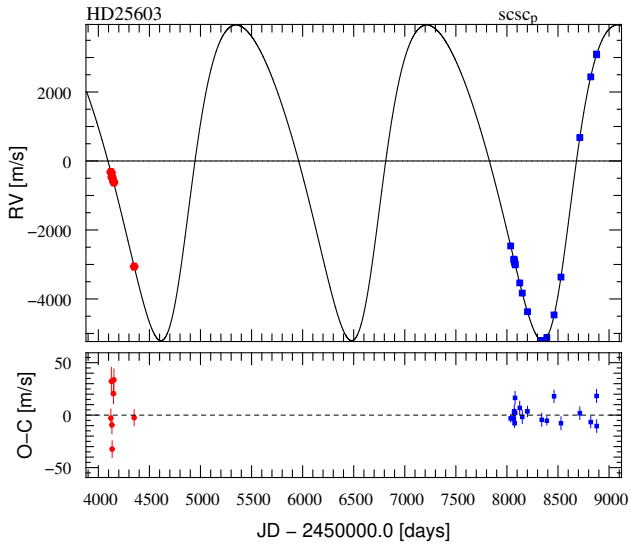


Figure A.2: Continued.

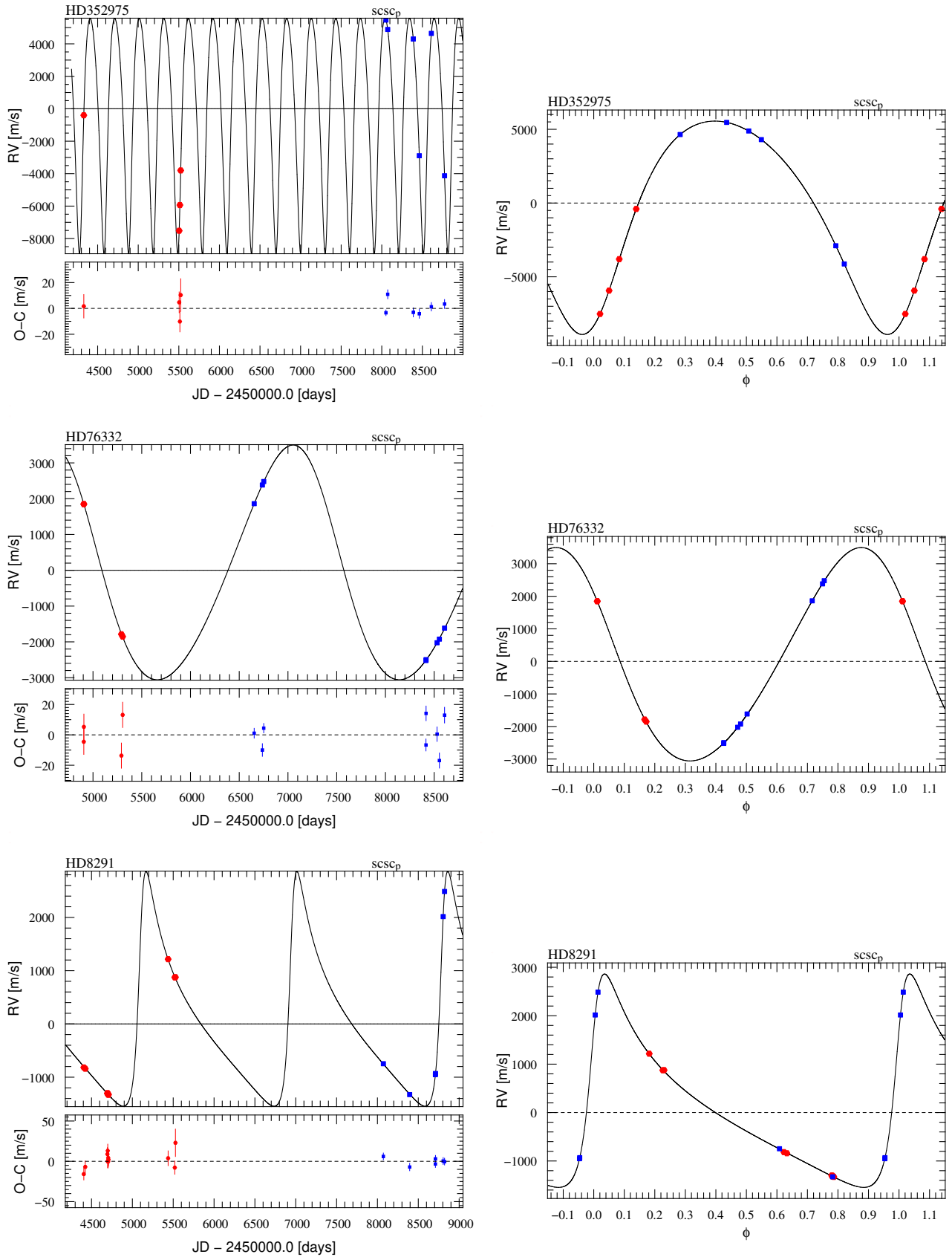


Figure A.2: Continued.

